공학박사학위논문

변분 기법을 적용한
측정 가속도로부터의
변위 및 속도 재구성 기법

- 플러터계수 추정에의 적용 -

Reconstruction of Dynamic Displacement and Velocity
based on the Variational Statement of an Inverse Problem
from Measured Acceleration with Special Application to the
Extraction of Flutter Derivatives

2011년 2월

서울대학교 대학원

건설환경공학부

홍 윤 화

Abstract

A new class of displacement reconstruction scheme is presented using only acceleration measured from a structure. For a given set of acceleration data, the reconstruction problem is formulated as a boundary value problem in which the acceleration is defined by the second-order ordinary differentiation of displacement. The displacement is reconstructed by minimizing the least squared errors between measured and approximated acceleration within a finite time interval. The displacement reconstruction problem becomes ill-posed because the boundary conditions at both ends of each time window are not known *a priori*. Furthermore, random noise in measured acceleration causes physically inadmissible errors in the reconstructed displacement. A Tikhonov regularization scheme is adopted to alleviate the ill-posedness. The governing equation for the reconstruction is derived by taking the variation to the regularized minimization problem, which yield beam on the elastic foundation problem. The conventional FIR (CFIR) filter directly approximates the transfer function of the governing equation, while the FDM-based FIR (FDM-FIR) and FEM-based FIR (FFIR) filter are formulated by the discretization of the minimization problem with the finite difference method and the finite element method, respectively. The FFIR filter is capable of reconstructing displacement and velocity simultaneously. The fundamental characteristics of the proposed filters are investigated in the frequency domain using the transfer and

accuracy functions. It is shown that the proposed FIR filters suppress low frequency noise components in measured accelerations effectively, and reconstruct physically meaningful displacement accurately. The validity of the proposed filters is demonstrated through several examples.

In the final example, a force-acceleration-based identification of the flutter derivatives of bridge decks in a wind tunnel is presented. An equation error estimator (EEE), which is the least square residual errors of the equation of motion, is employed to formulate the force-based identification scheme. Unlike most of previously proposed methods, the acceleration of an oscillating section model is measured in wind tunnel tests. The velocity and the displacement required in the EEE are reconstructed from the measured acceleration using the FFIR filter. As the EEE is expressed as a quadratic form with respect to flutter derivatives, neither an iterative solution scheme nor a complex eigenvalue analysis is required for optimization. The EEE method is capable of identifying the representative values of the flutter derivatives by one optimization process using multiple measurements for a wind velocity in wind tunnel tests and can be generally employed for the extraction of the flutter derivatives regardless of the testing procedures.

frequency dominant structure; Central finite difference; Time window; Tikhonov

regularization;

Student Number : 2007-30263

CHAPTER

List of Figures

List of Tables

1. Introduction

Dynamic responses of structural systems are frequently measured for the purpose of structural health monitoring (SHM) and structural control (SC) [Sohn 2004 and Housner 1997]. Among the dynamic responses, the time history of the dynamic displacement may contain precious information on structural behaviors that can be utilized in various SHM and SC applications. For example, in case a structure experiences severe events such as a strong earthquake or a typhoon, a quick decision on the possibility of structural damage could be made based on the maximum displacement of the structure [Gupta 2001, Park 1984 and Smyth 2007]. The displacements measured under normal operational conditions are utilized to identify nonlinear dynamic characteristics of a structure and to monitor abnormal changes in structural behaviors. For SC applications [Housner 1997], information on displacement should be provided in real-time or at least in near real-time to identify the states of a structure. Unfortunately, it is very difficult to measure displacement directly in large-scale structures such as bridges and buildings because fixed reference points are rarely found to install displacement transducers [Gavin 1998]. Moreover, the reference points as well as a structure move together during severe events, and thus the direct measurement of displacement becomes almost impossible.

Acceleration is easily measured without a fixed reference point unlike dis-

placement, and various types of accelerometers are commercially available for a wide range of dynamic frequency. Consequently, acceleration has been commonly measured for various engineering applications in real situations. From this point of view, the reconstruction of displacement from measured acceleration seems an attractive alternative to the direct measurement of displacement.

Various digital filters may be considered for the purpose of displacement reconstruction from measured accelerations. Among them, infinite impulse response filters (IIR filters) and finite impulse response filters (FIR filters) are widely employed in various applications [Bardella 2003, Boore 1997, Hamming 1989, Kumar 1996, Rabiner 1975 and Smyth 2007]. However, conventional digital filters have several drawbacks in the displacement reconstruction for low-frequency dominant structures. The IIR filters usually require initial conditions on displacement and velocity, which are generally unavailable. Low-frequency noise components in measured accelerations are amplified and propagate through time. Although some remedies have been proposed to suppress low-frequency noise, they either cause nonlinear phase errors [Hamming 1989, Kumar 1996 and Rabiner 1975], or require additional pieces of information [Smyth 2007]. In the case of FIR filters, it is difficult to approximate the analytic transfer function in a low-frequency range accurately by a finite Fourier series due to the singularity of the analytic transfer function at the zero frequency [Hamming 1989 and Kumar 1996].

The frequency domain integration approach (FDIA) is a possible alternative to digital filters for the displacement reconstruction [Lee 2010]. The time-history of

2

displacement is obtained using the inverse Fourier transform on the discrete Fourier transform (DFT) of measured accelerations multiplied by the analytic transfer function which will be defined in chapter 2. This approach, however, suffers from severe discretization errors if the DFT of the measured acceleration is performed on relatively a short time interval [Hamming 1989]. This is a major drawback for the real-time or near real-time reconstruction required in the SHM or the SC.

The current study formulates a new class of the displacement reconstruction scheme, which is suitable to low-frequency dominant structures, as a boundary value problem using measured acceleration without any information on initial conditions. The displacement is reconstructed through an inverse problem defined as the minimization of the least squared errors between measured acceleration and the second-order time derivative of displacement within a time interval, referred to as a time window. An overlapping time-window concept proposed by Park *et al*. [2008] is adopted to enhance the accuracy of reconstructed displacement.

Two major difficulties should be properly addressed to reconstruct displacement from acceleration based on the inverse problem. First, the reconstruction problem becomes rank-deficient because the boundary conditions at both ends of each time window are not known *a priori*. Furthermore, a small amount of low-frequency spectral noise in measured accelerations may significantly pollute the reconstructed displacement with physically inadmissible components, which is known as the ill-posedness of inverse problems. The Tikhonov regularization

scheme, which has been widely used in various types of inverse problems [Hansen 1988 and Park 2001], is utilized to overcome these difficulties.

The governing equation of the inverse problem is obtained by taking variation of the regularized minimization problem, which leads to the same type of differential equation as that of a beam on an elastic foundation (BEF) [Hetenyi 1946]. The transfer function of the inverse problem is hereafter referred to as the BEF transfer function. The exact relation between the regularization factor and the accuracy of the proposed filter is established through the desired accuracy at the target frequency which is the lowest frequency in physically meaningful frequency contents in measured acceleration.

The current thesis proposes three types of FIR filter, the CFIR filter, the FDM-FIR filter and the FEM-FIR (FFIR) filter based on the inverse problem formulated with a form of the BEF function. Two filter sizes are proposed for the CFIR filter from the viewpoint of the stability independently to the regularization factor. As the BEF transfer function is capable of suppressing noise components below the target frequency, the FDIA using the BEF transfer function dose not require low-cut filter or and band-pass filter.

The coefficients of the CFIR filter is obtained by approximating the BEF-transfer function with the Fourier series in the frequency domain, while the coefficients of the FDM-FIR and the FFIR filters are obtained by discretizing the inverse problem with the standard finite difference method and finite element method in the time domain, respectively. The proposed filters have their own merits and

disadvantages in relation to each other. The filter size can be selected arbitrarily for the FDM-FIR filter and the FFIR filter, while the uniform frequency responses are expected in the CFIR filter for the proposed filter sizes. The FDM-FIR filter needs relatively small computational time than other filters. A great advantage of the FFIR filter over the FDM-FIR filter and the CFIR filter is that velocity as well as displacement can be reconstructed simultaneously as the velocity field is embedded in the finite element model of the FFIR filter. The characteristics of the proposed FIR filters are presented and discussed in detail by investigating the transfer function and accuracy function.

Five examples are presented for demonstrating the validity of the proposed filters. Various characteristics of the FDIA, CFIR filter and FFIR filter are verified with reconstructed displacement and velocity from numerically simulated accelerations in the first example. Displacements are reconstructed from the accelerations measured from the small cantilever beam and the real-scale stay cable in laboratory, and are compared with the measured displacement in the second and third examples, respectively. In the forth example, the displacement reconstruction is employed for the accelerations measured in a simply supported railroad bridge during commercial operation, and is compared with the measured one.

The last example presents the evaluation of the flutter derivatives using the reconstructed responses together with the measured acceleration, this example is not just the verification of the reconstruction itself but the further application of the reconstructed responses to the other SI scheme. Moreover, it contains new SI al-

5

gorithms for the identification of the flutter derivatives and the valuable discussion about the aeroelastic phenomena and the experimental procedure for the extraction of flutter derivatives.   Hence, the last example organizes the separated chapter of 4.

2. Displacement Reconstruction for Dynamic Acceleration

Numerous attempts have been made to reconstruct displacement with measured acceleration based on the definition of acceleration, i.e., the second-order derivative of displacement in a time domain. Time integration schemes based on time-marching algorithms such as a Newmark's method and a third-order corrector are probably the most straightforward and easiest way to obtain displacement from measured acceleration. However, the time-marching algorithms yield erroneous displacement [Boore 1997 and Smyth 2007] caused by the following facts. First of all, initial conditions on velocity and displacement required in the time-marching algorithms are usually unavailable or inaccurate in real situations. Moreover, random noise in measured acceleration data causes physically inadmissible errors in the reconstructed displacement. Particularly, low-frequency spectral components in random noise are amplified during time-marching procedures, which severely deteriorate the accuracy of the reconstructed displacement [Hong 2010 and Lee 2010]. This undesirable effect becomes a critical issue in the displacement reconstruction for large-scale civil infrastructures, which usually exhibit very low fundamental frequencies [Smyth 2007].

Several remedies to overcome the drawbacks of the time-marching algorithms have been proposed for the displacement reconstruction with measured accelera-

tion. A baseline correction technique used in seismology applications is a well-known approach for eliminating the erroneous components in the reconstructed displacement by the time-marching algorithms [Boore 1997, Chiu 1997, Iwan 1985 and Stephens 1985]. In this approach, polynomial functions approximately representing the inadmissible errors are constructed, and are subtracted from the reconstructed displacement. However, the baseline correction depends on an engineer's decision, and thus is inadequate to SHM and SC applications [Sohn 2004 and Housner 1997] in which measured acceleration should be automatically processed in real time or pseudo-real time. Moreover, this approach corrects erroneous results obtained by the time-marching algorithms, and is not completely free of the aforementioned drawbacks. For SHM applications, Smyth and Wu (2007) combine displacement data from a global positioning system (GPS) with measured acceleration, and reconstruct displacement through the multi-rate Kalman filter approach [Smyth 2007]. However, their approach is not applicable for the displacement reconstruction at positions where the GPS signals are unable to reach. In addition, the low accuracy in the vertical positioning capability of the GPS may act as an additional source of noise in the reconstruction of vertical displacement.

2.1 The Exact Governing Equation and Transfer Function

This thesis formulates a new class of the displacement reconstruction scheme as a boundary value problem rather than an initial value problem using measured acceleration without any information on initial conditions. In case measured accelerations are given over a finite time interval referred to as a time window [Park 2008 and Lee 2010], the relation between the measured acceleration and the definition of acceleration forms a boundary value problem. As the second-order time derivative of displacement is acceleration, the displacement is reconstructed through the minimization of the least squared errors between measured acceleration and the second-order time derivative of displacement in a time window.

As the reconstruction problem of displacement is defined as a boundary value problem in a time window, boundary conditions at both ends of the domain should be specified to solve the minimization problem, but neither displacement nor velocity is known at the boundaries. Therefore, the minimization problem for the reconstruction of displacement becomes ill-posed or rank-deficient, and cannot be solved for unknown displacement in a time window. Furthermore, a small amount of low-frequency spectral noise in measured acceleration data may significantly pollute the reconstructed displacement as like to the reconstruction with the time-marching algorithm. To overcome these two difficulties, the Tikhonov regularization scheme [Hansen 1988 and Park 2001], which has been widely employed to alleviate the ill-posedness of inverse problems, is adopted.

2.1.1 Displacement Reconstruction Scheme as an Initial Value Problem

Dynamic structural responses such as acceleration, velocity and displacement are calculated by solving the following equation of motion of a structure with proper initial conditions [Chopra 2000].

$$\mathbf{M}\mathbf{a}(t) + \mathbf{C}\mathbf{v}(t) + \mathbf{K}\mathbf{u}(t) = \mathbf{p}(t), \quad \mathbf{v}(0) = \mathbf{v}_0 \quad \text{and} \quad \mathbf{u}(0) = \mathbf{u}_0 \qquad (2\text{-}1)$$

where $\mathbf{M}$, $\mathbf{C}$, $\mathbf{K}$, and $\mathbf{p}$ represent the mass, damping, stiffness matrix of a structure and a load vector imposed on the structure, respectively, while $\mathbf{a}$, $\mathbf{v}$ and $\mathbf{u}$ denote the acceleration, velocity and displacement of the structure, respectively. The prescribed initial conditions for velocity and displacement are given as $\mathbf{v}_0$ and $\mathbf{u}_0$, respectively. The equation of motion given in Eq. (2-1) is the system of an initial value problem in time domain, and represents a physical phenomenon that the specified initial conditions propagate through time.

To solve Eq. (2-1) numerically, a time integration scheme based on a time-marching algorithm is employed to express displacement and velocity in terms of acceleration. The propagating characteristics of Eq. (2-1) should be properly considered in a time integration scheme. Several well-formulated time-integration schemes have been proposed and successfully applied to various types of dynamic problems.

Backward difference:

$$(2\text{-}2\text{-}a)$$

$$v_i = v_{i-1} + a_{i-1}\Delta t$$
$$u_i = u_{i-1} + v_{i-1}\Delta t$$

Forward difference:

$$v_i = v_{i-1} + a_i\Delta t$$
$$u_i = u_{i-1} + v_i\Delta t$$

(2-2-b)

Backward trapezoid rule:

$$v_i = v_{i-1} + \frac{1}{2}(a_{i-1} + a_i)\Delta t$$

$$u_i = u_{i-1} + \frac{1}{2}(v_{i-1} + v_i)\Delta t$$

(2-2-c)

Third order corrector:

$$v_i = v_{i-1} + \frac{\Delta t}{12}(5a_i + 8a_{i-1} - a_{i-2})$$

$$u_i = u_{i-1} + \frac{\Delta t}{12}(5v_i + 8v_{i-1} - v_{i-2})$$

(2-2-d)

Newmark's method:

$$v_i = v_{i-1} + ((1-\gamma_N)a_{i-1} + \gamma_N a_i)\Delta t$$

(2-2-e)

$$u_i = u_{i-1} + (\Delta t)v_{i-1} + ((0.5-\beta_N)a_{i-1} + \beta_N a_i)(\Delta t)^2$$

where subscript i denotes a discrete time step, $a_k = a(k\Delta t)$, $v_k = v(k\Delta t)$ and

$u_k = u(k\Delta t)$ represent the acceleration, velocity and displacement of the structure,

Δt is a step length for the time-marching algorithm, which is often referred to as a

time increment or a sampling size, while β_N and γ_N represent numerical pa-

rameters for Newmark's method [Chopra 2000], which define the variation of ac-

celeration over a time step, respectively.

Once displacement and velocity are expressed in terms of acceleration using the time-marching algorithms in Eq. (2-2) for current and previous time steps, Eq. (2-1) is solved for acceleration. As the above procedure is applied stepwise, the entire histories of dynamic responses of a structure are calculated.

In case the initial conditions are known in previous and acceleration at a fixed material point is measured at every discrete time step with the time increment of Δt, the displacement at the point is calculated by use of Eq. (2-2) in theory. As one of the dynamic responses, the acceleration, is measured and thus known, the system information in Eq. (2-1) is not required, but only the relationship between displacement and acceleration, i.e., Eq. (2-2) is utilized to calculate displacement.

As mentioned at the beginning of this chapter, there exist two major drawbacks in the application of Eq. (2-2) for reconstructing displacement with measured acceleration. First of all, the initial conditions are generally not given, especially, for large-scale structures such as bridges and buildings. The second drawback is that noise in the initial conditions and measured accelerations not only propagate through time but also are severely amplified. This is because the time integration scheme given in Eq. (2-2) is developed to describe the propagating characteristics of the initial value problems accurately, and thus noise in measurement as well as true information on a dynamic system propagates [Hong 2010 and Lee 2010].

Among the algorithms in Eq. (2-2), the most popular one in the civil engineering field may be the Newmark's method, hence, all discussions about time-

marching algorithms are represented by Newmark's method in equation (2-2-e) hereafter.

To investigate propagating characteristics of Eq. (2-2-e), the velocity is eliminated from the equations, and the displacement is expressed in terms of the initial conditions and measured acceleration.

$$
\begin{aligned}
u_k = u_0 &+ k\Delta t v_0 - k(\Delta t)^2 \gamma_N a_0 + (\Delta t)^2 \beta_N (a_k - a_0) \\
&+ (\gamma_N + \frac{1}{2})(\Delta t)^2 S_{k-1} + (\Delta t)^2 \sum_{p=1}^{k-1} S_{p-1}
\end{aligned}
\quad , \quad k \geq 1
\tag{2-3}
$$

where $S_k = \sum_{i=0}^{k} a_i$. From Eq. (2-3), it is clearly seen that noise in the initial displacement propagates though time while noise in the initial velocity and acceleration are amplified linearly and quadratically, respectively.

In case noise components in measured acceleration are random with zero mean, noise in term S_{k-1} may vanish. However, the last term in Eq. (2-3) causes the accumulation of noise, which is explained by expressing the term for measured accelerations.

$$
\begin{aligned}
(\Delta t)^2 \sum_{p=1}^{k-1} S_{p-1} &= (\Delta t)^2 (a_0 + (a_0 + a_1) + \cdots + (a_0 + a_1 + a_2 \cdots + a_{k-2})) \\
&= \Delta t \sum_{p=1}^{k-1} \Delta t (k - p) a_{i-1}
\end{aligned}
\tag{2-4}
$$

13

$k = 40\,\text{N/m}$ $m = 1\,\text{kg}$

$f \approx 1\,\text{Hz}$ $u_0 = 1\,\text{m}$, $v_0 = 0\,\text{m/sec}$
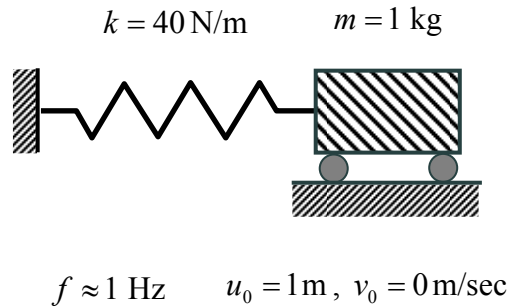
Figure 2-1. A single DOF system

Obviously, noise in accelerations measured in the past becomes larger rather than canceling out as time passes by. It may be concluded that the application of a time integration scheme for the initial value problem to the displacement recon-struction yields noise-polluted, meaningless results. More precise and accurate discussion about noise amplification will be discussed in the Chapter 3 with fre-quency domain analysis.

The aforementioned characteristics of the Newmark's method are demonstrat-ed through a simple numerical simulation study on a single DOF system shown in Fig. 2-1. The integration constant for the Newmark's method, $\beta_N = 1/4$, $\gamma_N = 1/2$, are used [Chopra 2000]. The natural frequency of the system is about 1Hz, and the exact initial condition for displacement and velocity are 1.0 m and 0.0 m/sec, respectively. The reconstructed displacement for the initial displacement of 1.2 m by Newmark's method is compared with the exact displacement in Fig. 2-2(a), which shows that the noise in the initial displacement propagates through time.

14
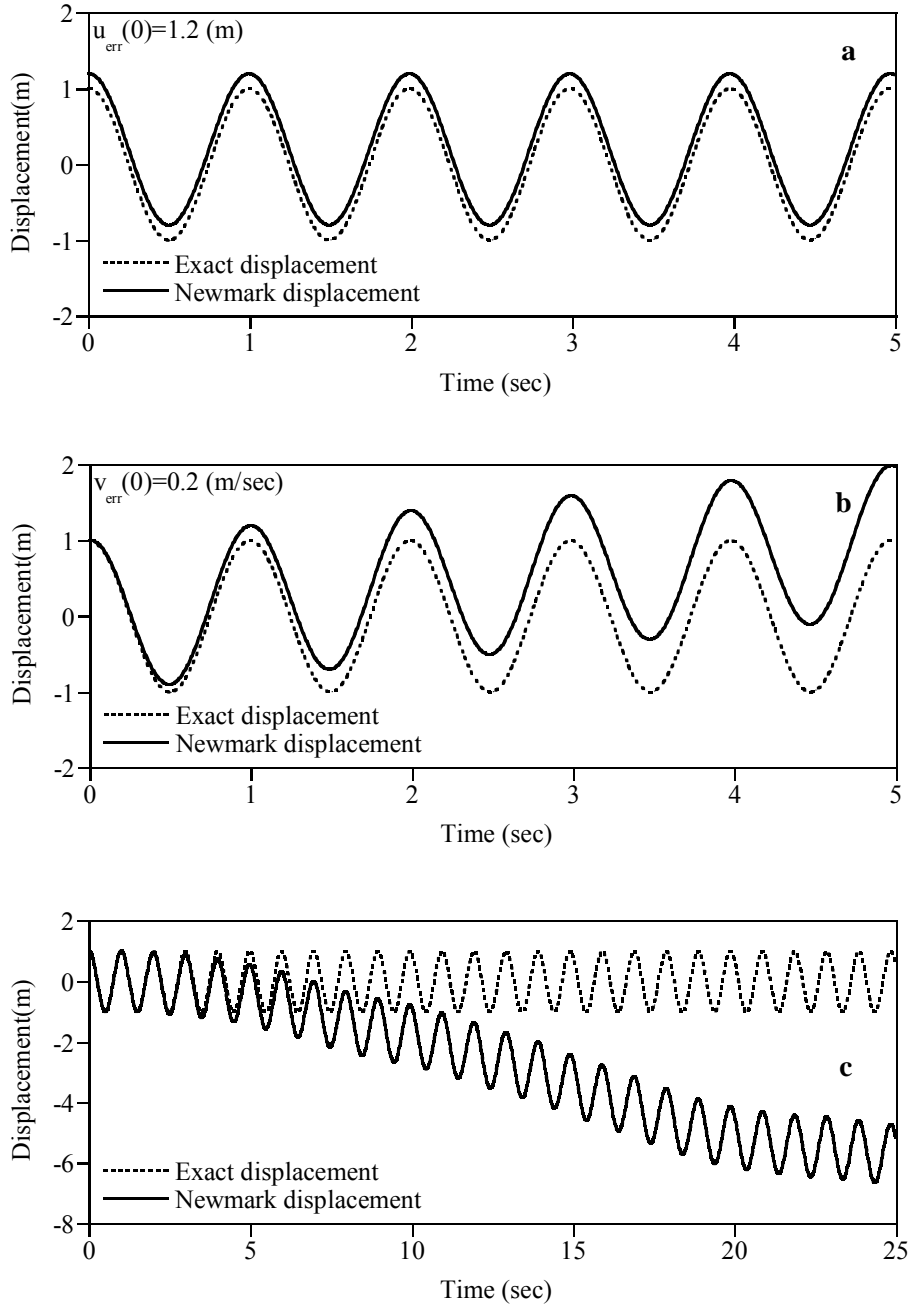
Figure 2-2. Reconstructed displacement by Newmark's method : (a) Noise in the initial displacement. (b) Noise in the initial velocity. (c) 5% random proportional noise in measured acceleration

15

The noise of 0.2 m/sec in the initial velocity causes linearly increasing displacement in the Newmark's method as illustrated in Fig. 2-2(b). Finally, Fig. 2-2(c) shows that the Newmark's method yields almost meaningless displacement in case the measured acceleration is polluted by 5% random proportional noise.

2.1.2 Displacement Reconstruction Scheme as a Boundary Value Problem

In this section, a new approach to reconstruct displacement with measured acceleration is presented as a boundary value problem. Suppose acceleration at a fixed material point is completely measured during a time interval (or a time window), $T_1 < t < T_2$, and thus known. By definition, the acceleration of a fixed material point, $a(t)$, is expressed in terms of displacement through a second order ordinary differential equation.

$$a(t) \equiv \frac{d^2 u(t)}{dt^2} \approx \bar{a}(t) \qquad T_1 < t < T_2 \qquad (2\text{-}5)$$

where $u(t)$ and $\bar{a}(t)$ are and displacement and measured acceleration, respectively. As only the dynamic information is utilized for the displacement reconstruction in this thesis, the displacement in Eq. (2-5) represents the dynamic component measured from the static equilibrium position of a structure.

Provided that proper boundary conditions on displacement or velocity at $t = T_1$ and $t = T_2$ are given, the displacement is easily obtained by integrating Eq. (2-5) twice and applying two boundary conditions. This study utilizes the

16

following minimization problem rather than attempts to solve Eq. (2-5) directly.

$$\operatorname*{Min}_{u} \Pi_E(u) = \frac{1}{2} \int_{T_1}^{T_2} (a(u(t)) - \bar{a})^2 \, dt \qquad (2\text{-}6)$$

where Π_E is error function of acceleration, and subscript 'E' denotes 'error'. Since, however, the boundary conditions for Eq. (2-5) are generally not known, the displacement field cannot be determined by integrating Eq. (2-5) twice. Furthermore, random noise components included in the measurement should be properly taken care of in the displacement reconstruction with Eq. (2-5).

The homogenous solution of Eq. (2-5) is given as a linear function in time. Since, however, the real dynamic displacement induced by structural vibration is defined with harmonic functions through the Duhamel integral [Chopra 2000], a linear function is not an adequate basis for the dynamic displacement induced by structural vibration. Therefore, the homogeneous solution should vanish, and the solution of Eq. (2-5) is expressed solely by the particular solution. Note that the displacements at the boundaries of a time window are determined by the particular solution rather than specified as boundary conditions.

The particular solution of Eq. (2-5) can be found through the Fourier transform [Rabiner 1975]. The transfer function of Eq. (2-5) is also derived by this transform procedure.

$$F(u(t)) = H_E(\omega)F(\overline{a}(t)) = -\frac{1}{\omega^2}F(\overline{a}(t)) \qquad (2\text{-}7)$$

where F and $H_E = -1/\omega^2$ denote the Fourier transform and the exact transfer function of the second order ordinary differential equation in Eq. (2-5), respectively, while ω is the angular frequency. Here, the exact transfer function implies the transfer function of the exact governing differential equation between displacement and acceleration.

Theoretically, the time history of displacement is obtained by applying the inverse Fourier transform to Eq. (2-7).

$$u(t) = -F^{-1}(\frac{1}{\omega^2}F(\overline{a}(t))) \qquad (2\text{-}8)$$

where F^{-1} represents the inverse Fourier transform. The displacement reconstruction scheme defined in (2-8) is referred to as the frequency domain integration approach (FDIA) [Hong 2010 and Lee 2010] hereafter.

In case the measured acceleration contains random noise, pure noise frequency contents in measured accelerations below the target frequency [Lee 2010 and Hong 2010], which is the lowest frequency in physically meaningful frequency contents in measured acceleration, are severely amplified by the exact transfer function in the frequency domain. Consequently, the reconstructed displacement in the time domain is polluted with the amplified noise components. Here, the

target frequency is easily determined by investigating the Fourier transform of measured accelerations or just by the engineer's decision in practical problems.

Even if measured accelerations are noise-free, the FDIA defined in Eq. (2-8) can not be directly applied to reconstruct displacement. Since the Fourier transform of measured accelerations in Eq. (2-8) is performed on the finite time interval and the acceleration is measured in discretized sense, the Fourier transform (discrete Fourier transform, more precisely) contains frequency responses below the target frequency [Rabiner 1975 and Hamming 1989], which should not exist, by truncation and discretization errors. These errors act as an additional source of noise, and thus pollute the reconstructed displacement in the time domain similar to the random measurement noise. To suppress the measurement noise and the truncation error below the target frequency, low cut filters or band pass filters are usually applied to Eq. (2-8) before performing the inverse Fourier transform.

$$u(t) = -F^{-1}(\frac{1}{\omega^2}\phi(\omega)F(\overline{a}(t)))$$ (2-9)

where ϕ is a proper weighting function for a low cut filter or a band pass filter. The Fourier transform in Eq. (2-9) holds for infinite and continuously measured acceleration. Since, however, the finite and discretized acceleration with the constant time step, Δt, is measured in real situation, the Fourier transform in Eq. (2-9) should be implemented by the discrete Fourier transform (DFT) which inevitably contains the truncation and discretization errors. If the measured acceleration

19

is long enough to ignore these errors, the displacement can be reconstructed by the

FDIA with proper weighted transfer function.

2.2 The Governing Equation and Transfer function of an Regularized Inverse Problem

As proper boundary conditions are not specified for Eq. (2-5), the minimization problem in Eq. (2-6) becomes ill-posed and unable to yield a unique displacement for given measured acceleration due to rank-deficiency. To solve ill-posed problems, the regularization techniques, in which *a priori* estimates of solutions are defined by a regularity condition as additional information, are widely adopted [Hansen 1988 and Park 2001]. The reconstructed displacement should stay around the static displacement of a given system, u_{st}, which is expressed by the following equation.

$$\Pi_R(u) = \frac{1}{2} \int_{T_1}^{T_2} (u(t) - u_{st}(t))^2 \, dt \le r^2 < \infty \tag{2-10}$$

where Π_R is a regularization function, and *r* defines a solution bound.

As the static displacement has no effect on the acceleration defined in Eq. (2-5), only the dynamic component in the total displacement can be reconstructed. Therefore, the displacements in Eq. (2-6) and (2-10) represent the dynamic displacement measured from the static equilibrium position of a structural system, and the static displacement in Eq. (2-10) should be set to zero, which leads to the following expression

$$\Pi_R(u) = \frac{1}{2}\int_{T_1}^{T_2}(u(t))^2\,dt \leq r^2 < \infty \qquad\qquad (2\text{-}11)$$

Since the solution bound is not known a priori, the regularity condition Eq. (2-11) is enforced as a penalty function to the original minimization problem in Eq. (2-6) [Kang 2005].

$$\operatorname*{Min}_{u}\Pi(u) = \Pi_E(u) + \Pi_R(u) = \frac{1}{2}\int_{T_1}^{T_2}\left(\frac{d^2u}{dt^2} - \overline{a}\right)^2 dt + \frac{\beta^2}{2}\int_{T_1}^{T_2}u^2\,dt \qquad (2\text{-}12)$$

The above minimization problem is generally known as the Tikhonov regularization scheme [Hansen 1988 and Park 2001]. The penalty number β in Eq. (2-12) is usually referred to as the regularization factor that adjusts the degree of the regularization in the minimization problem. As the regularization factor becomes larger, the solution bound approaches zero, and zero displacements are reconstructed. Meanwhile, a small regularization factor yields an ill-conditioned problem for Eq. (2-12), which may result in a meaningless and/or unstable solution. Therefore, a well-balanced regularization factor should be selected to obtain physically meaningful and accurate displacements [Park 2001].

The governing equation and the boundary conditions associated with the minimization problem is obtained by taking the variation to the object function in Eq. (2-12)

$$\delta\Pi(u) = \int_{T_1}^{T_2} \frac{d^2\delta u}{dt^2}(\frac{d^2 u}{dt^2} - \overline{a})dt + \beta^2 \int_{T_1}^{T_2} \delta u u \, dt = 0 \qquad (2\text{-}13)$$

The integration of the first term of Eq. (2-13) by parts twice leads to the following equation.

$$\int_{T_1}^{T_2} \delta u(\frac{d^4 u}{dt^4} + \beta^2 u - \frac{d^2\overline{a}}{dt^2})dt + \frac{d\delta u}{dt}(\frac{d^2 u}{dt^2} - \overline{a})\Big|_{T_1}^{T_2} - \delta u(\frac{d^3 u}{dt^3} - \frac{d\overline{a}}{dt})\Big|_{T_1}^{T_2} = 0 \quad (2\text{-}14)$$

Based on the above variational statement, the governing equation and the boundary conditions of the minimization problem are defined as follows

$$\text{G.E.: } \frac{d^4 u}{dt^4} + \beta^2 u = \frac{d^2\overline{a}}{dt^2} \quad T_1 < t < T_2$$

$$\text{B.C.: } \frac{d^2 u}{dt^2} = \overline{a}, \ \frac{d^3 u}{dt^3} = \frac{d\overline{a}}{dt} \quad \text{at } t = T_1, T_2 \qquad (2\text{-}15)$$

Since the displacements and the velocity are unknown at the boundaries, the Neumann type boundary conditions [Cheng 2005] are adopted. The governing equation in Eq. (2-15) is the same as that of a beam on an elastic foundation (BEF) [Hetenyi 1946]. Hence the problem in Eq. (2-15) is referred to as the BEF problem hereafter. The existence and uniqueness of the solution can be guaranteed with only the Neumann type boundary conditions by virtue of the second term of the left-hand side of the governing equation, which comes from the regularization function.

23

The transfer function of the governing equation in Eq. (2-15), which is abbreviated to the BEF transfer function, is derived by applying the Fourier transform.

$$H_B(\omega) = -\frac{\omega^2}{\omega^4 + \beta^2} = -\frac{(2\pi f)^2}{(2\pi f)^4 + \beta^2} \qquad (2\text{-}16)$$

where f is the frequency and H_B denotes the BEF transfer function. The time-history of displacement can be reconstructed by the FDIA with the BEF transfer function.

$$u(t) = F^{-1}(H_B(\omega)F(\overline{a}(t))) = -F^{-1}(\frac{\omega^2}{\omega^4 + \beta^2}F(\overline{a}(t))) \qquad (2\text{-}17)$$

Since the BEF transfer function by itself is capable of suppressing noise components below the target frequency, it is not necessary to apply an additional band filter to the FDIA defined in Eq. (2-17).

It is rather convenient to express the exact transfer function and the BEF transfer function in terms of the dimensionless frequency normalized to the target frequency. For example, the exact transfer function defined in Eq. (2-7) is normalized as follows.

$$\widetilde{H}_E(\widetilde{f}) = -\frac{H_E(\omega)}{1/(2\pi f_T)^2} = -\frac{-1/(2\pi f)^2}{1/(2\pi f_T)^2} = \frac{1}{\widetilde{f}^2} \qquad (2\text{-}18)$$

where $\widetilde{H}_E$, f_T and $\widetilde{f} = f/f_T$ are the normalized exact transfer function, the target frequency and the dimensionless frequency normalized to the target frequen-

cy, respectively. The normalized exact transfer function yields 1 at $\widetilde{f} = 1$, where frequency is equal to the target frequency, while the un-normalized exact transfer function becomes 1 at $f = 1/2\pi$. Since the performance of proposed reconstruction scheme is focused on the frequency region near the target frequency, the normalization presented in Eq. (2-18) is a very convenient tool for representation and comparisons for the transfer functions.

The normalized BEF transfer function is derived by applying the same normalization scheme to the BEF transfer function in Eq. (2-17)

$$\widetilde{H}_B(\widetilde{f}) = -\frac{H_B(\omega)}{1/(2\pi f_T)^2} = \frac{(2\pi f)^2 /(2\pi f_T)^2}{((2\pi f)^4 + \beta^2)/(2\pi f_T)^4} = \frac{\widetilde{f}^2}{(\widetilde{f}^4 + \beta^2 /(2\pi f_T)^4)} \quad (2\text{-}19)$$

where $\widetilde{H}_B$ is the normalized BEF transfer function. The term "normalized" is hereafter omitted for brevity of explanation, unless otherwise stated.

The accuracy of the reconstructed displacement is defined with the accuracy function [Hamming 1989 and Smyth 2007], which is the ratio of the transfer function used in the displacement reconstruction to the exact transfer function [Hong 2010 and Lee 2010]. The accuracy function of the exact transfer function, $H_E^{acc}(\omega)$, and the BEF transfer function, $H_B^{acc}(\omega)$, are defined as follows.

$$H_E^{acc}(\omega) = \frac{H_E}{H_E} = 1 \quad (2\text{-}20)$$

$$H_B^{acc}(\omega) = \frac{H_B}{H_E} = \frac{\omega^4}{\omega^4 + \beta^2} = \frac{\tilde{f}^4}{(\tilde{f}^4 + \beta^2/(2\pi f_T)^4)} \tag{2-21}$$

The exact accuracy function in Eq. (2-20) always yields 1 regardless of the frequency. On the other hand, the BEF accuracy function in Eq. (2-21) becomes 0 at $\tilde{f} = 0$, and rapidly converges to 1 as the frequency approaches to the target frequency. The transition characteristics of the BEF transfer function in $0 \leq \tilde{f} \leq 1$ are governed by the magnitude of the regularization factor. The accuracy at the target frequency is obtained by setting $\tilde{f} = 1$ in Eq. (2-21).

$$\alpha_T = \frac{1}{1 + \beta^2/(2\pi f_T)^4} \tag{2-22}$$

where α_T is the target accuracy, *i.e.*, the desired accuracy for the reconstructed displacement of the frequency component corresponding to the target frequency. If the target accuracy is pre-selected based on an engineering sense, the regularization factor is determined by the following equation.

$$\beta = \sqrt{\frac{1-\alpha_T}{\alpha_T}}(2\pi f_T)^2 = \lambda^2(\alpha_T)(2\pi f_T)^2 \quad 0 \leq \alpha_T \leq 1 \tag{2-23}$$

where $\lambda^4(\alpha_T) = (1-\alpha_T)/\alpha_T$. Substitution of Eq. (2-23) into Eq. (2-19) and Eq. (2-21) leads to the following expressions, respectively.
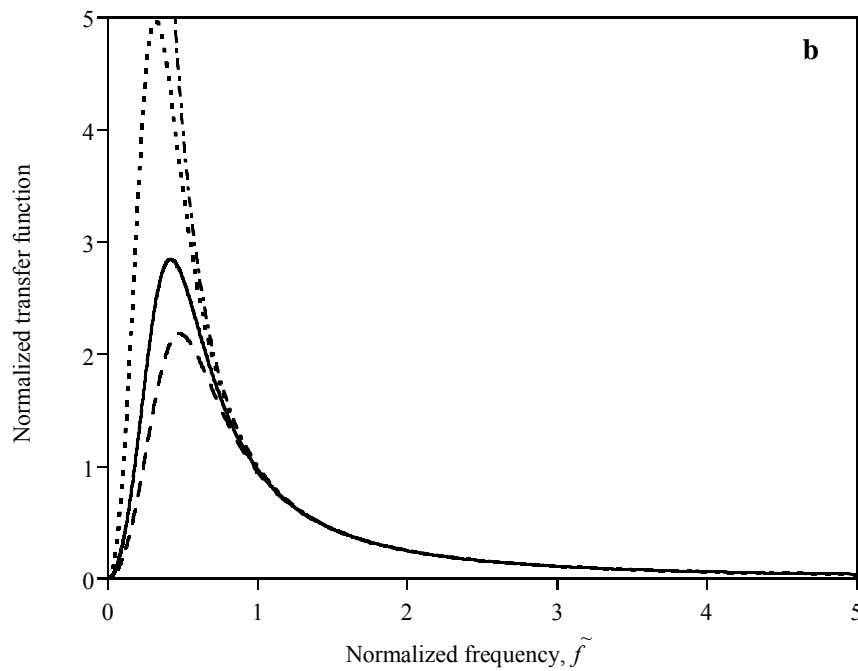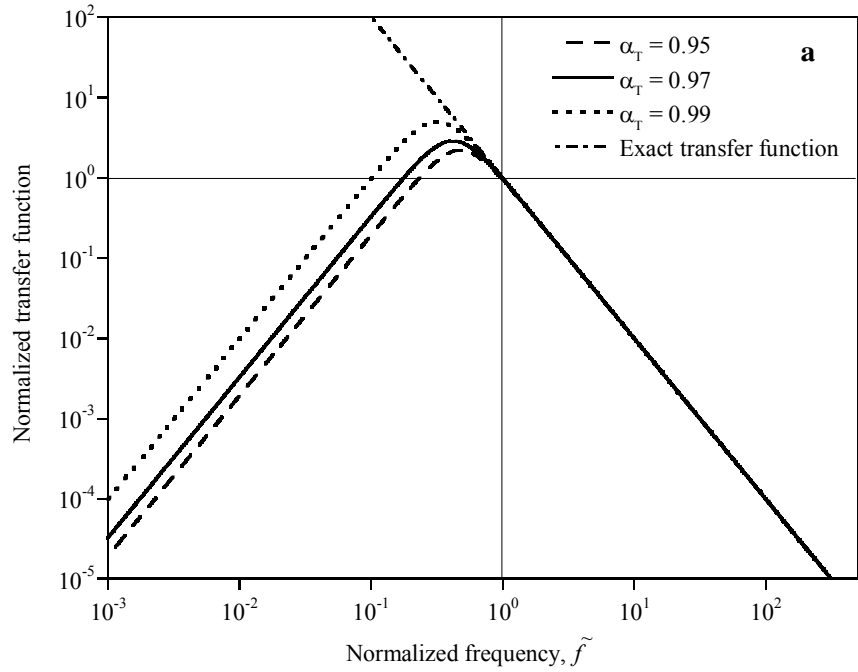
Figure 2-3. BEF transfer functions for various levels of the target accuracy: (a) Log-log scale. (b) Detail in a linear scale
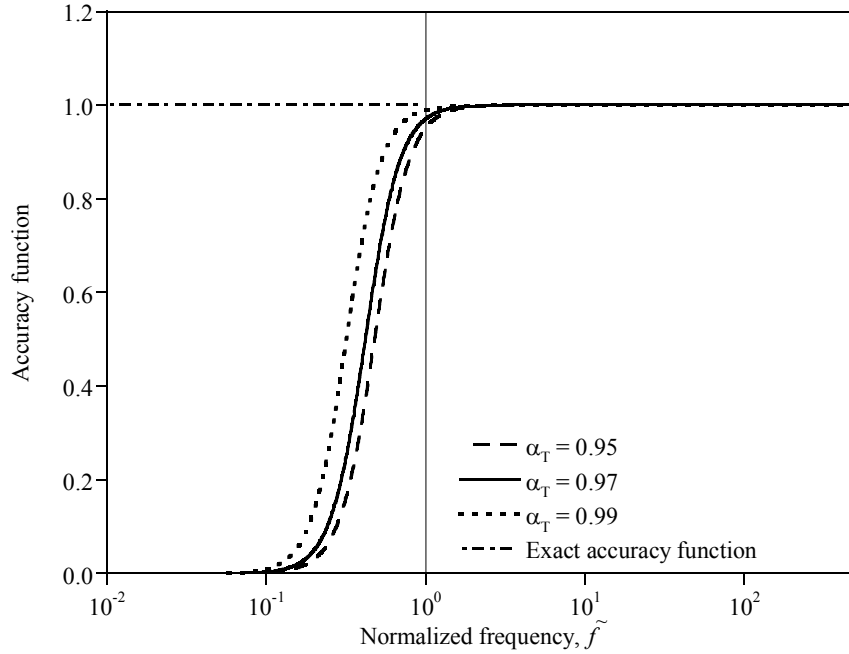
Figure 2-4. Accuracy functions for various levels of the target accuracy

$$\widetilde{H}_B(\widetilde{f}) = \frac{\widetilde{f}^2}{\widetilde{f}^4 + \lambda^4(\alpha_T)} \qquad (2\text{-}24)$$

$$H_B^{acc}(\widetilde{f}) = \frac{\widetilde{f}^4}{\widetilde{f}^4 + \lambda^4(\alpha_T)} \qquad (2\text{-}25)$$

The BEF transfer functions and the accuracy functions for various levels of target accuracy are drawn in Fig. 2-3 and Fig. 2-4, respectively, along with the exact transfer function. The BEF transfer function begins to decrease quickly below the target frequency while the exact transfer function keeps increasing as the frequency approaches to zero. For frequency ranges larger than the target frequency,

the BEF transfer function and the exact transfer function are almost identical regardless of the target accuracy.   Therefore, the FDIA with the BEF transfer function is able to reconstruct the displacement components for $\tilde{f} \geq 1$.   Meanwhile, the BEF transfer function suppresses the acceleration components below the target frequency, which are merely measurement noises, in the displacement reconstruction.   The degree of the noise suppression becomes stronger as the frequency approaches zero.   Higher target accuracy yields weaker noise-suppression capability of the BEF transfer function, and vice versa as shown in Fig. 2-3 and 2-4.   As an apparent trade-off between the accuracy at the target frequency and the noise-suppression exists in the selection of the target accuracy, the optimal target accuracy depends on a specific problem.   For example, in case the noise level of measured accelerations is expected to be high, lower target accuracy may be adequate to provide strong noise suppression capability to the BEF transfer function.   The target accuracy of 0.97 is selected for all forthcoming discussions in this study.

3. Design of FIR FILTERS

As acceleration is measured discretely by a uniform time interval Δt in actual situations as illustrated in Fig. 3-1, the reconstruction should be implemented in discretized form.   In the digital filter field, the discretized relationship between input acceleration and output displacement has a meaning of the digital filter.   In this chapter, the displacement reconstruction defined with the BEF problem in the previous section is designed by the finite impulse response (FIR) filter for the practical real-time or near real-time processing.

The digital filters define the relationships between discrete input values and a discrete output values.   In the context of this thesis, the input values and output values refer to the measured accelerations and the reconstructed displacements, respectively.   From the filter theory, displacements could be reconstructed from measured accelerations using various types of digital filters.
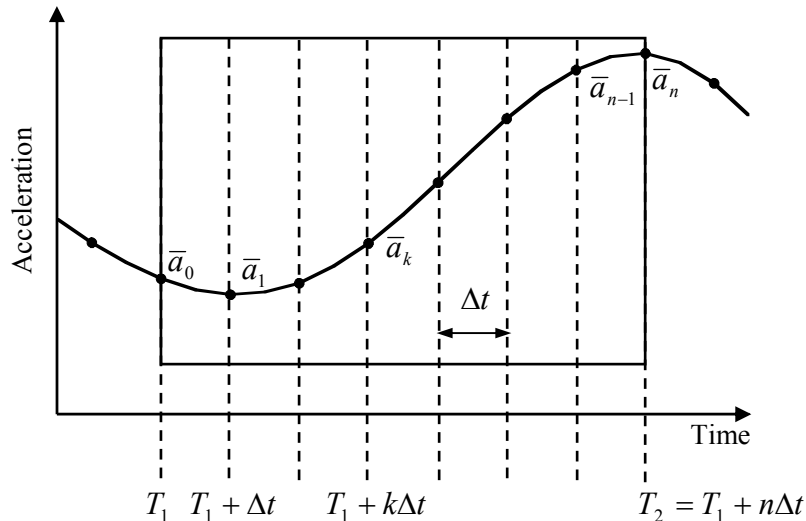
Figure 3-1. Definition of measured accelerations at discrete time steps

31

Among them, infinite impulse response (IIR) filters and FIR filters have been successfully applied in numerous fields [Kumer 1996, Boore 1997 and Smyth 2007]. An IIR filter and an FIR filter are often referred to as a recursive filter and a non-recursive filter, respectively. An IIR filter utilizes output values (displacements) as well as input values (accelerations) to define output values while an FIR filter expresses output values in terms of input values only. Unfortunately, however, it is difficult to reconstruct displacements from measured accelerations with the conventional digital filters for various reasons in low-frequency dominant structures.

Numerical integration schemes in Eq. (2-2) are a type of IIR filter [Boore 1997]. Namely, these time marching algorithms adopted in structural dynamics require the output of the previous steps to define the output of the present step. As mentioned in section 2.1.1 the IIR filters have several shortcomings when a displacement is reconstructed from a measured accelerations. First of all, initial conditions on velocity and displacement, which are usually unavailable in real situations, are required. Moreover, low-frequency components in random noise are amplified in the IIR filters, and thus severely deteriorate the accuracy of the reconstructed displacement [Rabiner 1975] as discussed in the previous chapter. This undesirable effect becomes a critical issue in the displacement reconstruction for a low-frequency dominant structure. In case noise-suppressing algorithms are introduced in the IIR filters, nonlinear phase errors are inevitably included in the reconstructed displacements [Bardella 2003, Boore 1997, Kumer 1996 and Smyth

2007].   Several remedies to overcome the drawbacks of the IIR filters with the time-marching algorithm have been proposed for the displacement reconstruction [Boore 1997, Chiu 1997, Iwan 1985 and Stephens].   However, since the remedies try to correct erroneous results obtained by the IIR filters with additional pieces of information on displacement or filtering operations, they are not completely free of the drawbacks of the IIR filters.   To date, a reliable IIR filter for the reconstruction of displacement with measured acceleration alone has rarely been reported.

The FIR filters approximate displacement as a linear combination of measured accelerations.   The coefficients of the FIR filters are usually defined as the coefficients of the finite Fourier series of transfer functions in the frequency domain [Hamming 1989, Oppenheim 1999 and Rabiner 1975].   Due to the singularity of the exact transfer function in Eq. (2.8) at the zero frequency, the maximum flatness criterion, rather than the standard least square approach is employed to calculate the coefficients of the FIR filters [Kumar 1996].   The maximum flatness criterion yields inaccurate approximation of the transfer function in the low-frequency range [Kumar 1996], which is a critical drawback of the FIR filter for the displacement reconstruction in low-frequency dominant structures.   Moreover, as the order of the FIR filter is increased beyond a certain limit to improve the accuracy of the filter, the system matrix derived by the maximum flatness criterion tends to be singular.

3.1 FIR filter design and accuracy analysis

In this section, the displacement reconstruction defined with the BEF problem in the previous section is designed to become filters using one frequency-domain theory and two time-domain theories. These filters, which will be designed in this chapter, have a form of FIR filter consequently. The general performances of three FIR filters are verified with the transfer function and the accuracy function presented in the previous section.

3.1.1 Conventional FIR Filter

A conventional finite impulse response (CFIR) filter based on the BEF transfer function is designed in this section. A CFIR filter approximates a given transfer function in the frequency domain. Fig. 3-2 illustrates the basic setups for the formulation of the CFIR filter. In case accelerations are measured discretely by a uniform time increment, Δt, the CFIR filter expresses the displacement at the center of the time interval, u_{k+1}, as a linear combination (or a time convolution) of measured accelerations in a time window.

$$u_{k+1} = u(t) = (\Delta t)^2 \sum_{p=1}^{2k+1} c_p^c \overline{a}_p = (\Delta t)^2 \sum_{p=-k}^{k} c_{p+k+1}^c \overline{a}(t + p\Delta t) \tag{3-1}$$

where c_p^c is the coefficient of the CFIR filter. Here superscript 'c' implies 'conventional'.

$$t = T_1 + k\Delta t$$
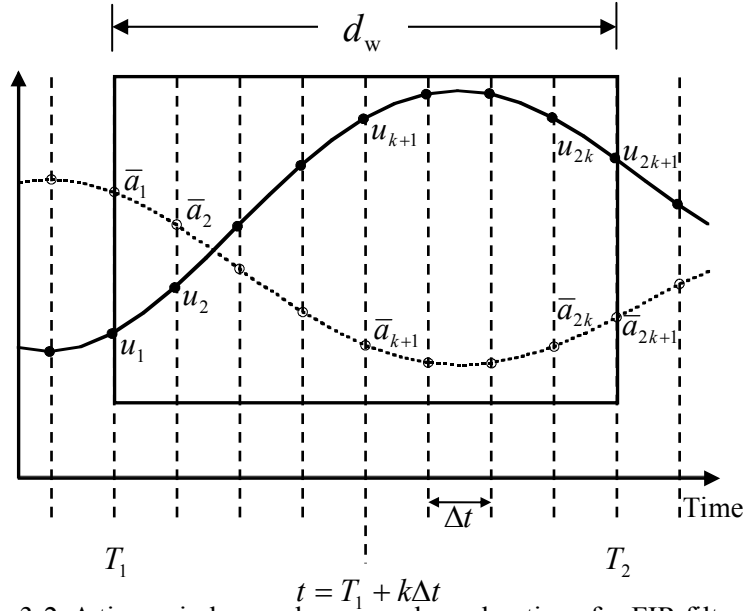
Figure 3-2. A time window and measured accelerations for FIR filters

The square of the time increment is introduced in Eq. (3-1) to make the coefficients of the CFIR filter dimensionless.

The size of the time window is referred to as the filter size in the digital filter field. Once the displacement is computed for time t, the time window moves forward by Δt to reconstruct the displacement at $t+\Delta t$. This procedure is identical to the overlapping time-window technique proposed by Park et al. [Park 2008] for the structural damage detection.

The Fourier transform of Eq. (3-1) yields the transfer function of the CFIR filter.

$$F(u(t)) = (\Delta t)^2 \sum_{p=-k}^{k} c_{p+k+1}^c F(\overline{a}(t + p\Delta t))$$

$$F(u(t)) = H_C(f)F(\overline{a}(t)) = (\Delta t)^2 \sum_{p=-k}^{k} c_{p+k+1}^c e^{i2\pi f p \Delta t} F(\overline{a}(t))$$

(3-2)

$$H_C(f) = (\Delta t)^2 \sum_{p=-k}^{k} c_{p+k+1}^c e^{i2\pi f p \Delta t}$$

(3-3)

where $H_C(f)$ is the transfer function of the CFIR filter, and i is the imaginary unit. The transfer function of the CFIR filter is supposed to approximate the BEF transfer function given in Eq. (2-16).

$$H_B(f) \approx (\Delta t)^2 \sum_{p=-k}^{k} c_{p+k+1}^c e^{i2\pi f p \Delta t}$$

(3-4)

Eq. (3-4) represents the truncated Fourier series of the BEF transfer function, and the coefficients of the CFIR filter are determined as following equation by the theory.

$$c_{p+k+1}^c = \frac{1}{(\Delta t)^2} \frac{1}{f_s} \int_{-f_s/2}^{f_s/2} H_B(f) e^{i2\pi f \Delta t p} df$$

$$= \frac{1}{\Delta t} \int_{-f_s/2}^{f_s/2} H_B(f) e^{i2\pi f \Delta t p} df$$

(3-5)

where $f_s = 1/\Delta t$ denotes the sampling frequency of measurement.

Since the BEF transfer function in Eq. (3-5), $H_B(f)$, is an even function, the imaginary term inside the integration is zero by Euler's identity and thus there is no

phase response in the CFIR filter.

$$
\begin{aligned}
c_{p+k+1}^{c} &= \frac{1}{\Delta t} \int_{-f_s/2}^{f_s/2} H_B(f) e^{i2\pi f \Delta t p} \, df \\
&= -\frac{1}{\Delta t} \frac{1}{(2\pi)^2} \int_{-f_s/2}^{f_s/2} \frac{f^2}{f^4 + \lambda^4 f_T^4} \cos(2\pi p f \Delta t) df \\
&= -\frac{1}{2\pi^2 \widetilde{f}_T} \int_{0}^{1/(2\widetilde{f}_T)} \frac{\widetilde{f}^2}{\widetilde{f}^4 + \lambda^4} \cos(2\pi p \widetilde{f}_T \widetilde{f}) d\widetilde{f}
\end{aligned}
\tag{3-6}
$$

where $\widetilde{f}_T = f_T / f_s$ denotes the target frequency to the sampling frequency (TSF)

ratio. The coefficient of the CFIR filter approximating the exact transfer function

cannot be evaluated like Eq. (3-6) due to the singularity at the zero frequency.

The coefficients in Eq. (3-6) are always real and symmetric with respect to

$p = 0$, since the BEF transfer function is an even function in the frequency do-

main. As the BEF transfer function decreases rapidly for larger $\widetilde{f}$ as shown in

Fig. 2-3, the integral in Eq. (3-6) is nearly independent of the upper limit for a

small TSF ratio of $\widetilde{f}_T \leq 0.1$, and thus becomes a function of $\widetilde{p} = p\widetilde{f}_T$. Conse-

quently, the relation between $\widetilde{c}_{p+k+1} = c_{p+k+1}\widetilde{f}_T$ and $\widetilde{p}$ is TSF-ratio independent

as shown in Fig. 3-3 (a). The trapezoidal rule is employed to evaluate the integral.

Although the number of terms included in the CFIR filter varies with filter sizes,

the coefficients for the same p are always identical for all filter sizes at a fixed TSF

ratio.
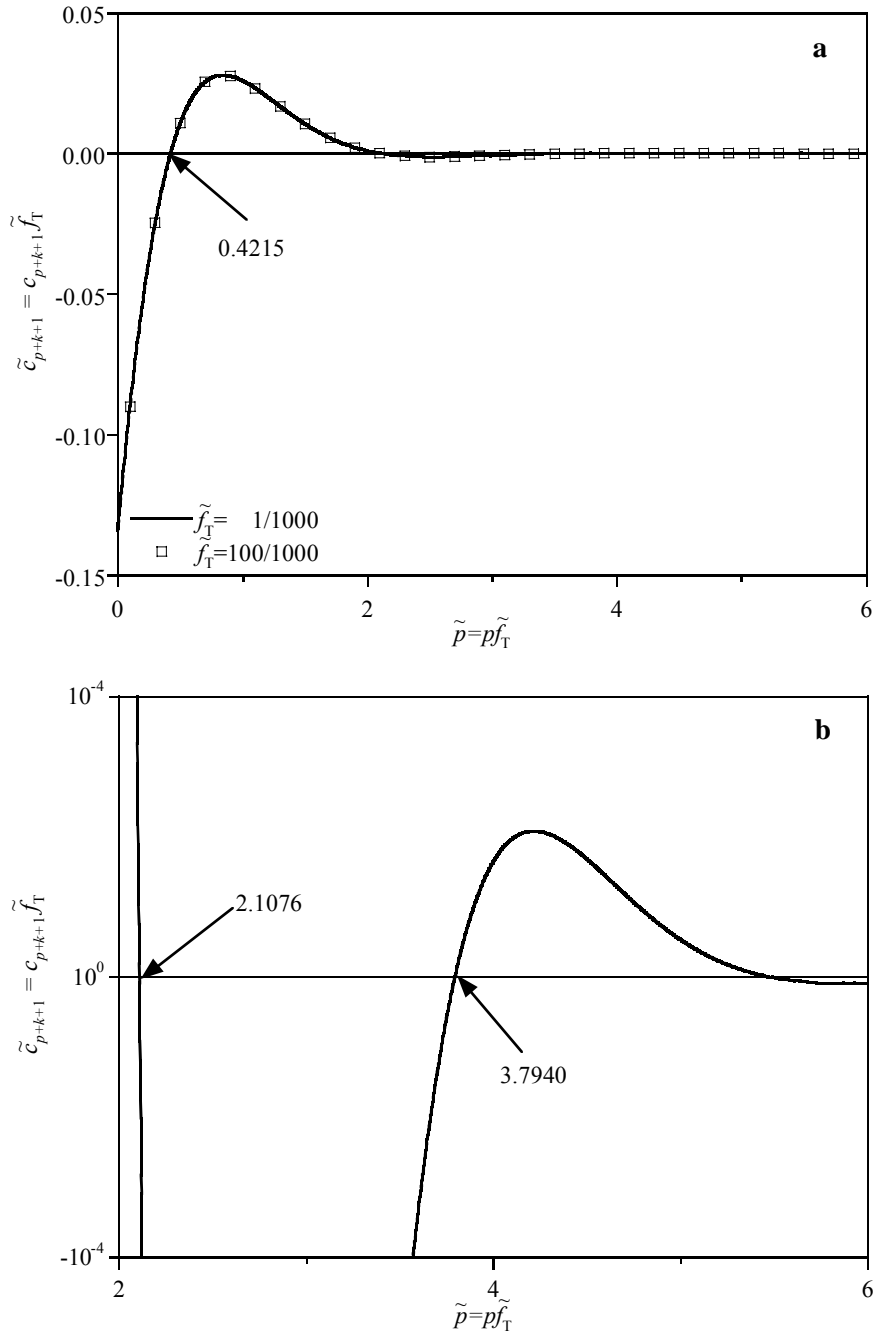
Figure 3-3. Coefficients of the CFIR filters for two different TSF ratios: (a) Small scale. (b) Detail in a large scale.

The Gibbs phenomenon, which is the rippling characteristics of a truncated Fourier series, occurs in the CFIR transfer function. To reduce the rippling amplitude, the filter size should be selected so that the coefficients smoothly converge to zero as p approaches to k [Rabiner 1975, Hamming 1989]. Therefore the last term of the CFIR filter should correspond to zero-crossing points, $\widetilde{p}_0$, in Fig. 3-3.

$$k\widetilde{f}_T = \widetilde{p}_0 \quad \text{or} \quad k = \frac{\widetilde{p}_0}{\widetilde{f}_T} \tag{3-7}$$

When the calculated value for k with Eq. (3-7) is not an integer, the closest integer to the calculated k is employed. The filter size is defined using k in Eq. (3-7)

$$d_w = 2k\Delta t = 2\frac{f_s}{f_T}\widetilde{p}_0\Delta t = \frac{2\widetilde{p}_0}{f_T} = N_w\frac{1}{f_T} \tag{3-8}$$

where d_w and $N_w = 2\widetilde{p}_0$ are the filter size expressed in terms of time and the target period, respectively. The target period denotes the reciprocal of the target frequency.

The zero-crossing points appear periodically from 0.421 by a constant interval of 1.687 such as 0.421, 2.108, 3.794, etc in Fig. 3-3. The filter sizes corresponding to the three zero crossing points become 0.842, 4.215 and 7.588 times the target period.

As the coefficient of the CFIR filter does not converge to zero near the first

zero-crossing point as shown in Fig. 3-3 (a), the filter size of $N_w = 0.842$ yields a large rippling amplitude in the transfer function (it will be illustrated in later in this chapter), and is not an adequate size. The filter sizes of $N_w = 4.215$ and 7.588 result in the acceptable rippling amplitudes in the transfer and accuracy functions, and therefore are selected as the standard filter size and the long filter size, respectively. The long filter size yields smaller rippling amplitude but requires more computational effort than the standard one. The selection of the filter size between the standard and long filter size depends on specific applications. Of course, a filter size longer than the long filter size may be utilized, but it is believed that the long filter size gives sufficiently accurate results in an engineering sense.

Because of the symmetry of the coefficients, the transfer function of the proposed CFIR filter has no phase differences and becomes as follows.

$$H_C(f) = (\Delta t)^2 (c_{k+1}^c + 2\sum_{p=1}^{k} c_{p+k+1}^c \cos(2\pi pf\Delta t)) \qquad (3\text{-}9)$$

The normalized transfer function and accuracy function of the CFIR filter are derived as following equations:

$$\tilde{H}_C(\tilde{f}) = -(2\pi\tilde{f}_T)^2 (c_{k+1}^c + 2\sum_{p=1}^{k} c_{p+k+1}^c \cos(2\pi p\tilde{f}_T\tilde{f})) \qquad (3\text{-}10)$$

$$H_C^{acc}(\tilde{f}) = -(2\pi\tilde{f}_T\tilde{f})^2 (c_{k+1}^c + 2\sum_{p=1}^{k} c_{p+k+1}^c \cos(2\pi p\tilde{f}_T\tilde{f})) \qquad (3\text{-}11)$$

where $\widetilde{H}_C$ and H_C^{acc} are the normalized transfer function and accuracy function of the CFIR filter, respectively.

The transfer functions of the CFIR filter are shown Fig. 3-4 for the standard and long filter sizes at the TSF ratio of 1/1000, while the transfer function for $N_w = 5$ is added to Fig 3-4 (a) to verify the rippling characteristic of the CFIR filter with other filter size. The CFIR filters for both standard and long filter sizes approximate the BEF transfer function very well for $\widetilde{f} \geq 1$.

As shown in Fig. 3-4 (a), the transfer function for $N_w = 5$ oscillates severely, and tends to diverge as the frequency increases. These severe oscillations in the transfer function are always observed for filter sizes other than the standard and long filter sizes. The smaller filter size except the two filter sizes not only causes the larger oscillation amplitude, but also triggers the oscillation at the smaller frequency. The transfer function of the CFIR filter with the standard filter size decreases faster than that with the long filter size for $\widetilde{f} \leq 0.1$, and becomes negative when $\widetilde{f} \leq 0.043$. The negative transfer function causes the phase error of π in the reconstructed displacement. Since, however, only noise components exist in the frequency range, the negative transfer function would not cause any phase error for physically meaningful displacement components.
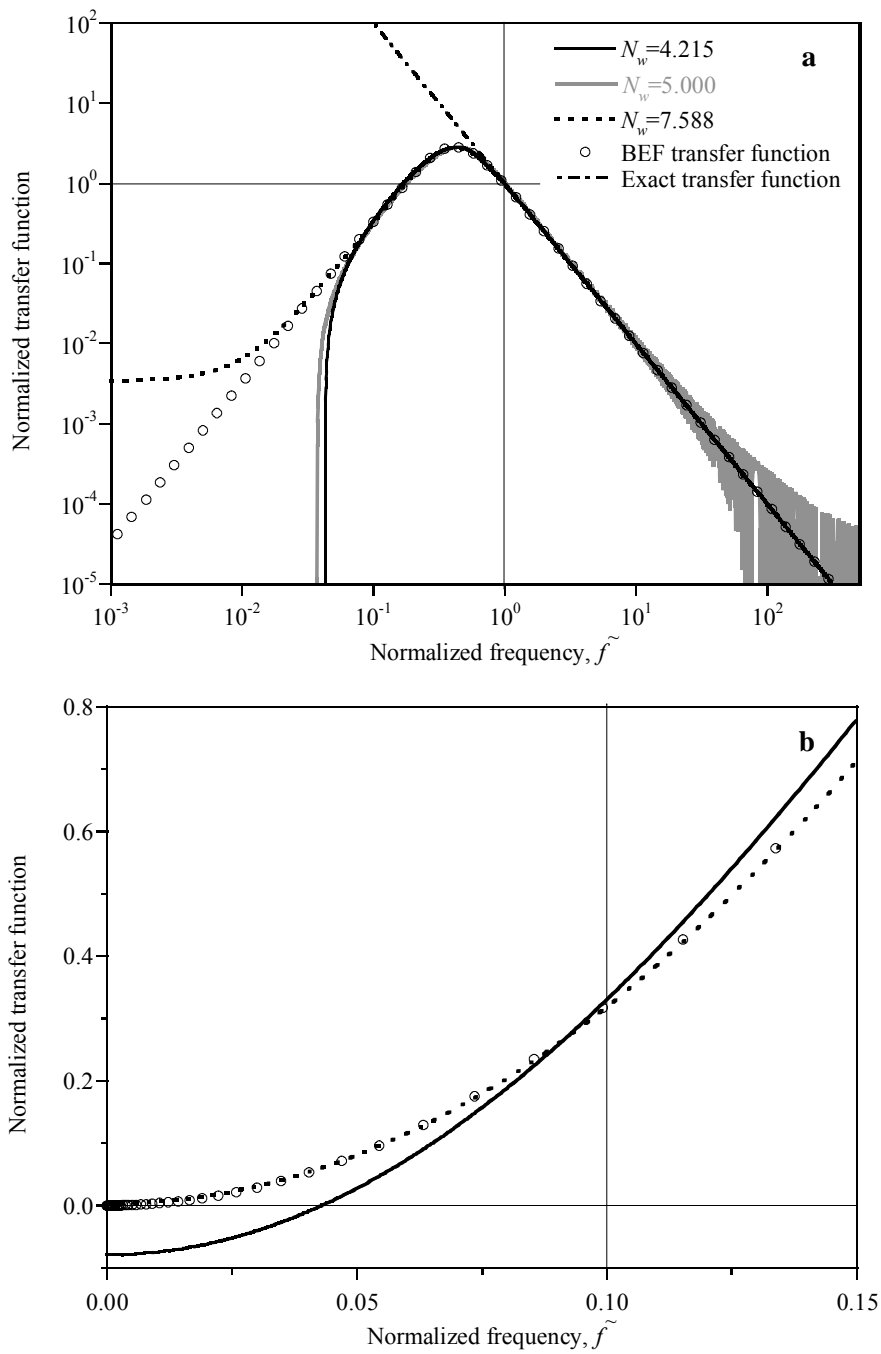
Figure 3-4. Transfer functions for the CFIR filters for various filter sizes: (a) Log-log scale. (b) Detail in a linear scale.
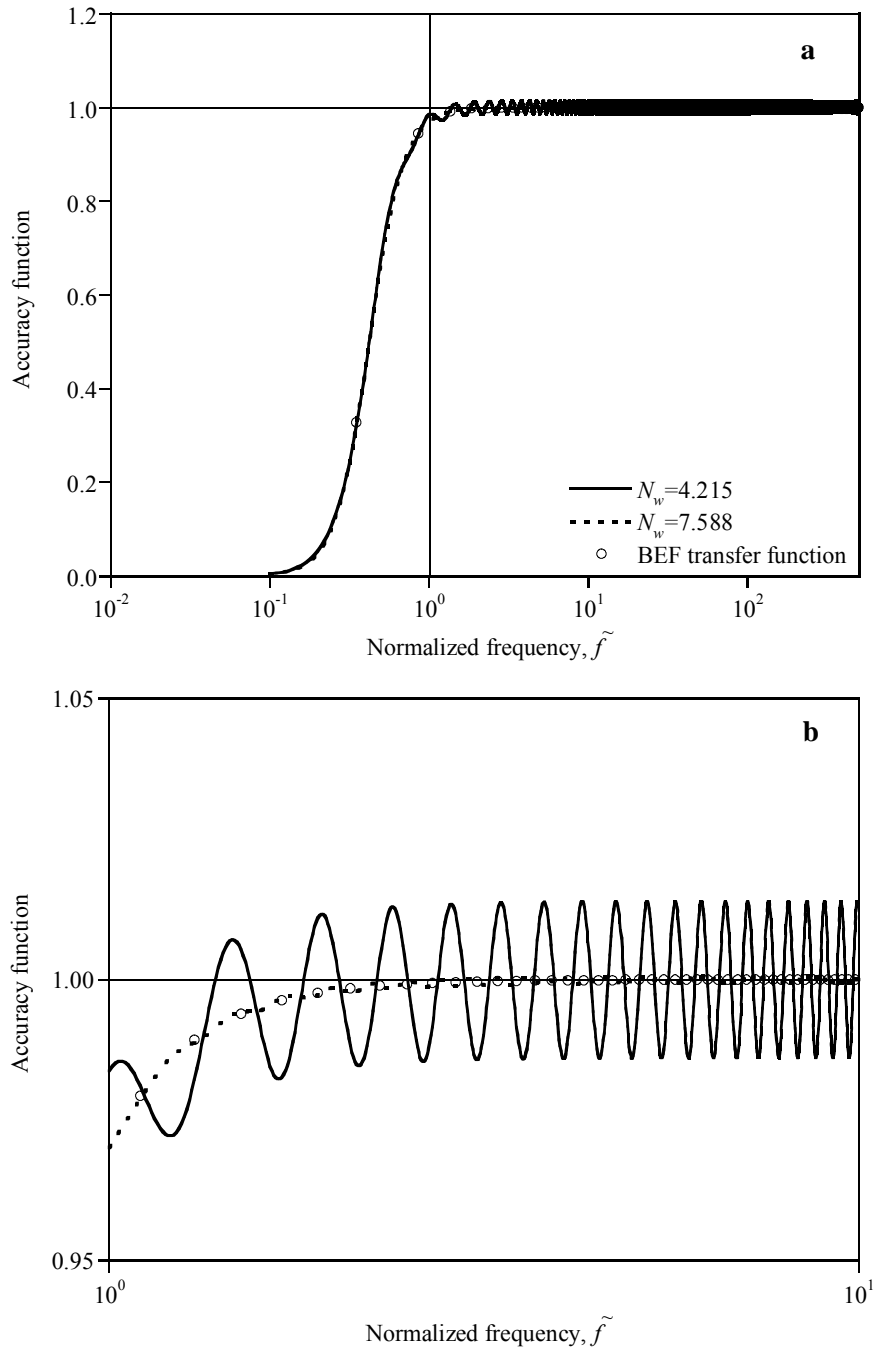
Figure 3-5. Accuracy functions of the CFIR filter for the standard and the long filter sizes: (a) Small scale. (b) Detail in a large scale.
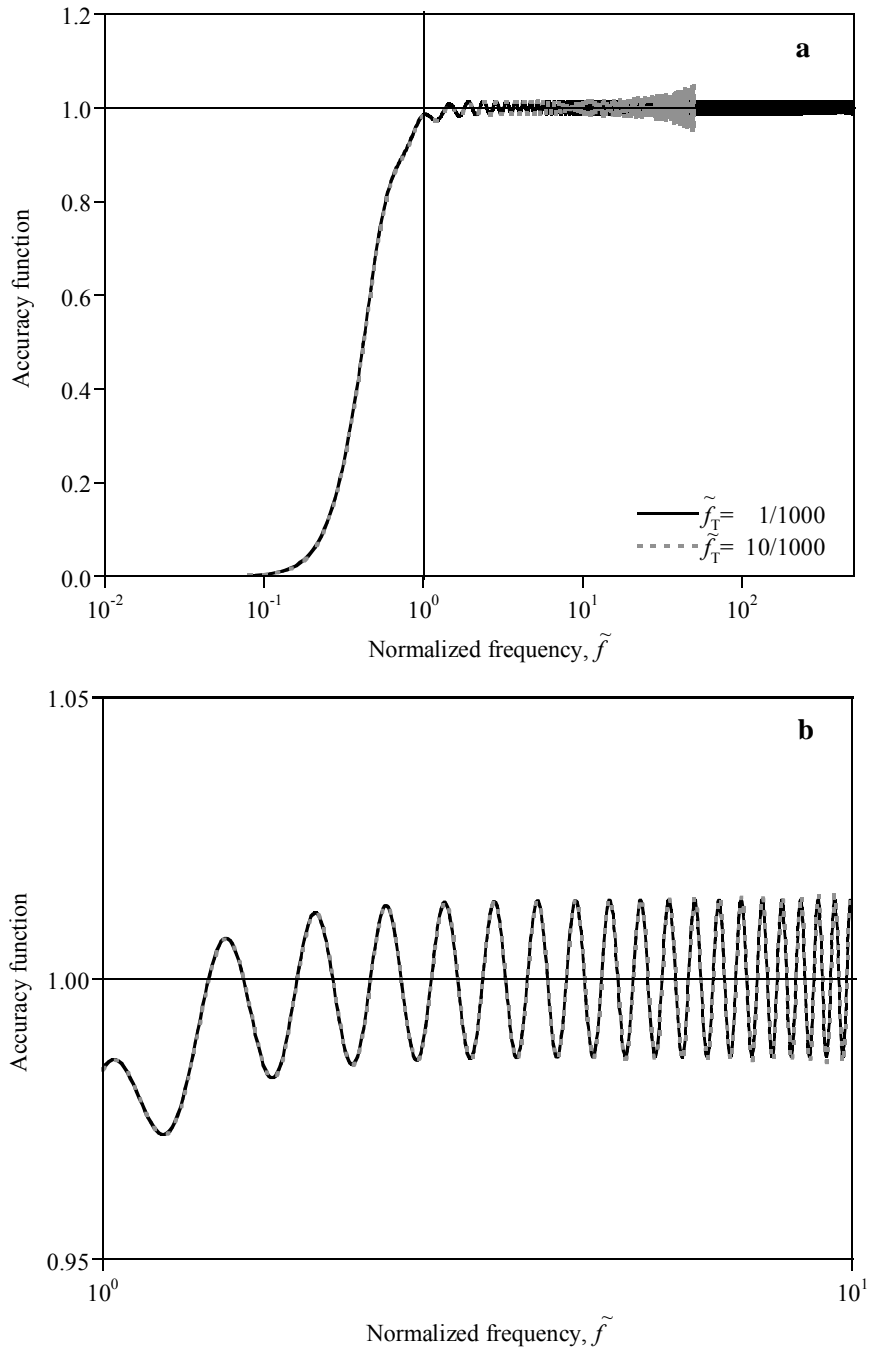
Figure 3-6. Accuracy functions of the CFIR filter for two different TSF ratios: (a) Small scale. (b) Detail in a large scale.

As shown in detailed graph with the linear scale in Fig. 3-4 (b), the transfer functions for the standard and long filter sizes converge to –0.079 and 0.004 at $\widetilde{f} = 0$, respectively.   This fact implies that the long filter size provides stronger noise suppression capability in the extremely low frequency range than the standard filter size to the CFIR filter.

The Gibbs phenomenon is clearly observed in the plot of the accuracy function in Fig. 3-5.   The rippling amplitudes for the standard and long filter sizes are 1.4% and 0.06%, respectively.   The rippling of the accuracy function is hardly noticeable for the long filter size even in the plot with a large scale in Fig. 3-5 (b).

The accuracy functions for the standard filter size at two different TSF ratios of 1/1000 and 10/1000 are presented in Fig. 3-6, and are almost identical up to the corresponding Nyquist frequencies.   The enlarged plot of the accuracy functions near the target frequency is also presented in Fig. 3-6 (b).   This figure verifies the TSF ratio independence of the transfer function.   The rippling amplitude of the accuracy function for the TSF ratio of 10/1000 increases slightly near the Nyquist frequency.   The accuracy at the target frequency is evaluated as 0.984 for the both TSF ratios.

The proposed CFIR filter exhibits uniform frequency responses from the target frequency to the Nyquist frequency, and is able to reconstruct displacement with the same level of accuracy independent of the TSF ratio for the frequency range.   Noise components below the target frequency are effectively suppressed in the CFIR filter.   The only restriction of the proposed CFIR filter is that the filter

size should be fixed at either the standard or long filter size, and cannot be adjusted freely as needed in actual applications.

3.1.2 FDM-FIR filter

The direct discretization of the minimization problem in Eq. (2-12) with the finite difference method leads to a new class of FIR filter, which is referred to as the FDM-FIR filter. The FDM-FIR filter is formulated purely in the time domain unlike FDIA and CFIR in previous chapter, and is able to reconstruct displacement history.
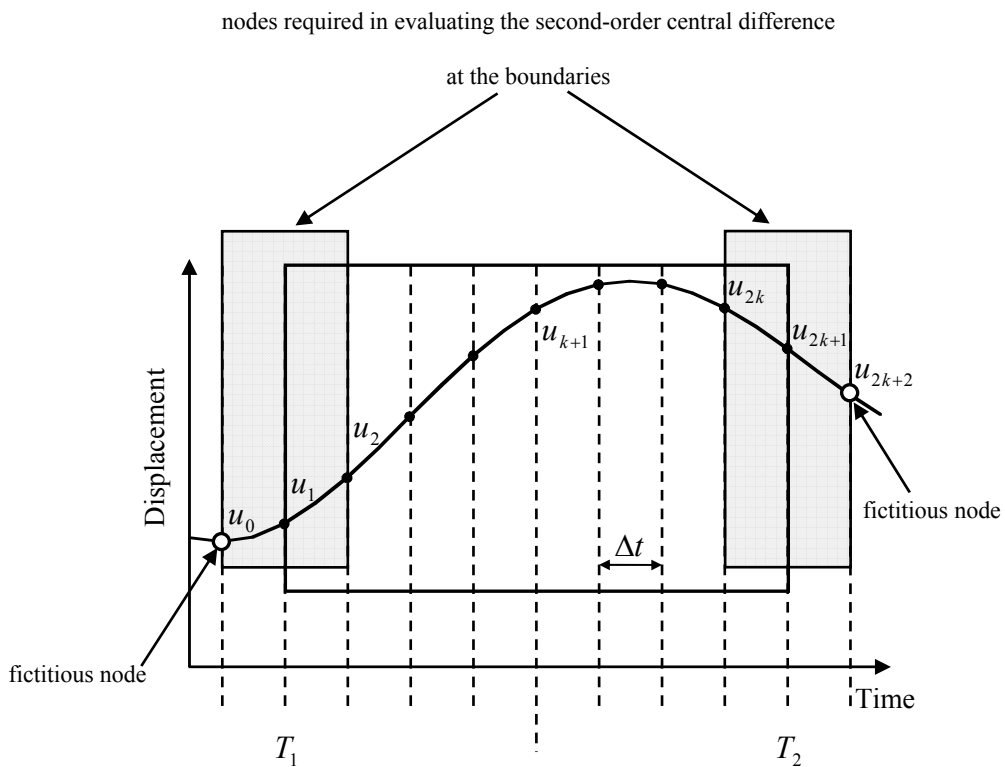
Figure 3-7. Definition of the displacements at discrete time steps and the fictitious nodes for FDM-FIR filter.

As the CFIR filter, the FDM-FIR filter reconstructs displacement using the moving time-window technique, the standard and long filter sizes defined for the CFIR filter in the previous section are adopted for the FDM-FIR filter.

The first term of Eq. (2-12), $\Pi_E(u)$, is discretized by the trapezoidal rule with an odd number of time step, $2k+1$, as shown in Fig. 3-7.

$$
\begin{aligned}
\Pi_E(u) &\approx \frac{1}{2}(\frac{1}{2}(a_1 - \overline{a}_1)^2 + (a_2 - \overline{a}_2)^2 + \cdots + (a_{2k} - \overline{a}_{2k})^2 + \frac{1}{2}(a_{2k+1} - \overline{a}_{2k+1})^2)\Delta t \\
&= \frac{1}{2}(\mathbf{a} - \overline{\mathbf{a}})^T(\mathbf{L}_a)^T \mathbf{L}_a(\mathbf{a} - \overline{\mathbf{a}})\Delta t = \frac{1}{2}\|\mathbf{L}_a(\mathbf{a} - \overline{\mathbf{a}})\|_2^2 \Delta t
\end{aligned}
\tag{3-12}
$$

where $2k+1$, a_p, $\overline{a}_p$ and $\|\cdot\|_2$ are the number of data points in period $T_1 \le t \le T_2$, the calculated acceleration, the measured acceleration at the p-th time step and the 2-norm of a vector, respectively, while the bold-faced variables denote the corresponding vectors. $\mathbf{L}_a$ is a diagonal weighting matrix of order $(2k+1)$ with all diagonal entries of 1 except the first and last entry, which are equal to $1/\sqrt{2}$. The calculated acceleration, a_p, is discretized by the central finite difference of Eq. (2-12), which is the proper approximation of the second-order boundary value problems [Lapidus 1982].

$$
\frac{u_{p+1} - 2u_p + u_{p-1}}{(\Delta t)^2} = a_p \quad \text{for} \quad p = 1, \cdots, 2k+1
\tag{3-13}
$$

where u_p is the displacement at the p-th time step as illustrated in Fig 3-7. Eq.

(3-13) is rewritten in a matrix form for all time steps.

$$\frac{1}{(\Delta t)^2} \mathbf{L}_c \mathbf{u} = \mathbf{a} \tag{3-14}$$

where $\mathbf{L}_c$ and $\mathbf{u}$ denote the linear algebraic operator matrix of order $(2k+1) \times (2k+3)$ and the vector of displacements at the discrete time steps, respectively, and are defined as follows.

$$\mathbf{L}_c = \begin{bmatrix} 1 & -2 & 1 & & & & \\ & 1 & -2 & 1 & & 0 & \\ & & & \ddots & & & \\ & 0 & & 1 & -2 & 1 & \\ & & & & 1 & -2 & 1 \end{bmatrix}, \quad \mathbf{u} = \begin{bmatrix} u_0 \\ u_1 \\ \vdots \\ u_{k+1} \\ \vdots \\ u_{2k+1} \\ u_{2k+2} \end{bmatrix} \tag{3-15}$$

Substitution of Eq. (3-14) into Eq. (3-12) leads to the following discretized minimization problem of Eq. (2-6).

$$\underset{\mathbf{u}}{\text{Min}}\, \Pi_E(\mathbf{u}) = \frac{1}{2} \left\| \mathbf{L}_a (\mathbf{a} - \bar{\mathbf{a}}) \right\|_2^2 \Delta t = \frac{1}{2} \frac{1}{\Delta t^4} \left\| \mathbf{L}\mathbf{u} - (\Delta t)^2 \mathbf{L}_a \bar{\mathbf{a}} \right\|_2^2 \Delta t \tag{3-16}$$

where $\mathbf{L} = \mathbf{L}_a \mathbf{L}_c$.

As discussed in Chapter 2, the minimization problem of Eq. (3-16) is unable to yield a unique displacement for given measured acceleration due to the rank-

deficiency in linear algebraic operator, $\mathbf{L}$. The rank-deficiency is caused by the fact that only $(2k+1)$ finite difference equations are defined in Eq. (3-13) for $(2k+3)$ unknown displacement. The two additional displacements at time step 0 and $(2k+2)$ outside the time window are included in Eq. (3-15) to define the second-order central finite difference at the two boundaries as illustrated in Fig. 3-7. The time steps denoted by 0 and $(2k+2)$ play the same role as fictitious nodes [Lapidus 1982], which are usually employed to solve partial differential equations by the finite difference method. Should two boundary conditions be supplied to Eq. (3-16) as in well-posed boundary value problems, two additional equations are defined with boundary conditions, and the sufficient rank of $(2k+3)$ is provided to solve the minimization problem given in Eq. (3-16).

Because of the fictitious nodes, the domain of regularization function should be extended to contain this outside displacement at the time steps 0 and $(2k+2)$. Hence the original minimization problem should be changed by following equation.

$$\underset{u}{\text{Min}}\,\Pi(u) = \Pi_E(u) + \Pi_R(u) = \frac{1}{2}\int_{T_1}^{T_2}(\frac{d^2u}{dt^2} - \bar{a})^2\,dt + \frac{\beta^2}{2}\int_{T_1-\Delta t}^{T_2+\Delta t} u^2\,dt \qquad (3\text{-}17)$$

By this extension of domain, the second term of Eq. (3-17), $\Pi_R(u)$, is discretized by the same procedure used in Eq. (3-12) with trapezoidal rule.

$$\Pi_R(u) \approx \frac{\beta^2}{2}(\frac{1}{2}u_0{}^2 + u_1{}^2 + \cdots + u_{2k+1}{}^2 + \frac{1}{2}u_{2k+2}{}^2)\Delta t$$

$$= \frac{\beta^2}{2}\mathbf{u}^T\mathbf{L}_u{}^T\mathbf{L}_u\mathbf{u}\Delta t = \frac{\beta^2}{2}\|\mathbf{L}_u\mathbf{u}\|_2^2\Delta t \qquad (3\text{-}18)$$

where $\mathbf{L}_u$ is a diagonal weighting matrix of order ($2k$+3) with all diagonal entries of 1 except the first and last entry, which are equal to $1/\sqrt{2}$.

Substitution of Eq. (3-16) and (3-18) into Eq. (3-17) leads to the following discretized minimization problem,

$$\underset{u}{\text{Min}}\,\Pi(u) = \Pi_E(u) + \Pi_R(u)$$

$$\approx \frac{1}{2}\frac{1}{\Delta t^4}\left\|\mathbf{L}\mathbf{u} - (\Delta t)^2\mathbf{L}_a\bar{\mathbf{a}}\right\|_2^2 + \frac{\beta^2}{2}\left\|\mathbf{L}_u\mathbf{u}\right\|_2^2 \qquad (3\text{-}19)$$

As the time increment is considered to be a constant in this study, the term on the time increment that appears outside the 2-norm has no effect on the solution of the minimization problem, and thus is omitted from the objective function in Eq. (3-19).

The minimization problem in Eq. (3-19) forms a quadratic problem with respect to the unknown displacement vector, and thus the solution of Eq. (3-19) is given analytically as

$$\mathbf{u} = \left(\mathbf{L}^T\mathbf{L} + \beta^2(\Delta t)^4\mathbf{I}_u\right)^{-1}\mathbf{L}^T\mathbf{L}_a\bar{\mathbf{a}}(\Delta t)^2 = \mathbf{C}^D\bar{\mathbf{a}}(\Delta t)^2 \qquad (3\text{-}20)$$

where $\mathbf{I}_u = \mathbf{L}_u{}^T\mathbf{L}_u$ is the near identity matrix of order $(2k+3)$ with all diago-

nal entries of 1 except the first and last entry, which are equal to $1/2$, and $\mathbf{C}^D$ is the coefficient matrix for the displacement reconstruction of order $(2k+3) \times (2k+1)$. Here superscript 'D' denotes the FDM-FIR filter.

The displacement at the center of a time window is the $(k+2)$-th component of $\mathbf{u}$ vector, u_{k+1}, in Eq. (3-15). Without the loss of generality, u_{k+1} of a time window is considered as the reconstructed displacement at time t.

$$u(t) = u_{k+1} = \mathbf{c}^D \overline{\mathbf{a}}(\Delta t)^2 = (\Delta t)^2 \sum_{p=1}^{2k+1} C_{k+2,p}^D \overline{a}_p$$
$$= (\Delta t)^2 \sum_{p=1}^{2k+1} c_p^D \overline{a}(t + (p - (k+1))\Delta t) = (\Delta t)^2 \sum_{p=-k}^{k} c_{p+k+1}^D \overline{a}(t + p\Delta t)$$

(3-21)

where $\mathbf{c}^D$ denotes the $(k+2)$-th row vector or the center row of the $\mathbf{C}^D$ matrix. The displacement reconstruction scheme defined in Eq. (3-21) represents an FIR filter that requires no initial condition.

The FDM-FIR filter of Eq. (3-21) is formulated completely in the time-domain rather than the frequency-domain. The transfer function and the trans-formations of measured accelerations to and/or from the frequency domain, which are required in the CFIR and FDIA, are not included at all in the whole reconstruction procedure of the proposed method.

The FDM-FIR in Eq. (3-21) have the identical expression with the CFIR filter in Eq. (3-1) except for the coefficient array. Hence, the only difference between the two filters is the method for determining the coefficients. The transfer func-

tion and accuracy function of the FDM-FIR filter in Eq. (3-21) are derived and normalized with the same method used in the CFIR filter as following equations.

$$\widetilde{H}_D(\widetilde{f}) = -(2\pi\widetilde{f}_T)^2 \left(c_{k+1}^D + 2\sum_{p=1}^{k} c_{k+1+p}^D \cos(2\pi p\widetilde{f}_T\widetilde{f})\right) \qquad (3\text{-}22)$$

$$H_D^{acc}(\widetilde{f}) = -(2\pi\widetilde{f}_T\widetilde{f})^2 \left(c_{k+1}^D + 2\sum_{p=1}^{k} c_{k+1+p}^D \cos(2\pi p\widetilde{f}_T\widetilde{f})\right) \qquad (3\text{-}23)$$

where $\widetilde{H}_D$ and H_D^{acc} are the normalized transfer function and accuracy function of the FDM-FIR filter, respectively.

The coefficients of the FDM-FIR filter, c_{p+k+1}^D, for various window sizes are plotted against p/k for the TSF ratio of 1/1000 in Fig. 3-8 together with those of the CFIR filter with the standard and long filter size.   The coefficients are symmetric with respect to $p=0$ and converge smoothly to zero regardless of filter sizes dissimilar to the CFIR filter.   Therefore, as far as the rippling amplitude in the transfer function is concerned, the filter size can be selected freely as needed in specific problems.   The convergence to zero becomes smoother for a longer filter size than other smaller filter size, which yields the smaller rippling amplitude [Rabiner 1975 and Hamming 1989].

The imaginary parts of the displacement transfer function vanish due to the s1ymmetry of the coefficients, and thus no phase error occurs in the reconstructed displacement with the FDM-FIR filter like the CFIR filter.   The coefficients of the

FDM-FIR and the CFIR filter appear to be almost identical in the figure, and the differences in the coefficients between the two filters seem negligible.   However, the differences cause considerable effect on behaviors of the two filters.

The transfer functions of the FDM-FIR filters with various filter sizes for the TSF ratio of 1/1000 are presented in Fig. 3-9.   The transfer functions appear almost identical above the target frequency regardless of the filter size in the figure, but the longer filter size the better approximation result of the BEF transfer function in the frequency region under target frequency.   The transfer function of the FDM-FIR filter approximates the BEF transfer function better than that of the CFIR filter shown in Fig. 3-4 below the target frequency for the same filter size. The severe oscillations in the transfer function of the CFIR filter found for $N_w = 5$ do not occur in the FDM-FIR at all.   The Gibbs phenomenon is clearly seen in the accuracy functions plotted for various filter sizes in Fig. 3-10 (a), and more precisely in Fig. 3-10 (b).
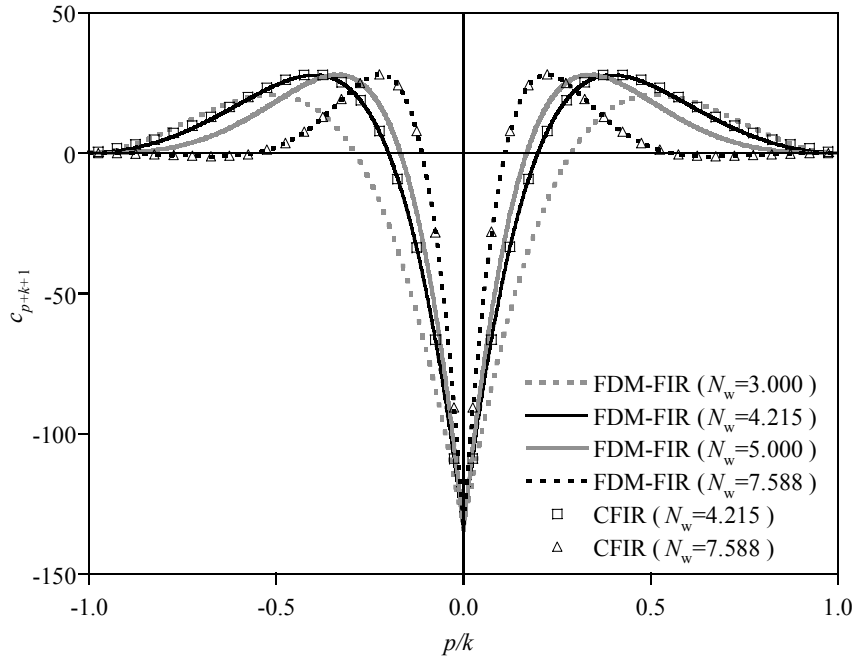
Figure 3-8. Coefficients of the FDM-FIR filter for various filter sizes
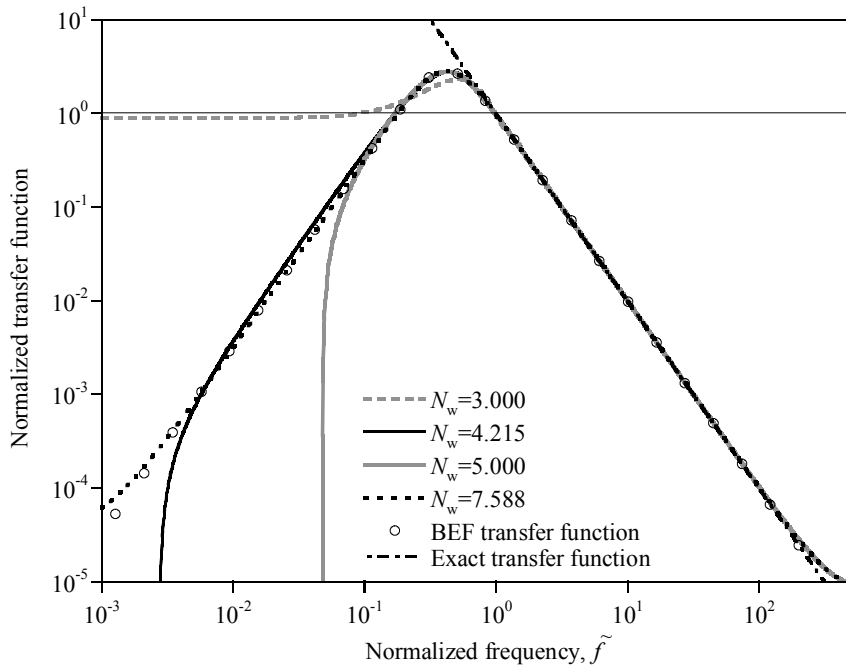
Figure 3-9. Transfer functions of the FDM-FIR filter for various filter sizes
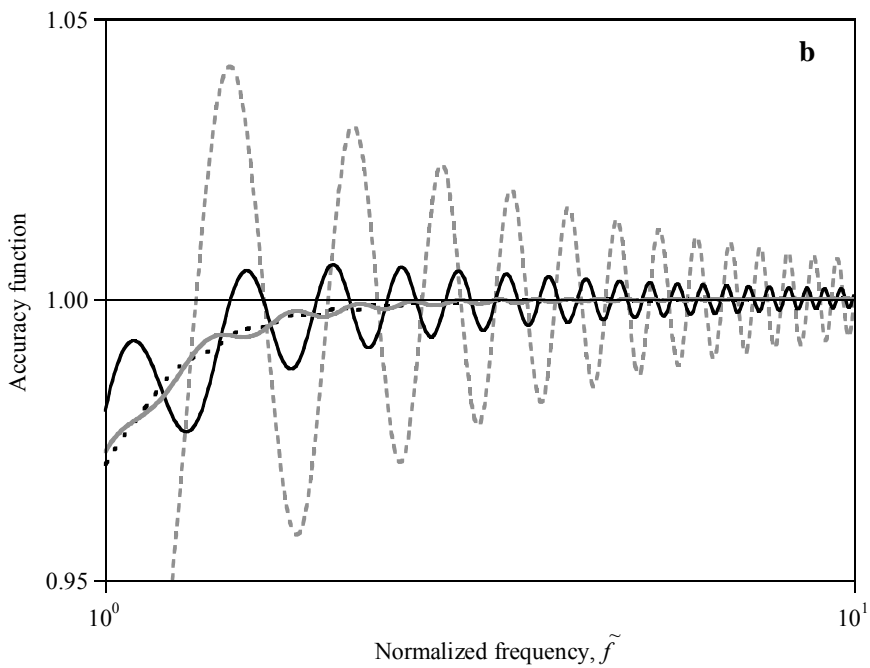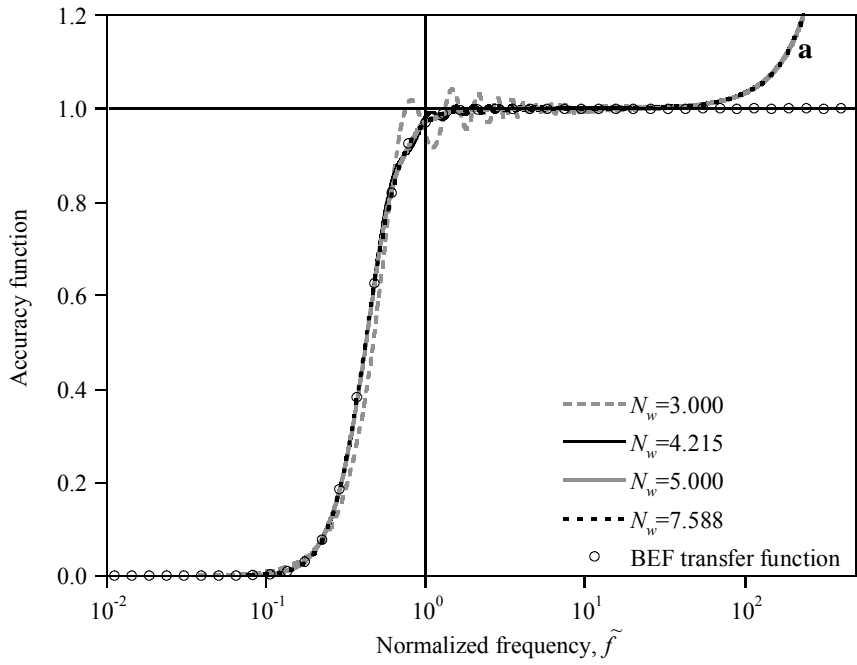
Figure 3-10. Accuracy functions of the FDM-FIR filter for various filter sizes: (a) Small scale. (b) Detail in a large scale

56
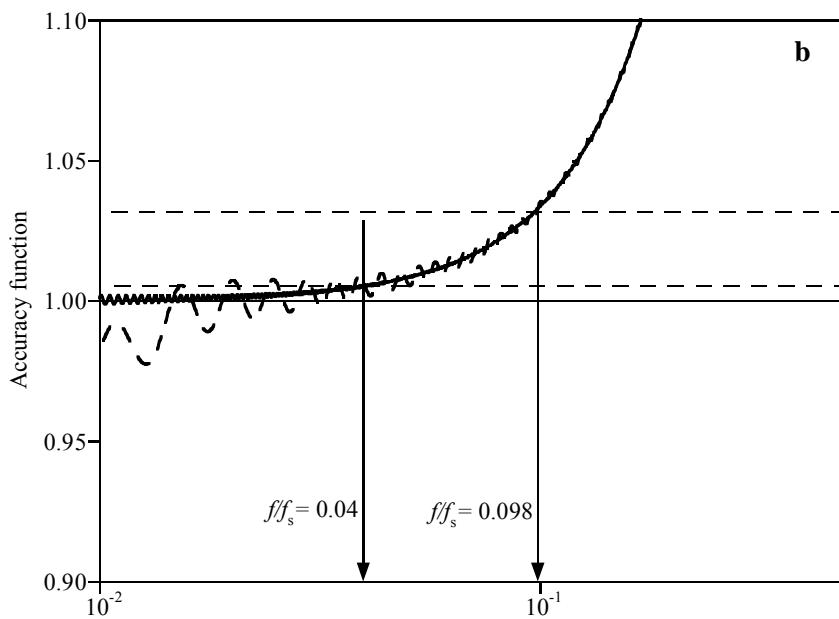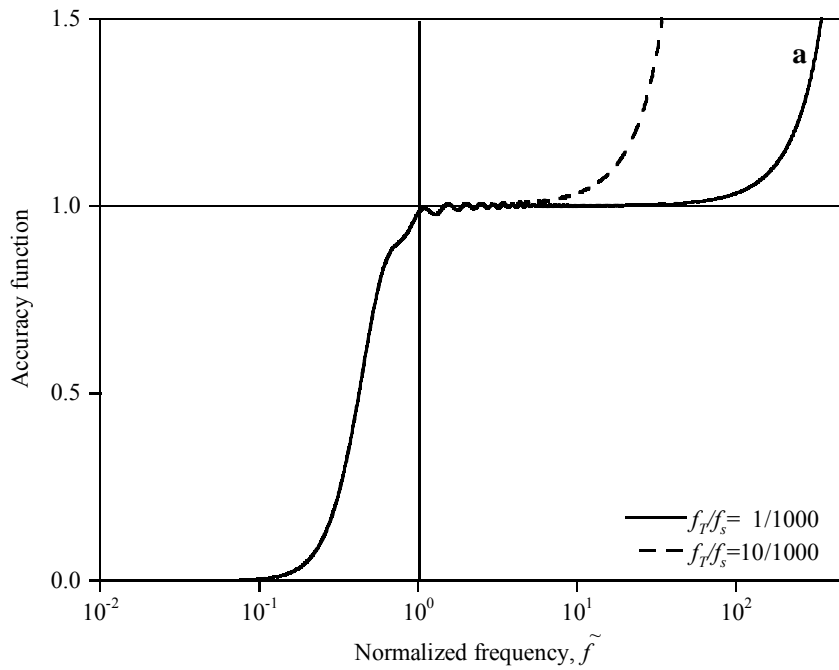
Figure 3-11. Accuracy functions of the FDM-FIR filter with the standard filter size
for two different TSF ratios: (a) Against the normalized frequency. (b) Against the
frequency normalized to the sampling frequency.

The larger filter size yields the smaller rippling amplitude of the accuracy function, and virtually no rippling in the accuracy function is observed for filter sizes larger than $N_w = 5$ as shown in Fig. 3-10 (b).

Unlike the CFIR filter, the rippling amplitude damps out quickly for all filter sizes as the frequency increases. The accuracy at the target frequency varies slightly with the filter size, which is caused by the rippling of the accuracy function. The standard and long filter sizes yield an accuracy of 0.98 and 0.97 at the target frequency, respectively.

Fig. 3-11 (a) presents the accuracy functions of the FDM-FIR filters with the standard filter size for two different TSF ratios of 1/1000 and 10/1000. In Fig. 3-11 (b), the accuracy functions plotted against the frequency normalized to the sampling frequency are also presented. The FDM-FIR filter yields identical accuracy functions independent of the TSF ratios near the target frequency as shown in Fig. 3-11 (a). Fig. 3-11 (b) reveals that the accuracy functions begin to deviate from the exact value 1 at 4% of the sampling rate, and become greater than 1.03, which means 3% amplitude amplification, after 12 % of the sampling rate regardless of TSF ratios. The FDM-FIR filter yields less accurate transfer functions for high frequencies over $0.1 f_s$ than for frequencies near the target frequency. Nevertheless, overall accuracy of the reconstructed displacement would not deteriorate much due to the aforementioned inaccuracy because the transfer function decreases rapidly in proportion to $1/\tilde{f}^2$, and the contribution of high frequency contents in

measured acceleration to the reconstructed displacement becomes negligible. To ensure the accuracy of the reconstructed displacement, all dominant frequencies in measured accelerations should be smaller than $0.1 f_s$. The frequency range to achieve the accuracy level of 0.97, which means 3% error in amplitude, is given as $f_T \leq f \leq 0.1 f_s$.

3.1.3 FEM-FIR filter

The discretization of the variation statement in Eq. (2-14) with the finite element method yields a FIR filter, which is referred to as the FEM-FIR filter (FFIR filter). Like the FDM-FIR filter in section 3.1.2, the FFIR filter is also formulated purely in the time domain for the purpose of the displacement reconstruction; it is able to reconstruct velocity as well as displacement at the same time. The FDM-FIR filter proposed in the previous section can successively reconstruct displacement history from measured acceleration, but the reconstruction of velocity is not considered.

The FFIR filter reconstructs displacement and velocity using the moving time-window technique as like other FIR filters in previous chapter. Even though the FFIR filter has no limitation about the filter size similar with the FDM-FIR filter, the standard and long filter sizes defined for the CFIR filter are also adopted for the FFIR filter for proper comparisons. Eq. (2-14) is discretized in time with $2k$ elements representing the time increments.

59

a) time coordinate   b) natural coordinate
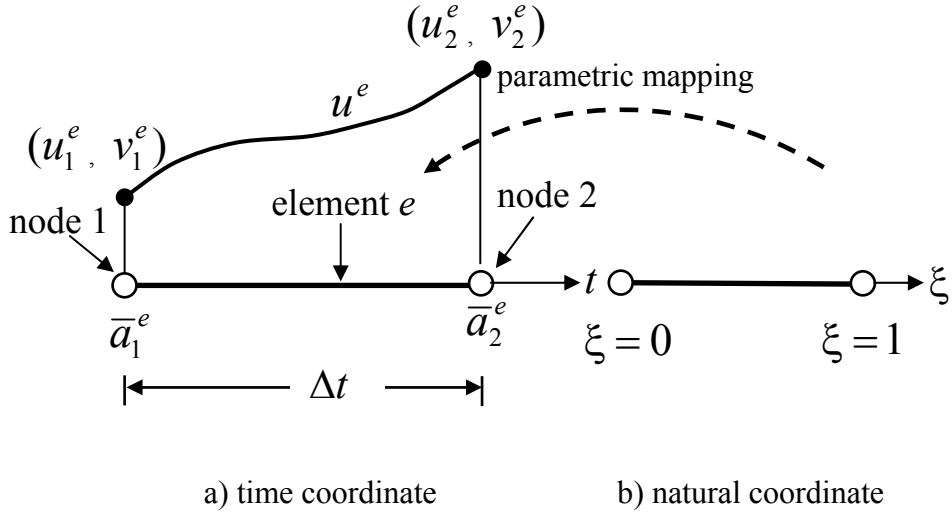
Figure 3-12. Finite element model for the FFIR filter

$$\delta\Pi(u) = \sum_{e=1}^{2k} \int_{\Delta t} \frac{d^2\delta u^e}{dt^2} \left(\frac{d^2 u^e}{dt^2} - \bar{a}^e\right) dt + \beta^2 \sum_{e=1}^{2k} \int_{\Delta t} \delta u^e u^e dt = 0 \qquad (3\text{-}24)$$

Here, u^e and $\bar{a}^e$ denote the displacement and acceleration in element, e, respectively. The displacement is interpolated with the Hermitian shape function, $\mathbf{N}_H$, and the measured acceleration is interpolated with the linear shape function, $\mathbf{N}_L$, in an element [Hughes 1987].

$$u^e = \mathbf{N}_H \cdot \mathbf{u}^e, \quad \bar{a}^e = \mathbf{N}_L \cdot \bar{\mathbf{a}}^e \qquad (3\text{-}25)$$

where $\mathbf{u}^e$ and $\bar{\mathbf{a}}^e$ are the nodal unknown vector and measured nodal acceleration in element e, respectively, and are defined as follows.

$$\mathbf{u}^e = (u_1^e, v_1^e, u_2^e, v_2^e)^T, \quad \overline{\mathbf{a}}^e = (\overline{a}_1^e, \overline{a}_2^e)^T \tag{3-26}$$

where $(\cdot)_1^e$ and $(\cdot)_2^e$ indicate nodal unknowns at the left and the right node of element e, respectively, and v is the velocity.   The definitions of the nodal variables are illustrated in Fig. 3-12.   Notice that the measured acceleration may be modeled as a constant in an element by averaging the two nodal accelerations if necessary.

The standard FEM formulation for a beam on an elastic foundation [Hetenyi 1946] is adopted to derive the following matrix expression of Eq. (3-24).

$$(\mathbf{K} + \beta^2 (\Delta t)^4 \mathbf{M})\mathbf{u} = (\Delta t)^2 \mathbf{Q}\overline{\mathbf{a}} \tag{3-27}$$

where $\mathbf{u}$ and $\overline{\mathbf{a}}$ denote the nodal unknown vector and the measured acceleration vector associated with all sampling points of measurement.   The nodal unknown vector consists of the nodal displacements and the nodal velocities.   The matrixes in Eq. (3-27) are defined as

$$\mathbf{K} = \sum_e \int_0^1 \frac{d^2 \mathbf{N}_H^T}{d\xi^2} \frac{d^2 \mathbf{N}_H}{d\xi^2} d\xi, \mathbf{M} = \sum_e \int_0^1 \mathbf{N}_H^T \mathbf{N}_H d\xi, \mathbf{Q} = \sum_e \int_0^1 \frac{d^2 \mathbf{N}_H^T}{d\xi^2} \mathbf{N}_L d\xi \tag{3-28}$$

where $\sum_e$ is the assembly operator of the FEM, and ξ is the natural coordinate [Hughes 1987] for the time variable ranging from 0 to 1.   The nodal unknown vector is obtained by solving Eq. (3-28).

$$\mathbf{u} = (\Delta t)^2 (\mathbf{K} + \beta^2 (\Delta t)^4 \mathbf{M})^{-1} \mathbf{Q}\overline{\mathbf{a}} = (\Delta t)^2 \mathbf{C}^F \overline{\mathbf{a}} \qquad (3\text{-}29)$$

where $\mathbf{C}^F$ is the coefficient matrix of order $2(2k+1) \times (2k+1)$. Here, super-script 'F' denotes the FFIR-filter.

Since the Neumann type boundary conditions are enforced in a weak sense for Eq. (3-24), the reconstructed variables are inevitably affected by errors in the boundary conditions. However, the errors rapidly decrease inside of the domain away from the boundary due to the diffusive characteristics of the FEM for elliptic boundary value problems. The displacement and velocity at the center of a time window are least affected by the errors induced by the weak enforcement of the boundary conditions, and are taken as the reconstructed solution in a time window. Assuming the time step at the center of a time window represents time t as in the CFIR and FDM-filter, the reconstructed displacement is expressed as

$$u(t) = u_{k+1} = \mathbf{c}^F \overline{\mathbf{a}} (\Delta t)^2 = (\Delta t)^2 \sum_{p=1}^{2k+1} C_{2k+1,p}^F \overline{a}_p$$

$$= (\Delta t)^2 \sum_{p=-k}^{k} c_{p+k+1}^F \overline{a}(t + p\Delta t) \qquad (3\text{-}30)$$

where $\mathbf{c}^F$ denotes the $(2k+1)$-th row of the $\mathbf{C}^F$ matrix. As shown in Eq. (3-30), not only FDM-FIR filter and CFIR filter but also FFIR filter has the identical expression. The transfer function and accuracy function of the FFIR filter in Eq. (3-30) are derived and normalized with the same method used in the CFIR filter as

following equations.

$$\widetilde{H}_F(\widetilde{f}) = -(2\pi\widetilde{f}_T)^2 (c_{k+1}^F + 2\sum_{p=1}^{k} c_{k+1+p}^F \cos(2\pi p \widetilde{f}_T \widetilde{f})) \tag{3-31}$$

$$H_F^{acc}(\widetilde{f}) = -(2\pi\widetilde{f}_T\widetilde{f})^2 (c_{k+1}^F + 2\sum_{p=1}^{k} c_{k+1+p}^F \cos(2\pi p \widetilde{f}_T \widetilde{f})) \tag{3-32}$$

where $\widetilde{H}_F$ and H_F^{acc} are the normalized transfer function and accuracy function of the FFIR filter, respectively.

Since the coefficients of the FFIR filter and the transfer function and accuracy function of it are nearly identical to the results of FDM-FIR filter, the detailed discussion is omitted and substituted by the Fig. 3-13~3-16. The frequency range to achieve the accuracy level of 0.97 is given as $f_T \leq f \leq 0.1 f_s$ by Fig 3-16 (b).

The velocity at the center of a time window is reconstructed using the (2*k*+2)-th row of the coefficient matrix in Eq. (3-30).

$$v(t) = v_{k+1} = (\Delta t)^2 \sum_{p=1}^{2k+1} C_{2k+2,p}^F \overline{a}_p = \Delta t \sum_{p=-k}^{k} \hat{c}_{p+k+1}^F \overline{a}(t + p\Delta t) = \hat{\mathbf{c}}^F \overline{\mathbf{a}} \Delta t \tag{3-33}$$

where $\hat{c}_{p+k+1}^F = \Delta t C_{2k+2,p+k+1}^F$. The coefficients for the velocity reconstruction are shown in Fig. 3-17 for various filter sizes at the TSF ratio of 1/1000, and always maintain anti-symmetry with respect to $p = 0$. The anti-symmetry of the coefficients is also held for different TSF ratios because the compositions of the system matrices in Eq. (3-28) are independent of the TSF ratios.
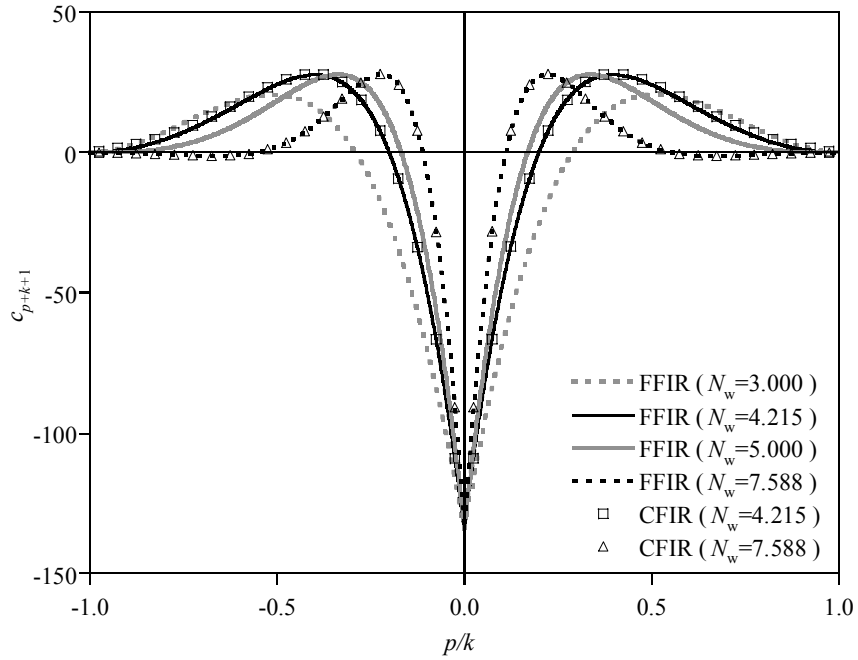
Figure 3-13. Coefficients of the FFIR filter for various filter sizes
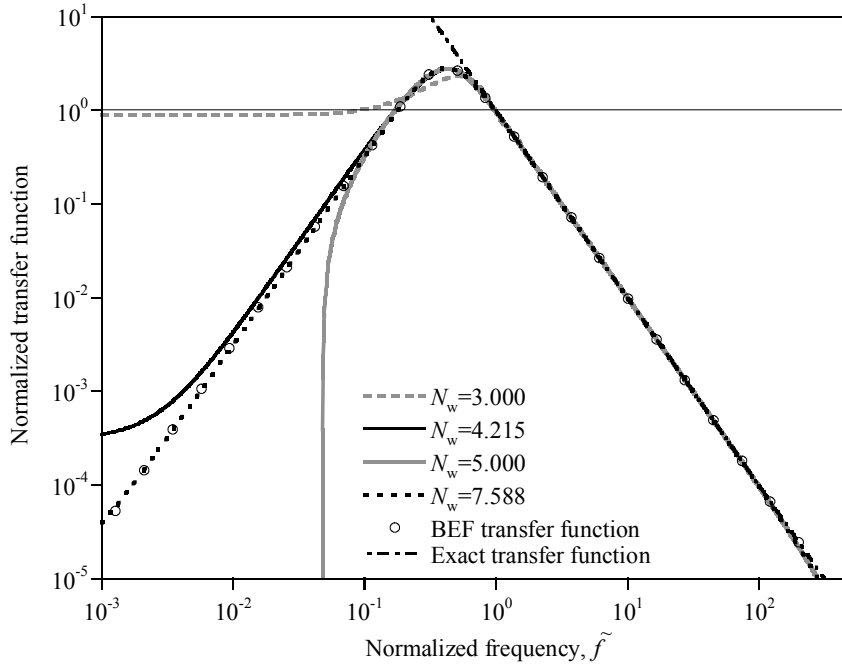
Figure 3-14. Transfer functions of the FFIR filter for various filter sizes
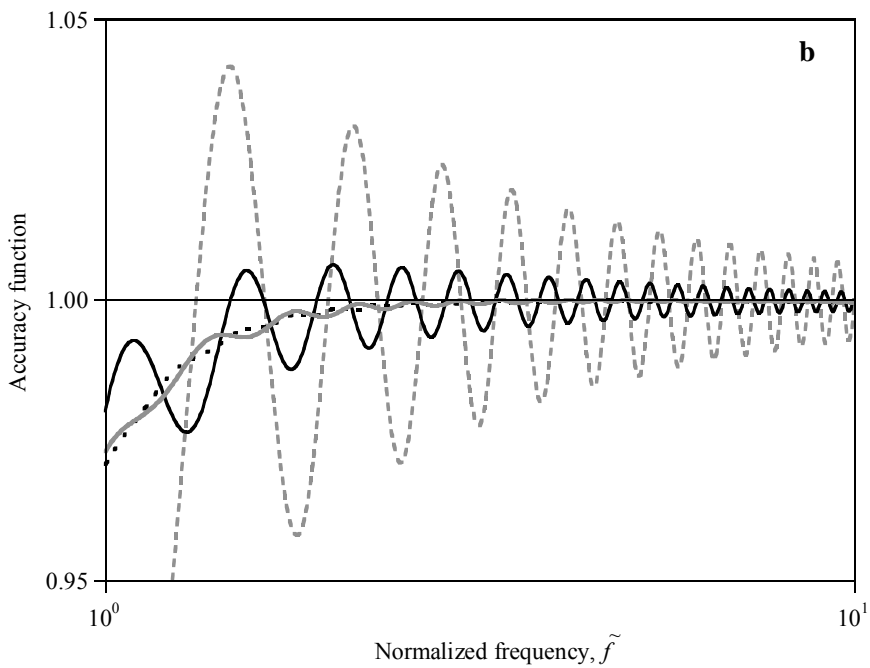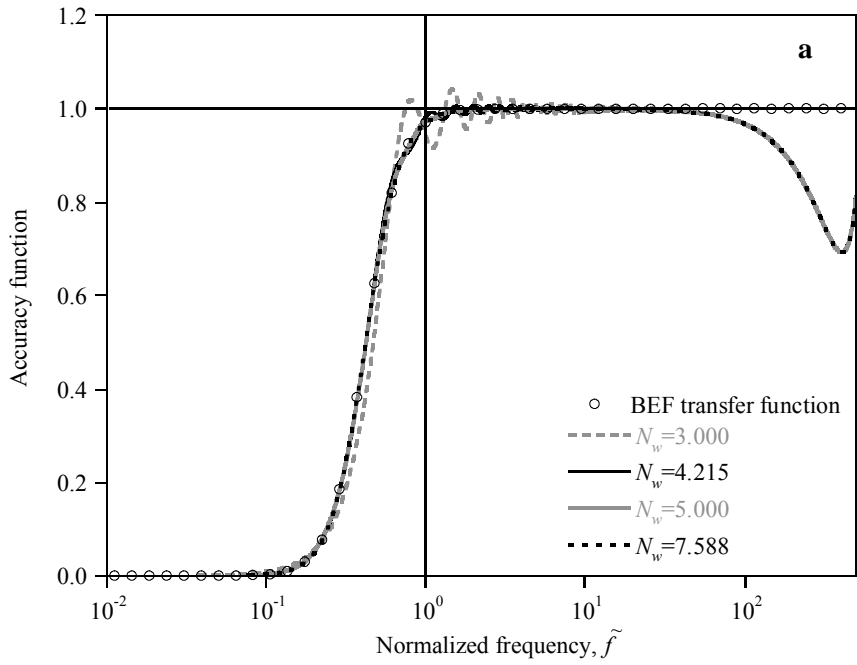
Figure 3-15. Accuracy functions of the FFIR filter for various filter sizes: (a) Small scale. (b) Detail in a large scale
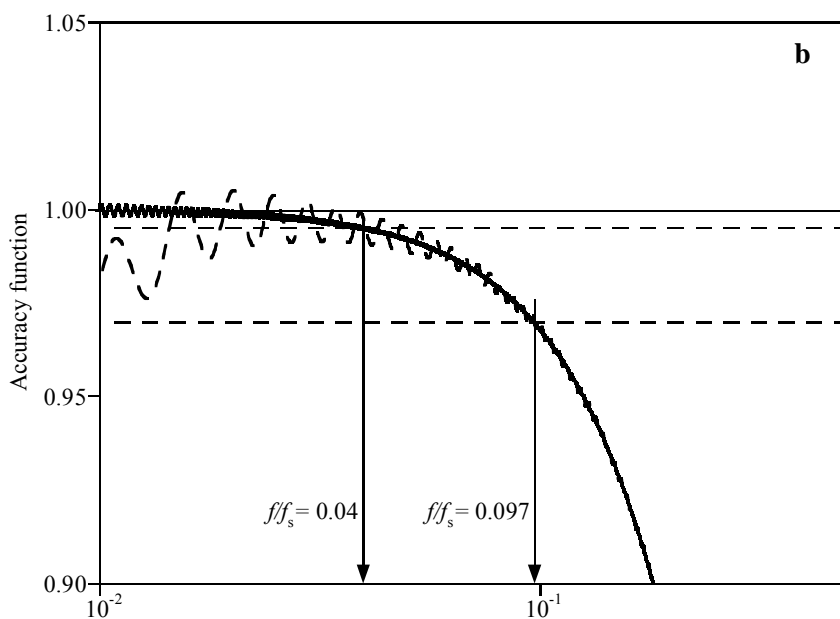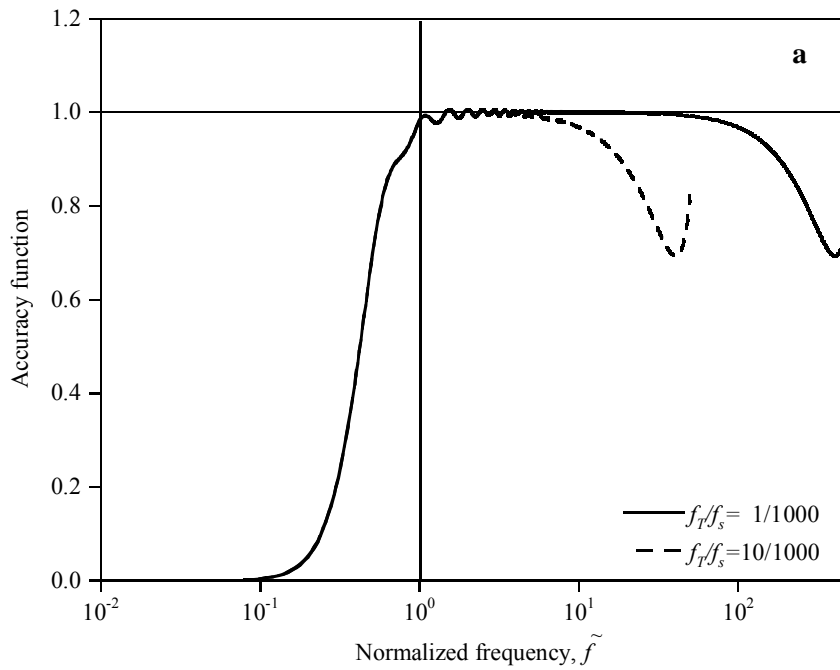
Figure 3-16. Accuracy functions of the FFIR filter with the standard filter size for two different TSF ratios: (a) Against the normalized frequency. (b) Against the frequency normalized to the sampling frequency.

The velocity transfer function of the FFIR filter is obtained by applying the Fourier transformation of Eq. (3-33). All real parts of the velocity transfer function vanish due to the anti-symmetry of the coefficients.

$$V_F(f) = 2i\Delta t \sum_{p=1}^{k} \hat{c}^F_{p+k+1} \sin(2\pi pf\Delta t) \tag{3-34}$$

where V_F is the velocity transfer function of the FFIR. As the exact transfer function for velocity is $1/i\omega$, the normalized transfer function $\widetilde{V}_F$ and the accuracy function V_F^{acc} of velocity are defined as follows.

$$\widetilde{V}_F(\widetilde{f}) = \frac{V_F(f)}{1/i\omega_T} = -2\pi\widetilde{f}_T 2\sum_{p=1}^{k} \hat{c}^F_{p+k+1} \sin(2\pi p\widetilde{f}_T\widetilde{f}) \tag{3-35}$$

$$V_F^{acc}(\widetilde{f}) = \frac{V_F(f)}{1/i\omega} = -2\pi\widetilde{f}_T\widetilde{f} 2\sum_{p=1}^{k} \hat{c}^F_{p+k+1} \sin(2\pi p\widetilde{f}_T\widetilde{f}) \tag{3-36}$$

The accuracy function of velocity is presented in Fig. 3-17 for two TSF ratios. As in the displacement reconstruction, most of the frequency contents smaller than the target frequency in measured accelerations are suppressed in the velocity reconstruction. The accuracy of the velocity reconstruction reaches 0.982 at the target frequency, and 0.97 at $0.1f_s$. The accuracy decreases rapidly after $0.1f_s$, and becomes zero at the Nyquist frequency.
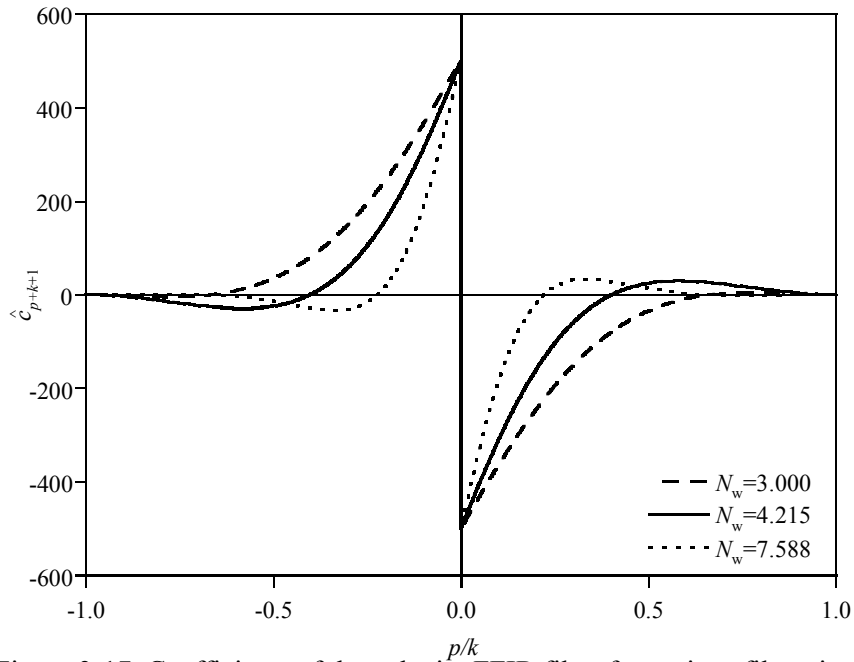
Figure 3-17. Coefficients of the velocity FFIR filter for various filter sizes
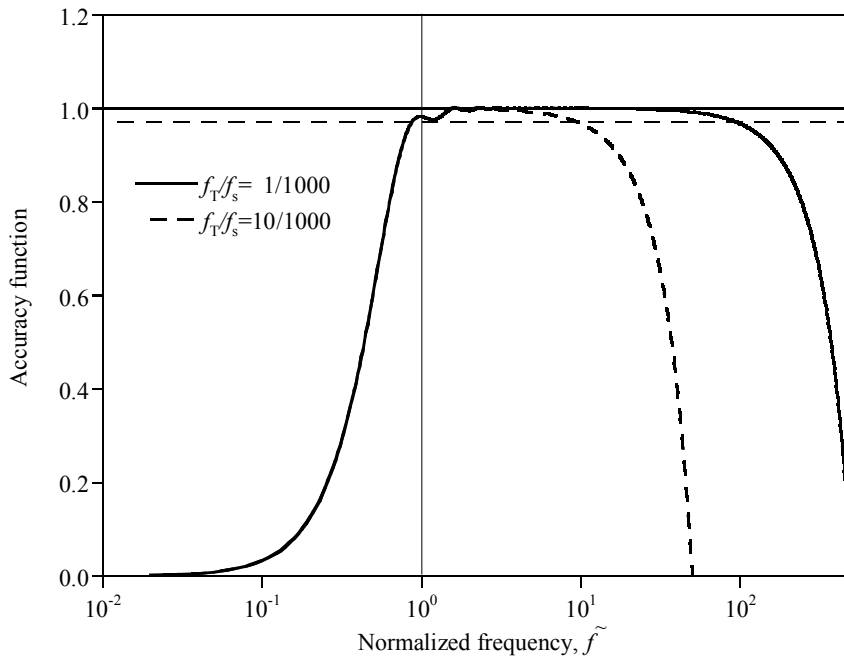
Figure 3-18. Velocity accuracy functions of the FFIR filter for various TSF ratios

68

An advantage of the FDM-FIR filter and FFIR filter over the CFIR filter is that the filter size can be flexibly selected as needed in actual applications. For example, a filter size shorter than the standard filter size may be employed to reduce computational effort for the real-time or near real-time reconstruction of displacement and/or velocity. However, shorter filter sizes lead to a less accurate transfer function at the target frequency and a larger rippling magnitude of the accuracy function.

3.2 Numerical and Experimental Verification for the FIR filters

The validity of the proposed FIR filters is demonstrated through a numerical simulation study, two laboratory experiments in different scales and a field test of a real railway bridge. The numerical study is presented to compare results by the proposed method with exact solutions quantitatively. Displacements as well as accelerations are measured in all cases, and the reconstructed displacements are compared with measured displacements. The fast Fourier transform (FFT) is utilized for the DFT. All calculations for the results presented here are performed after the completion of actual measurements. The instant when the displacement reconstruction begins is set to $t = 0$ throughout all the examples. The standard and long window sizes defined for CFIR filter are adopted for the filter size and 0.97 is used for the target accuracy. The results by the FDIA based on the BEF transfer function are also presented. For the real-time or near real-time processing, the overlapping time window technique, which is employed for FIR filters, is used for the FDIA.

As demonstrated in previous section with the transfer function and accuracy function of the FDM-FIR filter has nearly identical performance with the FFIR filter for the displacement reconstruction. Hence the results of the displacement reconstruction by the FDM-FIR filter are omitted in the forthcoming examples.

3.2.1 Numerical Simulation Study

The accelerations at the center of a simple beam with the span length of 40m

71

are measured.   The excitation force is applied at the location 12m right of the left support of the beam, and is defined as follows.

$$\Phi(t) = 8.9\sin15.4\pi t + 35.9\sin31\pi t + 29.3\sin56\pi t \qquad (3\text{-}37)$$

The forcing function given in Eq. (3-37) generates the maximum displacement of 1mm at the center of the beam during the force vibration.   The free vibration of the beam is introduced by withdrawing the excitation force at 6 second.   To obtain measured accelerations and displacements at the center of the beam, the dynamic analysis of the beam is performed by the finite element method using 10 elements with the Hermitian shape function [Hughes 1987].   The fundamental frequency of the beam is found as 6.22 Hz, and the frequencies of the excitation force are 7.70 Hz, 15.50 Hz and 28.00 Hz.

$$EI = 6.03 \times 10^{10}\,\text{N} \cdot \text{m}^2$$
Mass per unit length $= 1.5 \times 10^3$ kg/m
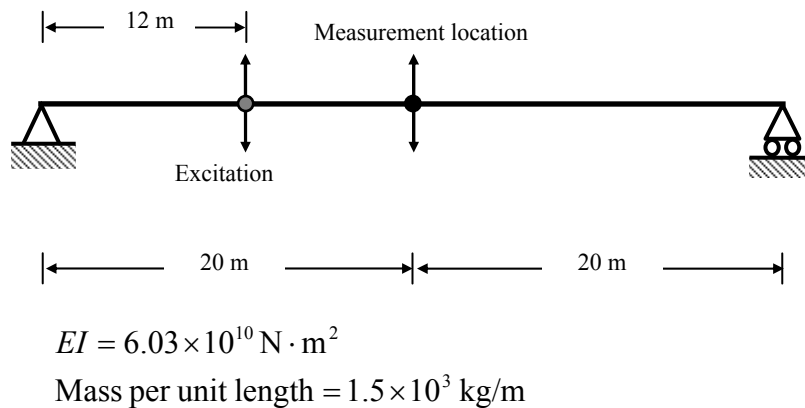
Figure 3-19. A simply supported beam for the numerical simulation study

The excitation force is withdrawn after 6 seconds to induce the free vibration of the beam. The Rayleigh damping model is adopted for the structural damping of the beam. The coefficients of the damping model are determined so that the modal damping ratios of the first and second mode are equal to 0.1%. The Newmark's method is employed for the dynamic analysis with a time increment of 0.001 second. Accelerations and displacements are measured at the sampling frequency of 1000 Hz.

The result of the FFT with the calculated accelerations is shown in Fig. 3-20, in which the normalization with respect to the maximum value is employed. Four dominant frequencies are identified at 6.17 Hz, 7.67 Hz, 15.5 Hz and 28.0 Hz.
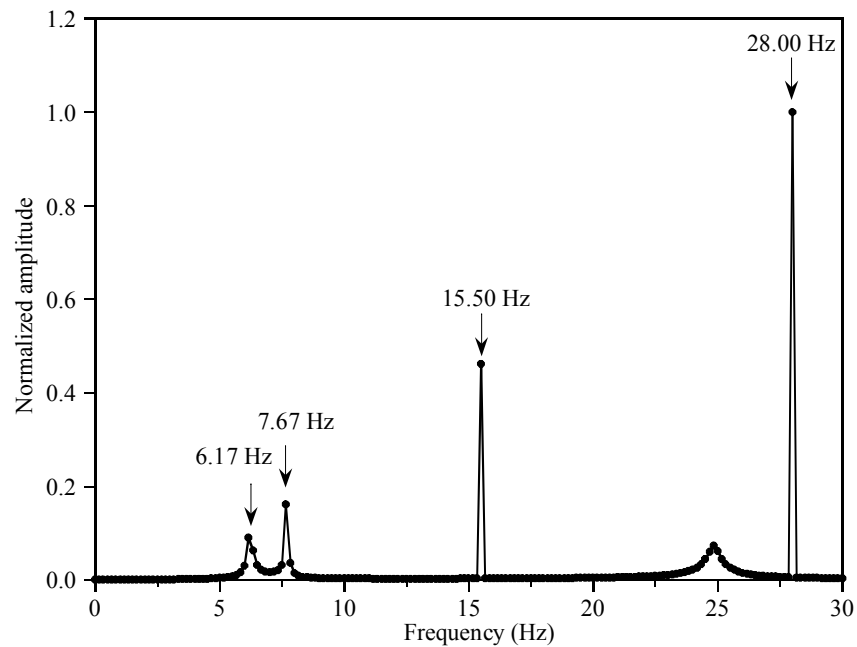
Figure 3-20. FFT of measured accelerations for the numerical simulation study

The lowest dominant frequency corresponds to the fundamental frequency of the beam, and the other three frequencies are the forcing frequencies. The minor peak at 24.80 Hz is the second natural frequency of the beam. The differences between the actual frequencies and identified frequencies are caused by the truncation and discretization errors that occur during the FFT.

From the lowest dominant frequency of the FFT result in the figure 3-20, 6.17Hz is selected for the target frequency of the reconstruction and 0.97 is used for the target accuracy. The standard and long window sizes corresponding to the target frequency are 0.684 second and 1.230 second, respectively
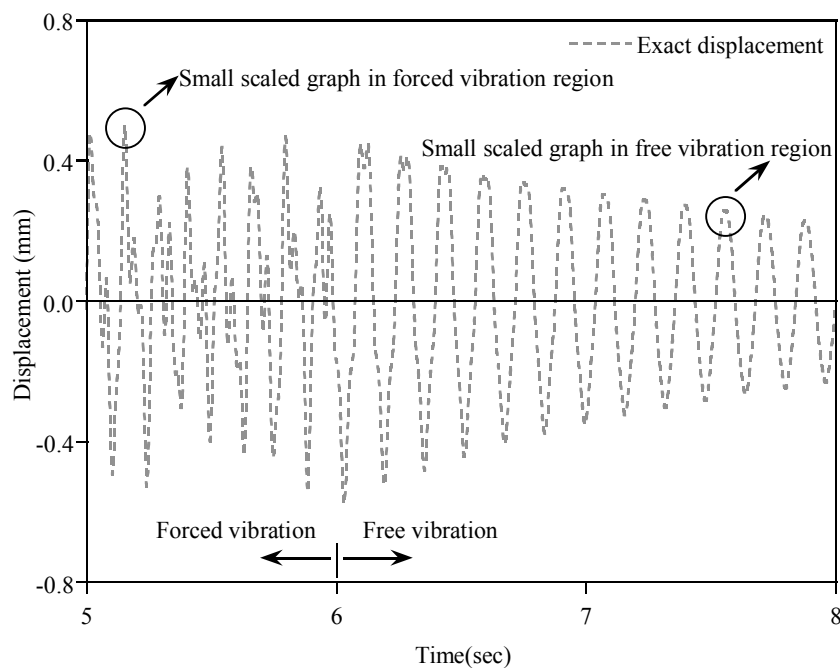
Figure 3-21. Exact displacement for the numerical simulation study

74
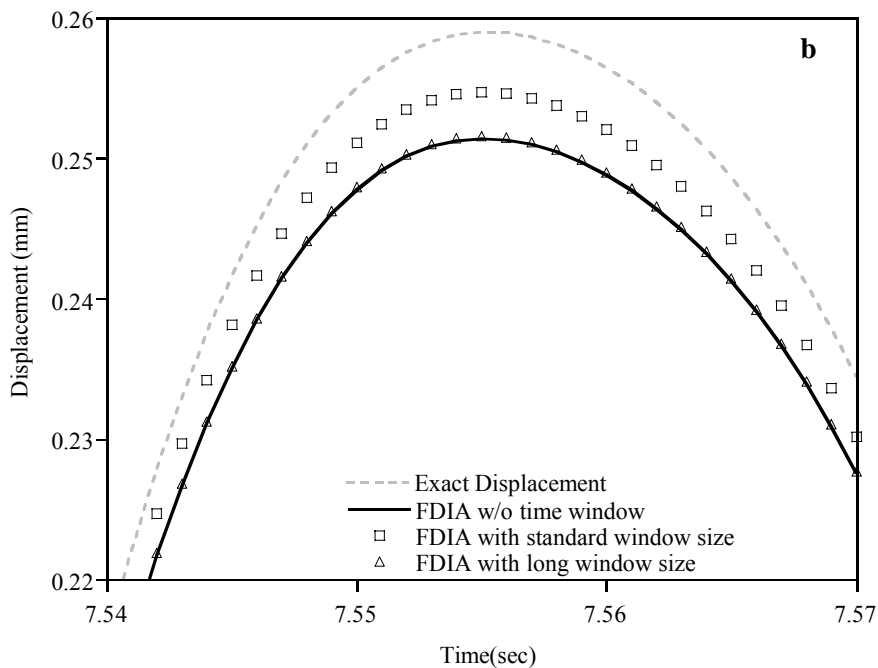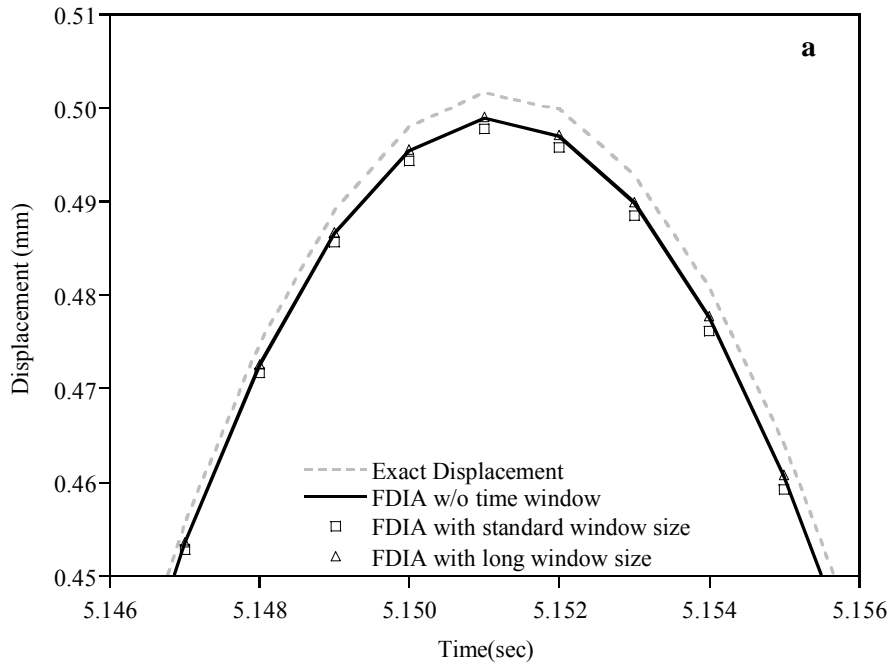
Figure 3-22. Details of the reconstructed displacement by FDIA with noise-free
data : (a) During the forced vibration. (b) During the free vibration.

Fig. 3-21 shows the exact displacement from 5 to 8 seconds. Since it is hardly to figure out the differences between reconstructed displacement and exact displacement in large scaled graph in Fig. 3-21, the details at the two peaks marked with circles in Fig. 3-21 are presented in following discussion for more accurate comparisons. Not only FDIA but also CFIR and FFIR yield almost same accuracy in the result of reconstruction, therefore the large scale graphs are skipped and just the details are illustrated hereafter.

Fig. 3-22 (a) and (b) show the details of the displacement reconstruction by FDIA during the forced vibration and free vibration for different window sizes together with the exact displacement, respectively. The overlapping window technique is employed for standard and long time-window sizes for the FDIA, and the FDIA with whole acceleration measurement without time window technique is tested for comparison.

The FDIA using the long window size yields almost same result with the FDIA without time window. It means that the long filter size is long enough to ignore the errors caused by the truncation and discretization of DFT which is discussed in section 2.1.2. The amplitudes of the reconstructed displacements by FDIA are slightly smaller than the exact displacement. Theoretically, if the input acceleration is single frequency component which only contains the target frequency component, the accuracy of reconstructed displacement should be 0.97 because the target accuracy is fixed to 0.97. However, in forced vibration region the dynamic responses contain multiple frequency components, the target accuracy not

hold for other frequency components except for the target frequency component.

This is more clearly seen in free vibration which contains nearly single dominant frequency component. The details of reconstructed displacements by the FDIA during the free vibration are drawn in Fig. 3-22 (b) for the standard window size and the long window size. As expected by previous discussion, the reconstructed displacement by FDIA with the long window size and without time window yield around 3 % error at the peaks, while the standard window size reconstructs slightly greater result at the peaks than other reconstructed displacement. No phase error is found in both the forced vibration and the free vibration.

The FDIA reconstructs displacement by applying the inverse Fourier transform to the Fourier transform of measured accelerations multiplied by the BEF transfer function. Though he FDIA yields very accurate result for the reconstruction but it requires a rather large computational effort, and may be inadequate for real-time or near real-time processing because the Fourier transform and the inverse Fourier transform should be performed for every reconstruction step.

The details of the reconstructed displacements by CFIR and FFIR are presented in Fig. 3-23 with the standard and long filter sizes, and compared with the exact displacement. No phase error is found in the reconstructed displacement by both filters. The reconstruction errors at the peak shown in Fig. 3-23 (a) by the FFIR filter for the standard and long filter sizes are evaluated as 0.8 % and 0.6%, respectively, and those by the CFIR filter for the two filter sizes as 1.3% and 0.5%, respectively.
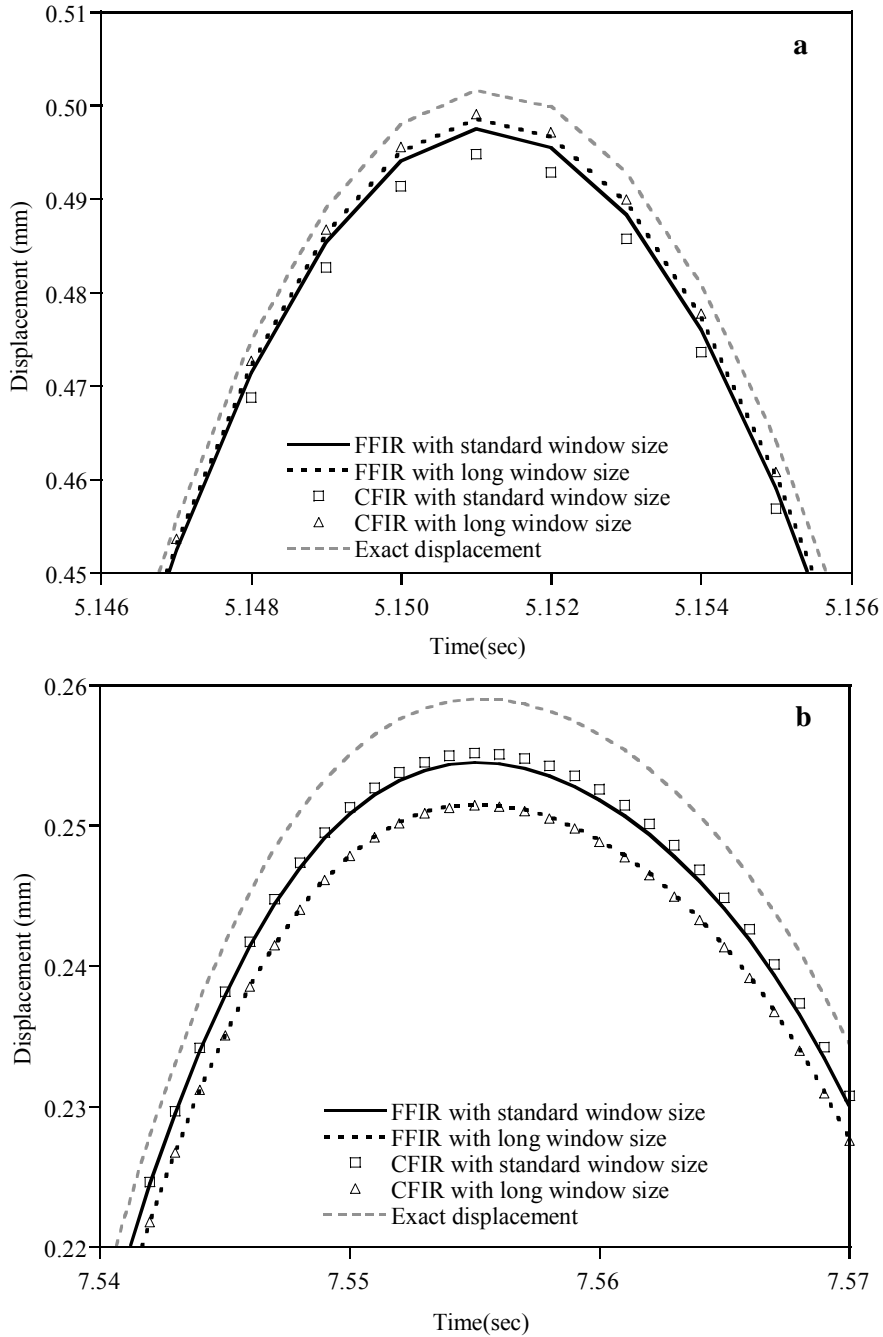
Figure 3-23. Details of the reconstructed displacement by CFIR and FFIR filter with noise-free data : (a) During the forced vibration. (b) During the free vibration.

The FFIR filter yields 1.8% and 2.9 % error for the standard and long filter sizes at the peak shown in Fig. 3-23 (b), respectively, and the CFIR filter yields 1.6% and 3.0 % errors for the two filter sizes.

The accuracy of the reconstructed displacement by the CIFR and FFIR filters at the peak shown in Fig. 3-23 (b) almost coincides with the accuracy of the BEF transfer functions corresponding to the filter sizes at the target frequency.   This is because the displacement components corresponding to the excitation frequencies have damped out, and only the displacement component corresponding to the fundamental frequency of the beam remains around the second peak.

To investigate the effect of noise on reconstruction results, displacement is reconstructed from noise-polluted accelerations and plotted in Fig. 3-24 together with those from noise-free accelerations.   The noise-polluted accelerations are simulated by adding 5% random proportional noise generated with the uniform probability function to the accelerations calculated by the finite element analysis.   The root mean square (RMS) errors in the measured accelerations and the displacement reconstructed by the proposed FIR filter with the standard filter size are shown in Tab. 3-1.   The 5% random proportional noise causes around 2.90 % RMS errors in the accelerations.   The RMS errors in the reconstructed displacements are around 4% for the forced vibration, and less than 2% for the free vibration, which demonstrates the robustness of the proposed filters against noise.   The reconstructed velocity from the noise-free accelerations is shown in Fig. 3-25.   Only the reconstruction results obtained by the FFIR filter with the standard filter size are

presented because differences between those with the long filter size and standard filter size are hardly noticeable for the scale of the figure. Although the details of the reconstructed velocity are not shown, the FFIR filter reconstructs the velocity at the same level of accuracy as the displacement.
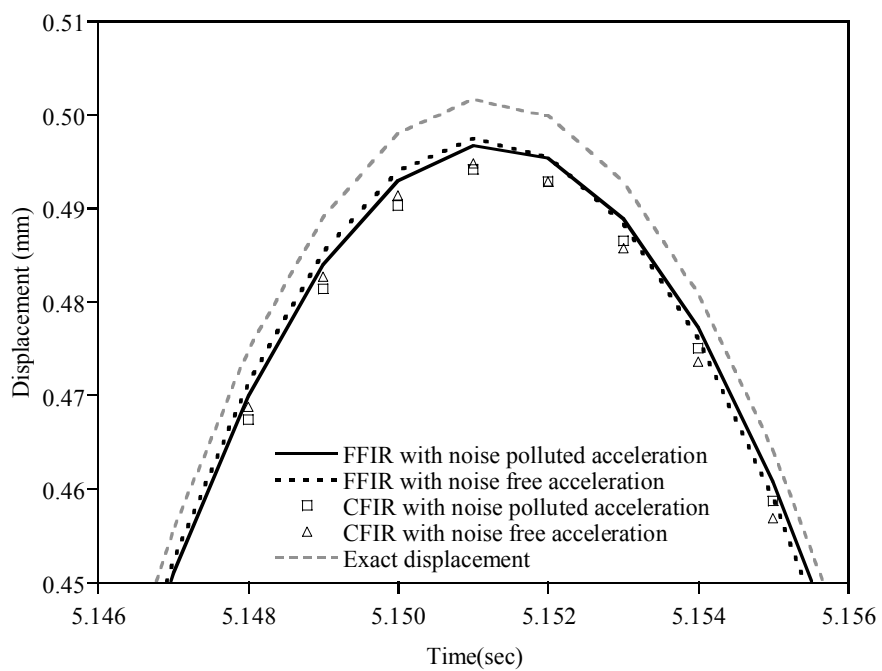
Figure 3-24. Effect of measurement noise on reconstructed displacement during the forced vibration with the standard filter size.
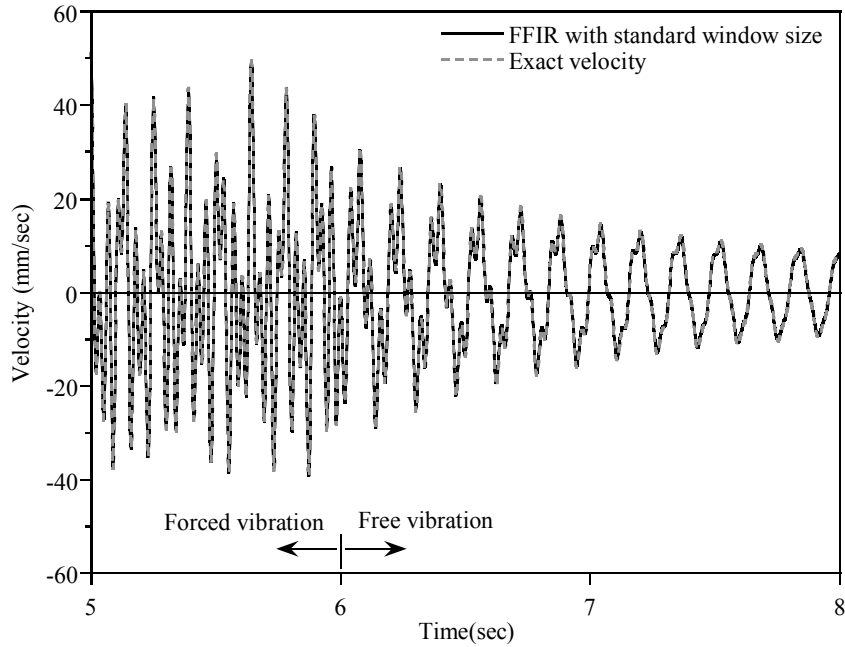
Figure 3-25. Reconstructed velocity by the FFIR filter with noise-free data

Table 3-1. RMS errors in measured accelerations and reconstructed displacements of example 1

Type of vibration	Acceleration		Reconstructed displacement(FFIR)		Reconstructed displacement(CFIR)	
	Noise free	5% Noise	Noise free	5% Noise	Noise free	5% Noise
Forced vibration	0.00 %	2.90 %	1.73 %	3.98 %	1.79 %	4.02 %
Free vibration	0.00 %	2.85 %	1.75 %	1.93 %	1.51 %	1.72 %

3.2.2 A Cantilever Beam subject to Base Motions

This experimental example is presented for the purpose of verification of the proposed method in the small scale laboratory setting, in which the measurement noise is relatively small but multiple frequency contents are contained in the dynamic responses.   The displacement is also reconstructed by the FDIA and CFIR method but omitted for the simplicity of the presentation.

One end of a small steel beam of 32.9cm×7.1cm×0.12cm is mounted on a vibration exciter to form a cantilever beam.   The vibration of the beam is induced by base motions generated by the exciter.   The overall setup for this experiment is illustrated in Fig. 3-26.
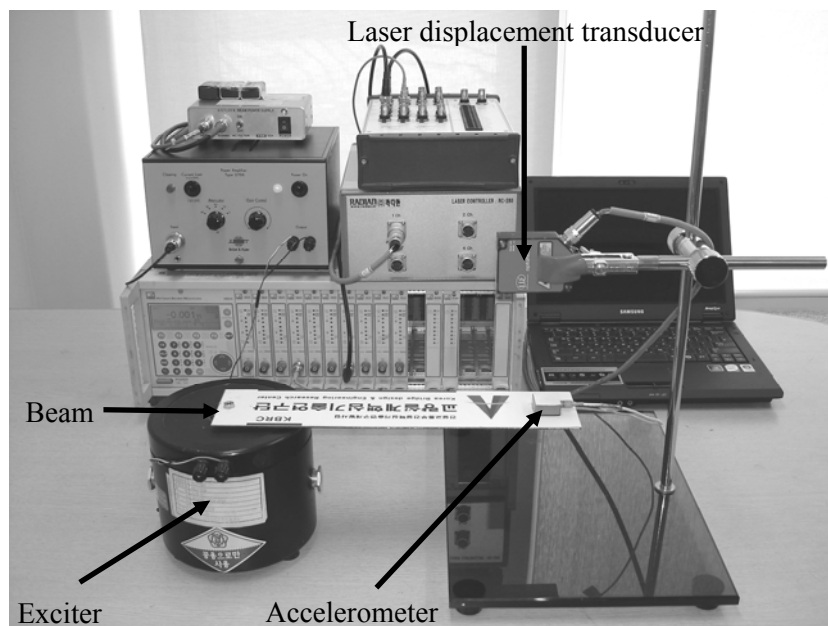
Figure 3-26. Experimental setup for the cantilever beam subject to base motions

82
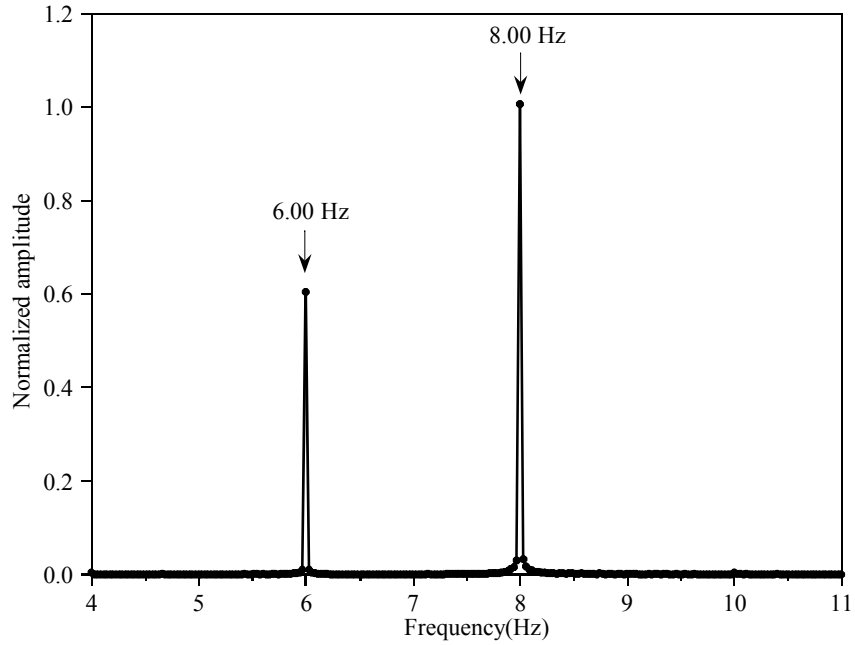
Figure 3-27. FFT with measured accelerations of the cantilever beam subject to dual frequency base motions
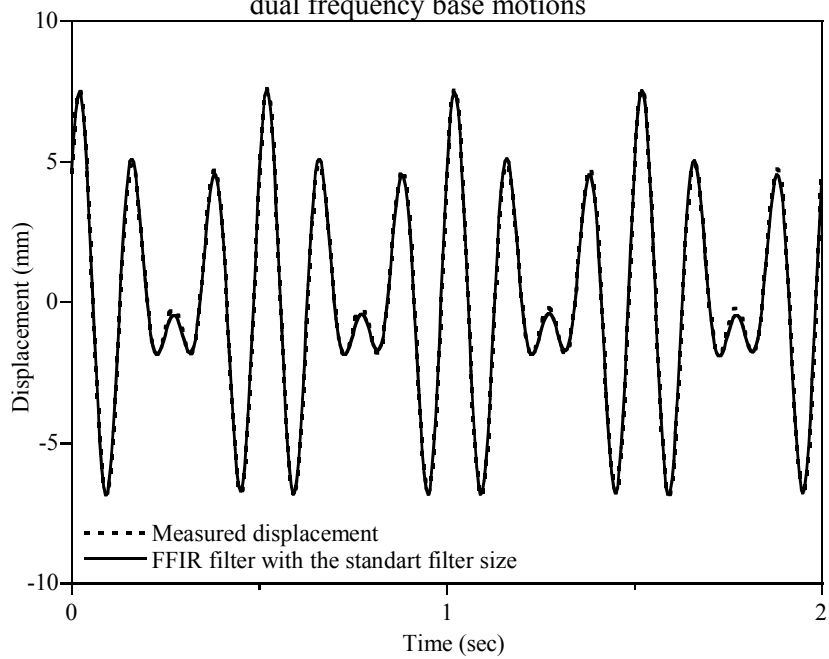
Figure 3-28. Reconstructed displacement of the cantilever beam subject to the dual frequency base motions

The acceleration and displacement are measured at the free end of the beam at a sampling rate of 200Hz.   The displacement is measured at the identical location of the accelerometer by a laser displacement transducer.   The model is excited by the base motion with dual frequency contents of 6Hz and 8Hz.   The dominant fundamental frequency is about 10Hz identified from the random excitation.

The results of the FFT with the measured accelerations are shown in Fig. 3-27. Three dominant frequencies of 6 Hz, 8 Hz and 9.96 Hz are identified.   The first two frequencies are the excitation frequencies, and the third minor frequency is the fundamental frequency of the cantilever beam.   From the result of FFT the lowest frequency, 6 Hz, are selected for the target frequency of dual frequency base motion test and the standard filter size is used for the FFIR filter.

The reconstructed displacements by FFIR filter with standard window size are compared with the measured displacements in Fig. 3-28.   In the figures, the phases and the amplitude of the vibrations are reconstructed accurately and the general history of the reconstructed displacement agrees well with that of the measured displacement in the overall sense.

3.2.3 Forced Vibration of a Stay Cable

A forced vibration test of a stay cable was performed at Structural Laboratory of Hyundai Institute of Construction, Kyungki-do, Korea.   The material properties of the stay cable are given in Table 3-2, and experimental setups, the geometry and

the boundary conditions of the cable are shown in Fig. 3-29.   Tension of approximately 300 kN is applied to the cable, and the fundamental frequency is calculated about as 1.5Hz.   The forced vibration of the cable is introduced with the cable exciter developed by Hyundai Institute of Construction at the center of the cable. The exciter generates vertical exciting forces by two rotating masses in the opposite direction.   The total mass of the exciter and the rotating mass are 14.58 kg and 0.46 kg, respectively.   The cable is excited by its fundamental frequency, i.e. 1.5Hz to induce the resonance of the cable for 40 sec.   An accelerometer is installed at the center of the stay cable and the vertical acceleration is measured at the sampling rate of 100 Hz.   A linear variable differential transformer (LVDT) is installed at 20cm away from the accelerometer to avoid interference between the exciter and the LVDT.   The LVDT measures vertical displacement at the same sampling rate as the accelerometer.   The FFT of the measured acceleration yields the dominant frequency of 1.48 Hz, which is slightly smaller than the excitation frequency.   The standard window size is used for the displacement reconstruction with the FFIR filter.

Table 3-2. Material properties of the stay cable

Young's Modulus (KN/mm^2)	Area (mm^2)	Weight (N/m)	Fundamental Frequency (Hz)	Unstrained length (L_0) (m)	Sag Ratio
200	2.348	199.075	1.52	44.304	1/310.8
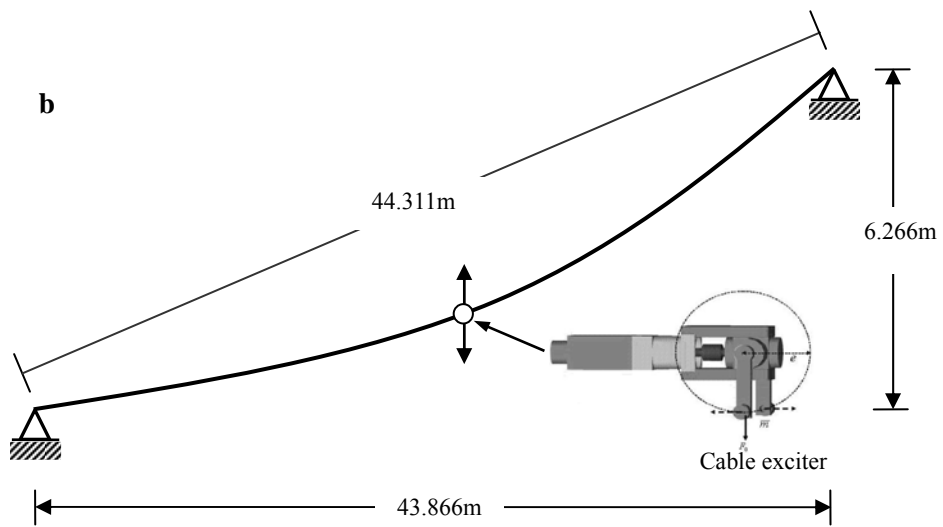
Figure 3-29. Forced vibration experiment of a stay cable: (a) Experimental setup.
(b) Dimensions and the boundary condition of a stay cable

The reconstructed results are shown in Fig. 3-20 for the two periods around the beginning of the excitation and the end of the excitation. In the figure, the reconstructed displacement agrees with the measured displacement from the LVDT well except for a small, constant phase difference. It is believed that the phase difference is caused by the difference in positions between the accelerometer and the LVDT. In Fig. 3-30 (a), the displacement reconstructed by the Newmark's method is drawn together with the others. The Newmark's method yields diverging displacement after 2 sec even though the exact initial conditions are specified.
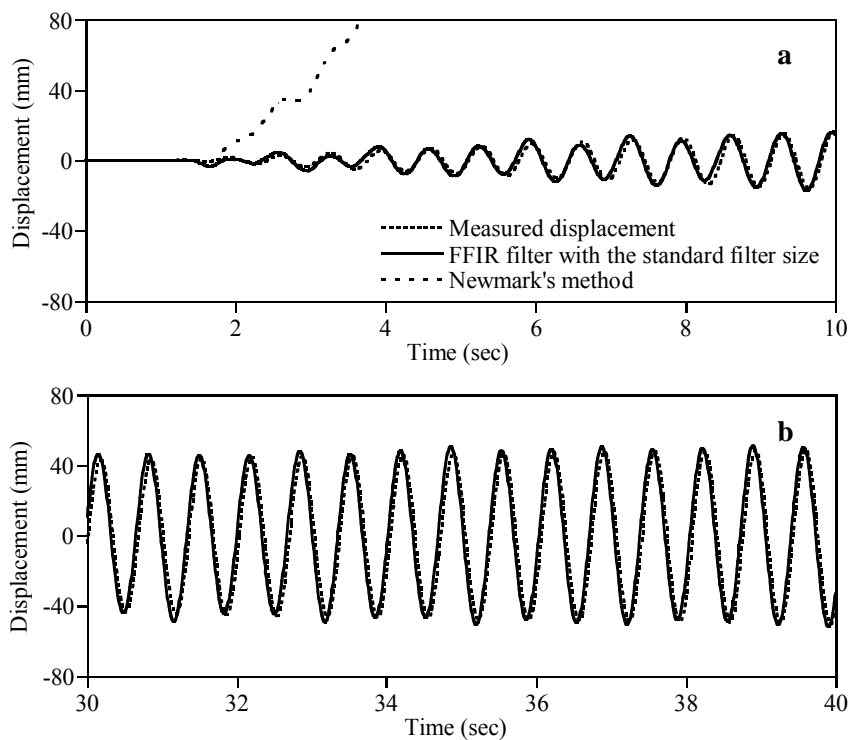
Figure 3-30. The reconstructed displacement of the stay cable by FFIR filter with strandard window size : (a) Near the beginning of the excitation. (b) Near the end of the excitation

87
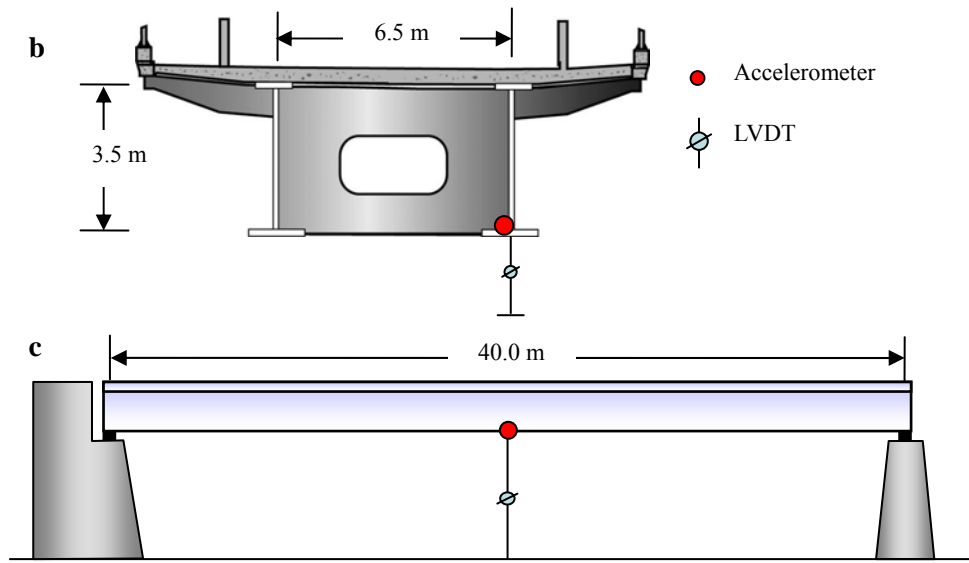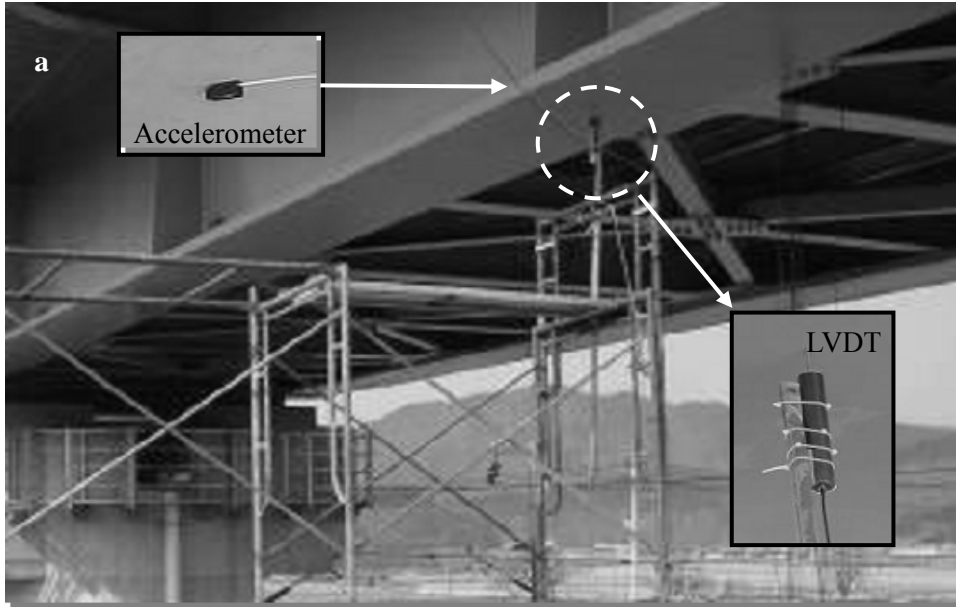
Figure 3-31. Measurement of the simply-supported span of in a KTX railway
bridge: (a) Installation of sensors. (b) Typical section and location of sensors. (c)
Simply-supported span

3.2.4 Field Test on a Simply supported Railway Bridge under a Moving Train

The acceleration and the displacement are measured at the center of a 40m simply-supported span of a railway bridge on the Gyeongbu line of the Korea Train Express (KTX). The measurement is taken at a sampling frequency of 1,000 Hz while an actual train passes the bridge during commercial operation. A linear variable differential transformer (LVDT) is used to measure displacement. The overall instrumentation for the measurement, a typical cross-section and the measurement location are illustrated in Fig. 3-31. The experiment is conducted by Steel Structure Research Laboratory of Research Institute of Industrial Science and Technology, Kyungki-do, Korea. Three dominant frequencies of the bridge are found at 2.86 Hz 3.86 Hz and 5.79 Hz by the FFT of the measured accelerations. The first dominant frequency corresponds to the excitation frequency of the moving train, and the second one is the first natural frequency of the bridge. The standard window size is used for the displacement reconstruction with the CFIR and FFIR filter.

Unlike the previous examples, the pseudo-static displacement is included in the measured displacement due to the moving train. Here, the pseudo-static displacement denotes the displacement obtained by neglecting the dynamic effect of the moving train on the bridge. Because the pseudo-static displacement has nothing to do with the measured acceleration, the purely dynamic displacement can be reconstructed by the proposed method. Therefore, to compare the reconstructed displacement by the proposed method to the measured displacement, the pseudo-static component in measured displacement should be eliminated. As the bridge

vibrates around the pseudo-static displacement, the moving average of the measured displacement [Montgomery 2005] over the longest dominant period is considered to be the pseudo-static displacement, and the dynamic displacement is estimated as follows.

$$u_d(t) = u_m(t) - \frac{1}{T} \int_{t-T/2}^{t+T/2} u_m(\tau) d\tau \qquad (3\text{-}38)$$

where $u_d(t)$, $u_m(t)$ and T are the extracted dynamic displacement, the measured displacement at time t and the longest period, respectively.   The integral term in Eq. (3-38), which is evaluated by the trapezoidal rule, represents the estimated pseudo-static displacement.   The numerically integrated extraction scheme forms a FIR filter as well.   As like to the displacement reconstruction scheme, the transfer function of this FIR filter is derived by applying the Fourier transform to the numerically integrated expression of Eq. (3-38).   The transfer function of the dynamic displacement extraction reveals the accuracy of the extracted dynamic displacements in the frequency domain compared to the measured displacements. The transfer function of this extraction is shown in Fig. 3-32, and its values at the three dominant frequencies are found as 1.001, 1.210 and 0.987 in the ascending order of the frequencies.   The dynamic displacements corresponding to the first and third dominant frequency are extracted accurately, but those corresponding to the second dominant frequency are overestimated by 21% during the extraction.
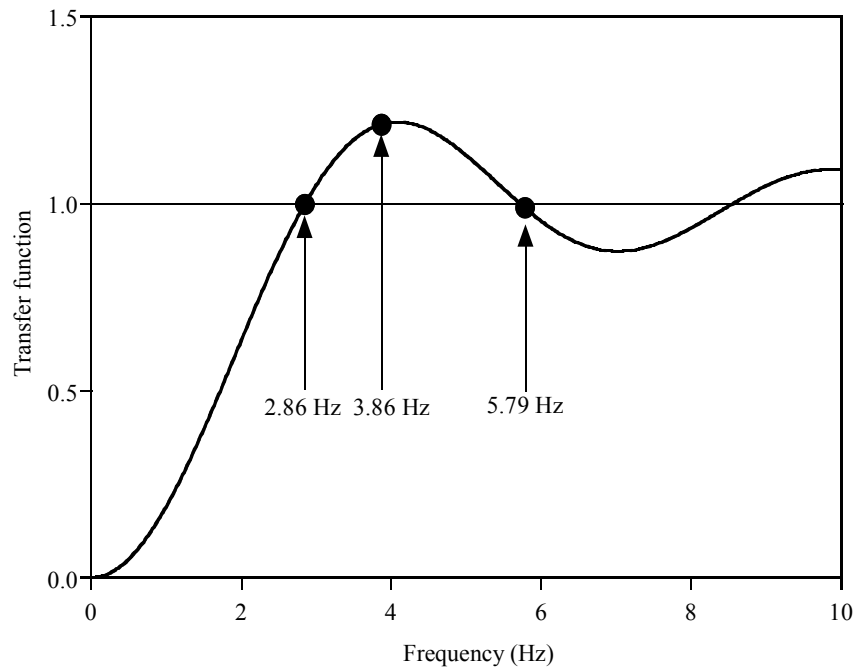
Figure 3-32. Transfer function of the dynamic displacement extraction scheme

The measured displacement and the estimated pseudo-static displacement are presented in Fig. 3-33.   As formulated, the measured displacement oscillates around the pseudo-static displacement.   The difference between the two displacements becomes the extracted dynamic displacement.   Fig. 3-34 compares the extracted dynamic displacement with the reconstructed displacement using the FFIR, and Fig. 3-35 shows the details of Fig. 3-34 during the period when the train is completely on the span.   The train enters the bridge at 0.5 seconds, begins to exit the bridge from 7.7 seconds and completely leaves the bridge at 8.4 seconds.   The aforementioned instants are not measured values but estimated ones based on the measured displacements in Fig 3-34.
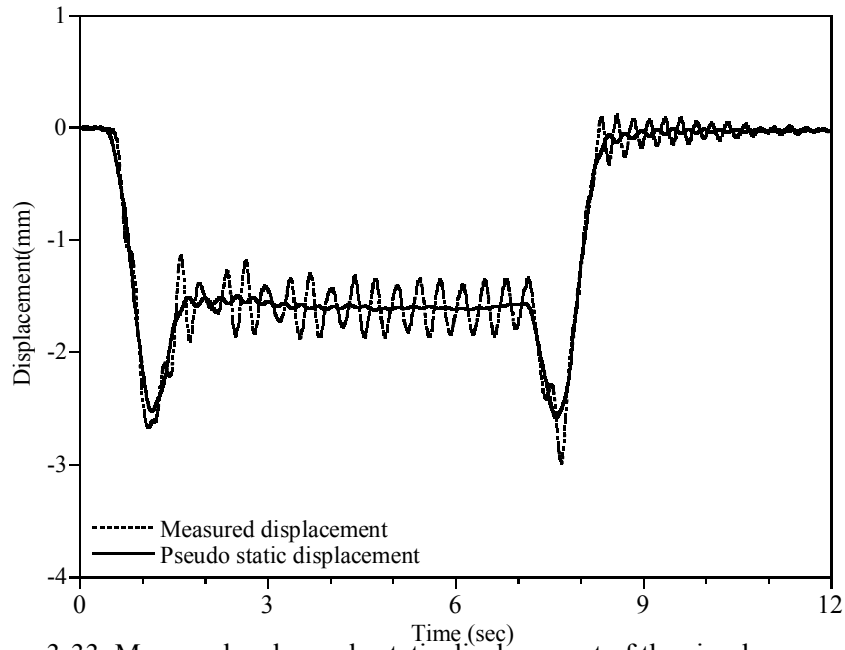
Figure 3-33. Measured and pseudo static displacement of the simply-supported railway bridge
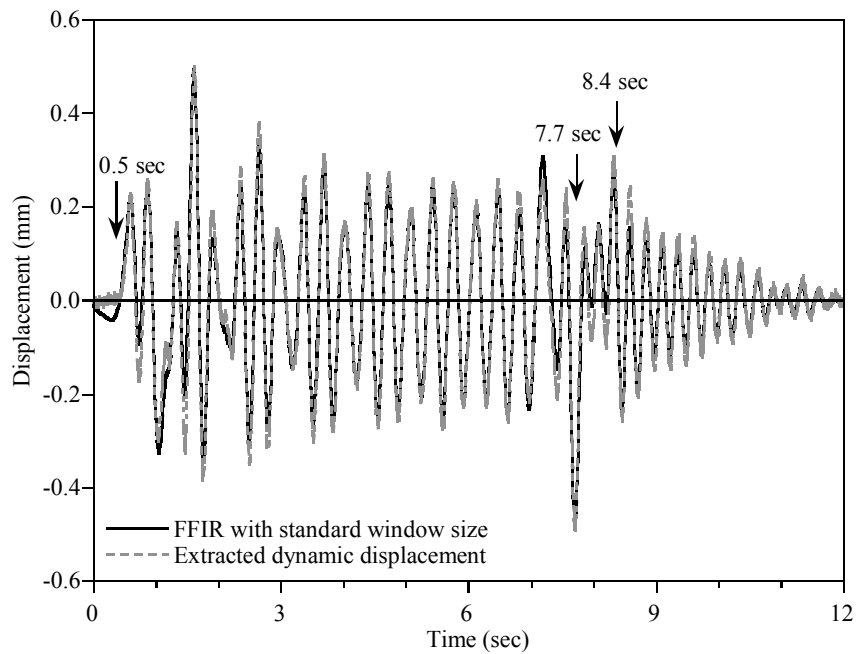
Figure 3-34. Reconstructed and extracted dynamic displacement of the simply-supported railway bridge with standard filter size
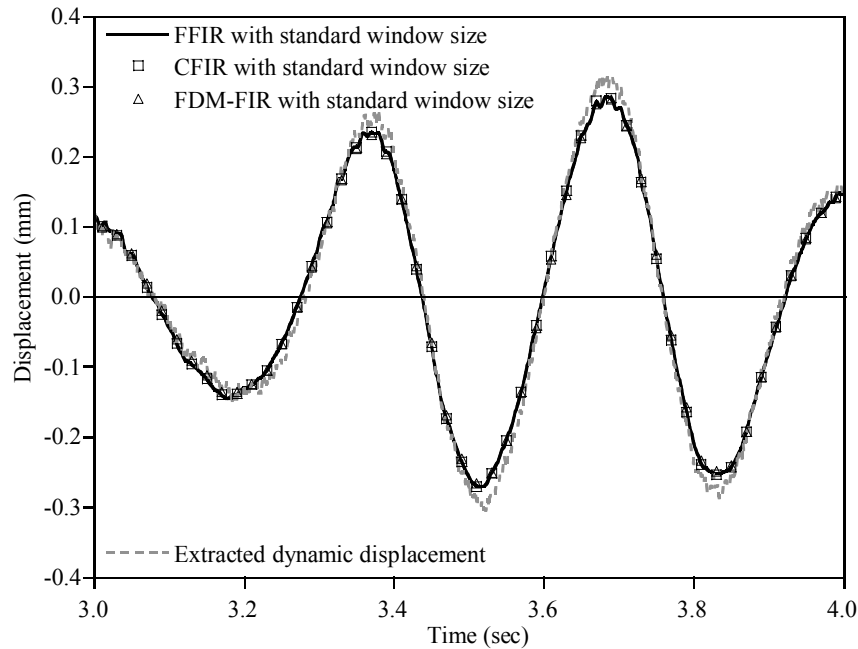
Figure 3-35. Details of reconstructed and extracted dynamic displacement

Figure 3-34 shows the extracted dynamic displacement by Eq. (3-38) and the reconstructed displacement by the FFIR filter. Results by the CFIR appear to be almost identical to those of the FFIR filter, and are not presented in the figure. When the train is on the bridge, the forced vibration is dominant. After the train leaves the bridge, the free vibration governs the responses of the bridge. The maximum differences between the reconstructed and extracted dynamic displacement at peaks are found as about 10% during the forced vibration, and those during the free vibration as about 25%. The details of reconstructed displacements by the CFIR filter, FFIR filter and the FDM-FIR filter are compared with the extracted dynamic displacement in Fig. 3-35. The three FIR filters yield almost identical results, and no noticeable difference is found in either the amplitude or the phase.

93

The discrepancies between the extracted and reconstructed displacements are strongly caused by the dynamic displacement extraction scheme in Eq. (3-38). As illustrated above, the displacement component corresponding to the second dominant frequency is overestimated by 21% during the extraction. Since the accuracy bound of the proposed filter is set to be 3% with the target accuracy of 0.97, the discrepancy of 25% in the free-vibration region is in an acceptable range regarding to 21% error of the dynamic displacement extraction scheme. Hence, the reconstructed displacements represent actual dynamic displacements better than the extracted displacements.

4. Special Application of the Reconstruction for the Identification of Flutter Derivatives.

The flutter derivatives identified from wind tunnel tests are indispensable parameters for the analyses of dynamic behaviors of long-span bridges induced by wind. The interaction between a fluid flow and an embedded elastic structure is extremely complex especially for the bluff body section. Different response modes and flow phenomena exist depending on the flow characteristics, the body geometry and the structural properties like stiffness and damping. This poses a particular challenge to the development of analytical and numerical models and renders experimental methods still the most reliable tool.

The mutual influence of structural dynamics and fluid flow in regions of moving boundaries makes this particularly challenging and the corresponding subject is termed aeroelasticity. The aero-dynamic force acts as an outer force for the structural system, and the motion of structure recursively influence to boundary conditions of the aero-dynamic force. This moving boundary problem has several nonlinearity regard to the amplitude, the vibrational mode shape and etc. [Falco 1992, Matsumoto 1993 and Morgenthal 2000] caused by the interaction and the flutter derivatives should be determined by proper experimental procedures which can consider this nonlinear effect of the original problem.

Although the aeroelastic system is nonlinear, the flutter analysis and the iden-

tification of the flutter derivatives are commonly based on the assumption of linear elastic system behavior [Simiu 1996]. A popular set of expressions for the aerodynamic forces on a cross section in motion is the one proposed for bridge deck analysis by Scanlan and Tomko (1971), which is based on the assumption that the self-excited lift and moment on an elastic section model are treated as linear in the structural vertical and rotational displacement and their first derivatives.

The flutter derivatives can be identified with different experimental procedures from an idealized 2-DOF section model, i.e. forced-vibration test and free-vibration test. The most widely adopted technique is the free-vibration method. The original concept of the flutter derivatives was proposed by Scanlan and Tomko (1971) with a primitive experimental procedure consisted of three separate wind tunnel tests; two 1-DOF free-vibration tests for the vertical and the rotational directions, and one single frequency free-vibration 2-DOF test. To circumvent complexity of the experimental procedure proposed by Scanlan and Tomko (1971), a great deal of effort has been made for decades to identify all the flutter derivatives from a single 2-DOF free-oscillation test [Bartoli 2009, Chen 2004, Chowdhury 2003, Gu 2000, Iwamoto 1995, Li 2003, Matsumoto 1993, Sarkar 1992 and Sarkar 1994]. In these procedures, a 2-DOF section model is elastically suspended in a given initial condition and suddenly released from the imposed initial position, and then the flutter derivatives are extracted from the history of the free-decaying motions in vertical and rotational direction. Although free-vibration technique requires relatively complicated procedure to identify the flutter derivatives and need

additional assumption because of the uncertainty of frequency similarity, but it is appealing for the simple setup and the possibility for the realization of interaction between the structure and the wind.

A more reliable procedure is forced-vibration method [Diana 2004, Falco 1992, Kim 2007 and Matsumoto 1993] in the sense of the law of similarity. Although this method requires a sophisticated driving instrument, it yields the steady state response in a single frequency, which exactly coincides with the fundamental assumption of the aero-dynamic force proposed by Scanlan and Tomko (1971). The forced-vibration test can be controlled by two different methods, a displacement-control technique and a force-control technique.

Generally, the forced-vibration test is conducted by imposing a sinusoidal displacement to the section model without the elastic suspension of the springs, namely by the displacement-control method. However, if the body is controlled to oscillate in a prescribed motion, the nonlinearity of the original aeroelastic system may be not fully considered in the experimental procedure because of the predefined boundary condition. On the other hand, the force-control method dose not imposes the motion itself, but just excites the section model with an outer force to yield a steady state motion after the end of full interaction.

As the selection of the experimental procedure, different numerical algorithms are employed for the extraction of the flutter derivatives. Numerous SI algorithms used for the free-vibration technique is inappropriate for the steady state response of the forced-vibration test and vice versa. As far as the author knows of,

the general algorithm that can be employed for extraction of flutter derivatives regardless of the testing procedures has not been proposed yet. Moreover the state variables such as the displacement, velocity and acceleration are not fully measured in the experimental procedures, i.e. the displacement is the only kind of the measured data. By the absence of full measurement of the state variables, the SI algorithm, which is based on the output error estimation (OEE) [Hjelmstad 1995] with the state-space model, is inevitable for the extraction of the flutter derivatives in the free-vibration test. In the OEE scheme, if the analytic solution is nonlinear with respect to the unknown system parameters, it can not yield a quadratic minimization problem; hence it requires a complicated sensitivity analysis or a complex eigen-value analysis to identify the unknown system parameters.

This thesis proposes a new approach to identify the flutter derivatives by minimizing an equation error estimator (EEE) [Hjelmstad 1995] which is defined as the least-square errors between structural resistance forces and aeroelastic forces induced by wind. Dissimilar to the other SI algorithm, the proposed method can successfully employed for the identification of flutter derivatives regardless of the experimental procedure and do not require any complicated sensitivity analysis or complex eigen-value analysis to identify the unknown system parameters.

The EEE requires complete information on the state variables at all time steps. In the proposed method, accelerations of a section model are measured with accelerometers in wind tunnel tests while the velocities and displacements corresponding to the measured accelerations are reconstructed by the FFIR filter in chapter 3.

Hence, the EEE method in this thesis is solely based on the measured acceleration. Measurement of acceleration has certain advantages over measurement of displacement in various engineering applications. The most distinctive advantage in the measurement of acceleration over that of displacement is that acceleration is measured without any fixed reference point, which opens a possibility to identify flutter derivatives of real long-span bridges in service. Moreover, various types of accelerometers are commercially available at relatively low costs.

The validity of the proposed method in the free-vibration test is demonstrated for two types of bridge sections; a thin rectangular section and a bluff H-type section. The former section represents a streamlined section used in relatively long-span bridges, and the latter simulates a slab-on-stringer type section often applied to medium-span cable-stayed bridges. It is shown that the flutter derivatives identified by the proposed method agree well with those by the MITD method and/or those by the Theodorsen function [Simiu 1996]. The forced-vibration tests are not implemented yet in our wind tunnel, but by the virtue of the analytic solution of the force-control test proposed by Jung et al. (2011) the validity of the proposed method to the force-control test is verified by the numerically simulated example.

4.1 System identification with OEE and EEE for general dynamic system

In this section the two concepts of the system identification for the linear-time in-variant system are summarized. If the responses are fully measured for all de-grees of freedom, it will be referred to the full measurement in space, while if the responses for all state, such as a displacement, a velocity and an acceleration, are fully measured for a fixed material point, it will be referred to the full measurement in state.

Generally the dynamic responses are not fully measured in both space and state. The system identification for partially measured responses can not be di-rectly solved from the force equilibrium equation but should be solved by minimiz-ing error between the analytic solution responses of the problem and the limited measurement responses. These kinds of the system identification methods are called by the output error estimation method (OEE). In the OEE scheme, if the analytic solution is nonlinear with respect to the unknown system parameters, it can not yield a quadratic minimization problem. Hence it requires a complicated sensitivity analysis or a complex eigen-value analysis to identify the unknown sys-tem parameters [Hjelmstad 1995, Park 2008 and Sarkar 1992].

By the virtue of the FFIR filter in the previous section, if the only acceleration is fully measured in space, the displacement and velocity can be reconstructed and complete measurement in both space and state is possible. The full measurement data can be successively employed for the system identification directly using the

force equilibrium equation. This system identification method is called by the equation error estimation method (EEE). In the EEE, the minimization problem yields the quadratic problem with respect to the unknown system parameters; hence, the unknown system parameters can be identified from the first order necessary condition without the complicated sensitivity analysis or the complex eigenvalue analysis.

Though the general concept of the OEE and the EEE in following section is valid for the dynamic system regardless of the number of DOFs, but for the convenience of the presentation, 2-DOFs system is selected for the description. In SI procedure, it is supposed that the mass matrix and the excitation force is given and known in priori and the responses are fully measure in space.

4.1.1 System identification based on output error estimation method (OEE)

The second order differential equation for the general dynamic system in Eq. (2-1) is described by following equation in state-space model to acquire the analytic solution from the first order differential equation.

$$\dot{\mathbf{x}}(t) = \mathbf{A}_s \mathbf{x}(t) + \mathbf{B}_s \mathbf{p}(t) \qquad (4-1)$$

where $\mathbf{x}(t) = \begin{bmatrix} u(t) & v(t) \end{bmatrix}^T$ is the state variable for a given time, while $\mathbf{A}_s$ and $\mathbf{B}_s$ are system matrix and the input influence matrix which are defined as follows:

$$\mathbf{A}_s = \begin{bmatrix} \mathbf{0} & \mathbf{I} \\ -\mathbf{M}^{-1}\mathbf{K} & -\mathbf{M}^{-1}\mathbf{C} \end{bmatrix}, \quad \mathbf{B}_s = \begin{bmatrix} \mathbf{0} \\ \mathbf{M}^{-1} \end{bmatrix} \tag{4-2}$$

here the subscript '*s*' denotes the state-space model.

The analytic solution for the general dynamic system in Eq. (2-1) is described by following equation in state-space model.

$$\mathbf{x}(t) = e^{\mathbf{A}_s(t-t_0)}\mathbf{x}(t_0) + \int_{t_0}^{t} e^{\mathbf{A}_s(t-\tau)}\mathbf{B}_s\mathbf{p}(\tau)d\tau \tag{4-3}$$

where $\mathbf{x}(t_0) = \begin{bmatrix} u(t_0) & v(t_0) \end{bmatrix}^T$ is the initial condition at time t_0.

The system identification with OEE is based on the assumption of the partial measurement of the state variable, $\mathbf{x}$.

$$\mathbf{y}(t) = \mathbf{C}_s\mathbf{x}(t) + \mathbf{D}_s\mathbf{p}(t) \tag{4-4}$$

where $\mathbf{y}(t)$ is observable or output variable, $\mathbf{C}_s$ and $\mathbf{D}_s$ are the output influence matrix and the direct transmission term, respectively. Substitution of Eq. (4-3) to Eq. (4-4) yields following equation for the analytic solution of the observable variable.

$$\mathbf{y}(t) = \mathbf{C}_s e^{\mathbf{A}_s(t-t_0)}\mathbf{x}(t_0) + \mathbf{C}_s\int_{t_0}^{t} e^{\mathbf{A}_s(t-\tau)}\mathbf{B}_s\mathbf{p}(\tau)d\tau + \mathbf{D}_s\mathbf{p}(t) \tag{4-5}$$

Supposing the state variable is fully measured in space but is partially meas-

102

ured in state, i.e. the state variable is fully measured for all degree of freedoms in space domain but just one of state variables such as the displacement, the velocity and the acceleration is measured, the output influence matrix and the direct transmission term are represented by the following equations for three individual state measurements.

For displacement

$$\mathbf{C}_s = \begin{bmatrix} \mathbf{I} & \mathbf{0} \end{bmatrix} \text{ and } \mathbf{D}_s = \mathbf{0} \tag{4-6}$$

For velocity

$$\mathbf{C}_s = \begin{bmatrix} \mathbf{0} & \mathbf{I} \end{bmatrix} \text{ and } \mathbf{D}_s = \mathbf{0} \tag{4-7}$$

For acceleration

$$\mathbf{C}_s = \begin{bmatrix} -\mathbf{M}^{-1}\mathbf{K} & -\mathbf{M}^{-1}\mathbf{C} \end{bmatrix} \quad \mathbf{D}_s = \mathbf{M}^{-1} \tag{4-8}$$

The purpose of OEE methods is to minimize the relative error between measured response and output response which is calculated from the mathematical model in Eq. (4-5) respect to the unknown system parameters of the dynamic system.

$$\underset{\mathbf{X}}{\text{Min}} \, \Pi(\mathbf{X}) = \frac{1}{2} \sum_{i=1}^{nt} \left\| \overline{\mathbf{y}}(t_i) - \mathbf{y}(\mathbf{X}, t_i) \right\|_2^2 \tag{4-9}$$

where $\mathbf{y}(t_i)$ and $\overline{\mathbf{y}}(t_i)$ are output (or calculated) response and measured response vector at time t_i, and nt and $\left\| \cdot \right\|_2$ are the number of time steps used in the identification and the 2-norm of a vector, respectively, while $\mathbf{X}$ is unknown sys-

103

tem parameter vector.   Supposing the mass matrix is known in prior and the components of the damping matrix and the stiffness matrix are the unknown system parameters, $\mathbf{X}$ can be written as following equation for 2-DOF system.

$$\mathbf{X} = \begin{bmatrix} c_{11} & c_{12} & k_{12} & k_{11} & c_{21} & c_{22} & k_{22} & k_{21} \end{bmatrix}^{\mathrm{T}} \tag{4-10}$$

where c_{ij} and k_{ij} are the individual components of the damping and stiffness matrix, respectively.   Note that the sequence of each component has no physical meaning but the components are aliened in Eq. (4-10) for the convenience of applying to the flutter derivatives example in the next section.

$$\mathbf{C} = \begin{bmatrix} c_{11} & c_{12} \\ c_{21} & c_{22} \end{bmatrix}, \qquad \mathbf{K} = \begin{bmatrix} k_{11} & k_{12} \\ k_{21} & k_{22} \end{bmatrix} \tag{4-11}$$

The system parameters can be successively identified by OEE methods to minimize relative errors in responses.   Since, however, the solution of the dynamic system in Eq. (4-5) are not linear with respect to the unknown parameters in Eq. (4-10), the minimization problem in Eq. (4-9) can not yield the quadratic problem with respect to the unknown parameters.   Hence, as mentioned in the beginning of this section, the complicated sensitivity analysis or complex eigen-value analysis with the iterative procedure should be employed to identify the system parameters.

4.1.2 System identification based on equation error estimation method (EEE)

In case the complete time history of displacement, velocity and acceleration

are available, the unknown system parameters can be identified by the minimization procedure based on the EEE.

For convenience of formulation, the known parts and unknown parts of Eq. (2-1), are represented as following separated functions defined in discrete time step, t_i.

$$\mathbf{F}_{kn}(t_i) = \mathbf{M}\mathbf{a}(t_i) - \mathbf{p}(t_i) \tag{4-12}$$

$$\mathbf{F}_{un}(\mathbf{X}, t_i) = -\mathbf{C}\mathbf{v}(t_i) - \mathbf{K}\mathbf{u}(t_i) = \mathbf{s}(t_i)\mathbf{X} \tag{4-13}$$

where subscripts '*kn*' and '*un*' represent the known and unknown force, while $\mathbf{s}$ sensitivity matrix which is composed of displacement and velocity at time step t_i, which can be expressed as following equation.

$$\mathbf{s}(t_i) = -\begin{bmatrix} v^1(t_i) & v^2(t_i) & u^2(t_i) & u^1(t_i) & 0 & 0 & 0 & 0 \\ 0 & 0 & 0 & 0 & v^1(t_i) & v^2(t_i) & u^2(t_i) & u^1(t_i) \end{bmatrix} \tag{4-14}$$

The purpose of EEE methods is to minimize the equation error of the force equilibrium equation in Eq. (4-5) with respect to the unknown system parameters of the dynamic system.

$$\underset{\mathbf{X}}{\text{Min}}\, \Pi(\mathbf{X}) = \frac{1}{2} \sum_{i=1}^{nt} \left\| \mathbf{F}_{kn}(t_i) - \mathbf{F}_{un}(\mathbf{X}, t_i) \right\|_2^2 \tag{4-15}$$

In case the excitation force, the acceleration, velocity and displacement history is given *a priori*, the known force and sensitivity matrix in Eq. (4-12) and (4-14)

can be determined from the known dynamic responses and material properties. Therefore, the system parameter $\mathbf{X}$ is the only unknown and can be uniquely identified by solving Eq. (4-15).

Substitution of equation Eq. (4-13) into Eq. (4-15) leads to the following matrix form of minimization problem.

$$
\begin{aligned}
\operatorname*{Min}_{\mathbf{X}} \Pi(\mathbf{X}) &= \frac{1}{2}\sum_{i=1}^{nt}(\mathbf{F}_{kn}(t_i) - \mathbf{F}_{un}(\mathbf{X},t_i)(t_i))^{\mathrm{T}} \cdot (\mathbf{F}_{kn}(t_i) - \mathbf{F}_{un}(\mathbf{X},t_i)(t_i)) \\
&= \frac{1}{2}\mathbf{X}^{\mathrm{T}}\mathbf{S}\mathbf{X} - \mathbf{X}^{\mathrm{T}}\mathbf{G} + \frac{1}{2}\sum_{i=1}^{nt}\mathbf{F}_{kn}^{T}(t_i)\mathbf{F}_{kn}(t_i)
\end{aligned}
\tag{4-16}
$$

where $\mathbf{S}$ and $\mathbf{G}$ are global sensitivity matrix and gradient vector expressed as following equation, respectively.

$$
\mathbf{S} = \sum_{i=1}^{nt}\mathbf{s}^{\mathrm{T}}(t_i)\mathbf{s}(t_i) \ , \quad \mathbf{G} = \sum_{i=1}^{nt}\mathbf{s}^{\mathrm{T}}(t_i)\mathbf{F}_{kn}(t_i)
\tag{4-17}
$$

Since the unknown force in Eq. (4-13) is linear with respect to the system parameter, $\mathbf{X}$, the minimization problem in Eq. (4-16) forms a quadratic problem with respect to the system parameter.   Hence, the solution of Eq. (4-16) is simply obtained by solving the first-order necessary condition for the quadratic problem, which is linear algebraic equation.

$$
\frac{\partial \Pi(\mathbf{X})}{\partial \mathbf{X}} = \mathbf{S}\mathbf{X} - \mathbf{G} = 0 \rightarrow \mathbf{X} = \mathbf{S}^{-1}\mathbf{G}
\tag{4-18}
$$

As no iterative solution scheme, or complicated sensitivity analysis are required to solve the minimization problem, a unique solution is always determined by Eq. (4-18) as long as a sufficient amount of measured dynamic responses of a section model are provided.

It is customary in the SI procedures to carry out multiple measurements for a dynamic system to reduce the effect of noise in measurements on the identified system parameters. In most of the OEE methods, the system parameters are identified for each measurement independently, and then are averaged to obtain representative values. The EEE scheme is capable of identifying the system parameters with a single minimization process using all measurements obtained in each measurement together without critical consideration of the initial conditions.

The minimization problem in Eq. (4-15) is modified to accommodate data measured in each measurement within one optimization statement.

$$\underset{\mathbf{X}}{\text{Min}}\,\Pi(\mathbf{X}) = \underset{\mathbf{X}}{\text{Min}}\sum_{k=1}^{N}\Pi^{k}(\mathbf{X}) = \frac{1}{2}\sum_{k=1}^{N}\sum_{i=1}^{nt}\left\|\mathbf{F}_{kn}^{k}(t_{i}) - \mathbf{F}_{un}^{k}(\mathbf{X},t_{i})\right\|_{2}^{2} \qquad (4\text{-}18)$$

Here, N denotes the number of measurements for a structural system, and the variables with superscript k represent those for the k-th measurement. The solution of Eq. (4-18) is given as follows:

$$\mathbf{X} = (\sum_{k=1}^{N}\mathbf{S}^{k})^{-1}\sum_{k=1}^{N}\mathbf{G}^{k} \qquad (4\text{-}20)$$

4.2 Free vibration test for the flutter derivatives

Various SI algorithms have been proposed to extract the flutter derivatives form the free-vibration teat of the 2-DOF sectional model. The Ibrahim time domain (ITD) method [Ibrahim 1977] and the unifying least-square (ULS) method [Gu 2000] are representative and most widely used algorithms among them. Sarkar et al. (1992) proposed the modified ITD (MITD) method by employing an instrumental variable (IV) in the least-square process to enhance the accuracy and stability of the ITD method. Bartoli et al. (2009) also proposed the modified ULS (MULS) method by improving the solution algorithm of the ULS method. The (M)ITD method identifies the system matrix in the state-space form of the equation of motion by the complex eigenvalue analysis of the shift operator formed from the measured displacement. The (M)ULS method are based on a nonlinear optimization problem on the least square errors between the measured and the predicted displacements using the eigenvalues and eigenvectors of the system matrix of the state-space form. Both the (M)ITD and the (M)ULS methods require the complex eigenvalue analysis.

Identification schemes that utilize complete information about the state variable have been proposed for the free-vibration test. The iterative least square (ILS) method proposed by Chowdhury and Sarkar (2003) utilizes velocity and acceleration reconstructed from measured displacement using digital filters. Although the ILS method utilizes information on acceleration, the reconstruction is based on the measured displacement. Since, moreover, it requires the IV procedure with the

state-space model to minimize the relative error between calculated and measured response, the ILS is a kind of the OEE using the measured displacement.

Most of previously proposed identification schemes for free-vibration test are based on the minimization of errors between measured and calculated displacements using the state-space form of the equation of motion and requires an complex eigen-value analysis and iterative solution procedures. Moreover these methods can not be directly employed for the SI procedure of the forced-vibration test, which contains solely steady-state response.

In this chapter, the EEE method in the previous section is adopted for the SI procedure of the flutter derivatives. As the aeroelastic forces are assumed to be linear with respect to the flutter derivative, the minimization of the EEE is expressed as a quadratic problem, and thus neither iterative solution scheme nor complex eigen-value analysis is required. Because of the aforementioned linearity of the EEE, the proposed method is able to identify representative flutter derivatives corresponding to multiple measurements for a wind velocity in one optimization process. Since, moreover, both the free-vibration test and forced-vibration test are governed by the same equation; the EEE method can be employed for the forced-vibration test also.

4.2.1 Dynamic equation for the aeroelastic motion of 2-DOFs system

In this chapter, the dynamic equation for flutter derivatives and the fundamental assumption for identification of flutter derivatives from the free vibration test

are presented.   The flutter derivatives of a bridge deck are usually identified through wind tunnel tests on a section model.

An elastically supported section model with 2-DOF in the vertical (h) and the rotational (α) directions is illustrated in Fig. 4-1.   The equation of motion for the section model per unit length is defined as follows:

$$\mathbf{M}\ddot{\mathbf{U}}(t)+\mathbf{C}\dot{\mathbf{U}}(t)+\mathbf{K}\mathbf{U}(t)=\mathbf{F}_{ae}\big(\mathbf{U}(\mathbf{X},t),U(\mathbf{U},\mathbf{X},t)\big) \qquad (4\text{-}21)$$

where $\mathbf{M},\mathbf{C},\mathbf{K}$ and $\mathbf{F}_{ae}$ are the mass, damping, stiffness matrix of the structural system and the aeroelastic force vector, respectively, while $\mathbf{U}$, U and $\mathbf{X}$ are the displacement vector containing h and α, the flow field and the vector of the flutter derivatives which will be defined in next section.   The overhead dot denotes differentiation with respect to time.
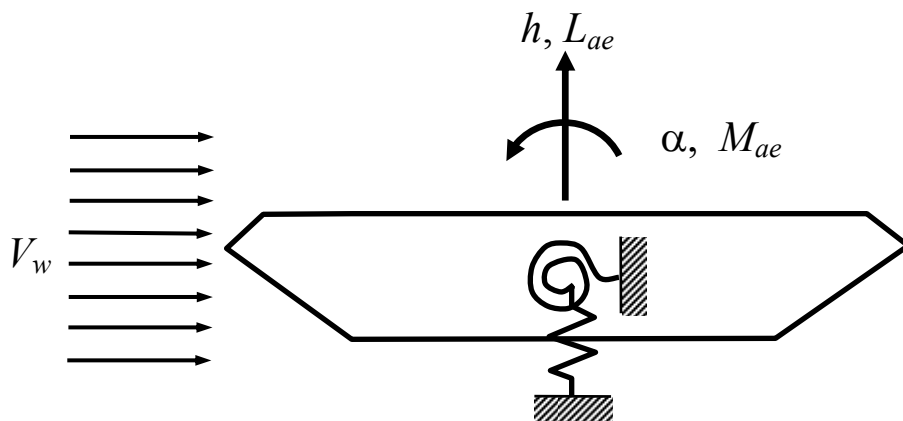
Figure 4-1. 2-DOF section model

111

The aero-dynamic force in the right side of the Eq. (4-21) acts as an outer force for the structural system, and the motion of structure recursively influence to boundary conditions of the aero-dynamic force. This moving boundary problem has several nonlinearity regard to the amplitude, the vibrational mode shape and etc. [Falco 1992, Matsumoto 1993 and Morgenthal 2000] caused by the interaction and the flutter derivatives should be determined by proper experimental procedures which can consider this nonlinear effect of the original problem.

The mechanical properties of the structural system represented by $\mathbf{M}$, $\mathbf{C}$ and $\mathbf{K}$ are generally assumed to be uncoupled. Hence, there is no off-diagonal term in the matrices and the section model behaves as separated 1 DOF systems in the vertical and rotational direction as following equation.

$$\mathbf{M} = \begin{bmatrix} m_h & \\ & m_\alpha \end{bmatrix}, \ \mathbf{C} = \begin{bmatrix} c_h & \\ & c_\alpha \end{bmatrix}, \ \mathbf{K} = \begin{bmatrix} k_h & \\ & k_\alpha \end{bmatrix} \tag{4-22}$$

The aeroelastic force acting on a sinusoidal oscillating section model in a single mode is assumed as a linear function to the motion of the section and its first order derivative [Iwamoto 1995 and Scanlan 1971]:

$$\begin{aligned} \mathbf{F}_{ae}(t) &= \begin{pmatrix} L_{ae}(t) \\ M_{ae}(t) \end{pmatrix} \approx \mathbf{C}_{ae}(\omega)\dot{\mathbf{U}}(t) + \mathbf{K}_{ae}(\omega)\mathbf{U}(t) \\ &= \begin{bmatrix} H_1(\omega) & H_2(\omega) \\ A_1(\omega) & A_2(\omega) \end{bmatrix} \begin{pmatrix} \dot{h}(t) \\ \dot{\alpha}(t) \end{pmatrix} + \begin{bmatrix} H_4(\omega) & H_3(\omega) \\ A_4(\omega) & A_3(\omega) \end{bmatrix} \begin{pmatrix} h(t) \\ \alpha(t) \end{pmatrix} \end{aligned} \tag{4-23}$$

where L_{ae} and M_{ae} are the aeroelastic lift force and moment, respectively, while ω is the circular frequency of the oscillation, and H_m and A_m ($m = 1, 2, 3, 4$) are the flutter derivatives.   It is customary to use normalized expressions of the flutter derivatives [Scanlan 1971].   For the simplicity of presentation, however, this thesis presents discussions with the un-normalized forms of the flutter derivatives.

The aeroelastic force, $\mathbf{F}_{ae}$, in Eq. (4-23) are assumed to be linear function to the displacement and velocity response, and the flutter derivatives are the function of the modal frequency.   Matsumoto et al. (1993) have tried to clarify the dependency of the flutter derivatives to the vibrational mode shape.   From their discussion, the flutter derivatives have closely related to both the modal frequency and the modal shape of the vibration especially for a bluff body.   Besides the dependency to the mode shape, the original aeroelastic system in Eq. (4-21) contains various factor of nonlinearity caused by the interaction between the structure and wind. Though the assumptions of linear and mode shape independency in Eq. (4-23) have a significance for simplicity of the identification of flutter derivatives and an analysis of the aeroelastic system.   But the experiment should be performed to consider the nonlinearity and the dependency to the modal shape.

Since the section model always vibrates in two distinct modes for the free-oscillation test, the total aeroelastic force acting on the section model is obtained by summing up the aeroelastic forces induced by each mode [Chen 2004 and Iwamoto

1995].

$$\mathbf{F}_{ae}(t) \approx \sum_{i=1}^{2} \left\{ \begin{bmatrix} H_1(\omega_i) & H_2(\omega_i) \\ A_1(\omega_i) & A_2(\omega_i) \end{bmatrix} \begin{pmatrix} \dot{h}_i(t) \\ \dot{\alpha}_i(t) \end{pmatrix} + \begin{bmatrix} H_4(\omega_i) & H_3(\omega_i) \\ A_4(\omega_i) & A_3(\omega_i) \end{bmatrix} \begin{pmatrix} h_i(t) \\ \alpha_i(t) \end{pmatrix} \right\} \quad (4\text{-}24)$$

where variables with subscript i denote those corresponding to the i-th mode, and

$h = h_1 + h_2$, $\alpha = \alpha_1 + \alpha_2$. Since sixteen flutter derivatives appear in Eq. (4-24)

for a 2-DOF system, a free-oscillation test should provide at least sixteen pieces of

information on dynamic behaviors of a section model. Unfortunately, however,

the responses of a section model measured from a free-oscillation test contain only

eight pieces of information on modal frequencies, modal damping ratios, ampli-

tudes and phases, and thus the sixteen flutter derivatives can not be uniquely de-

termined [Iwamoto 1995]. Because it is impossible to increase an amount of

information in measurements, a certain type of approximation should be introduced

to reduce the number of unknowns.

Most of previous works based on the state-space form express Eq. (4-24) in

terms of the total responses of the section model as follows:

$$\mathbf{F}_{ae}(t) \approx \begin{bmatrix} H_1 & H_2 \\ A_1 & A_2 \end{bmatrix} \begin{pmatrix} \dot{h}(t) \\ \dot{\alpha}(t) \end{pmatrix} + \begin{bmatrix} H_4 & H_3 \\ A_4 & A_3 \end{bmatrix} \begin{pmatrix} h(t) \\ \alpha(t) \end{pmatrix} \quad (4\text{-}25)$$

Eight flutter derivatives appear in Eq. (4-23), and thus are identifiable with the ILS,

(M)ITD or (M)ULS methods using measured data. Since, however, no clear defi-

nition on the frequency appearing in each flutter derivative is given in the afore-mentioned works; the frequency dependency of each flutter derivative is unidenti-fiable.

Iwamoto and Fujino (1995) and Chen and Kareem (2004) reduce the number of the flutter derivatives by eight based on an assumption that the vertical motion strongly defends on the first mode and the rotational motion is dominant to the second mode, respectively. That is, $h \approx h_1$ and $\alpha \approx \alpha_2$ because $h_2 \ll h_1$ and $\alpha_1 \ll \alpha_2$. With this assumption the aeroelastic forces are defined with eight flutter derivatives, which can be identified through a single free-oscillation test.

$$\mathbf{F}_{ae}(t) \approx \begin{bmatrix} H_1(\omega_1) & H_2(\omega_2) \\ A_1(\omega_1) & A_2(\omega_2) \end{bmatrix} \begin{pmatrix} \dot{h}(t) \\ \dot{\alpha}(t) \end{pmatrix} + \begin{bmatrix} H_4(\omega_1) & H_3(\omega_2) \\ A_4(\omega_1) & A_3(\omega_2) \end{bmatrix} \begin{pmatrix} h(t) \\ \alpha(t) \end{pmatrix} \qquad (4\text{-}26)$$

In contrast to Eq. (4-25), the dependency of each flutter derivative on the frequency is clearly defined in Eq. (4-26).

It is worthwhile to investigate the validity of the aforementioned assumption on the relative dependency. The degree of dependency in each DOF between two modes is represented by the following ratios of the fast Fourier transform (FFT) on measured displacements at the modal frequencies.

$$C_h = \frac{|F_h(\omega_2)|}{|F_h(\omega_1)|}, \quad C_\alpha = \frac{|F_\alpha(\omega_1)|}{|F_\alpha(\omega_2)|} \qquad (4\text{-}27)$$
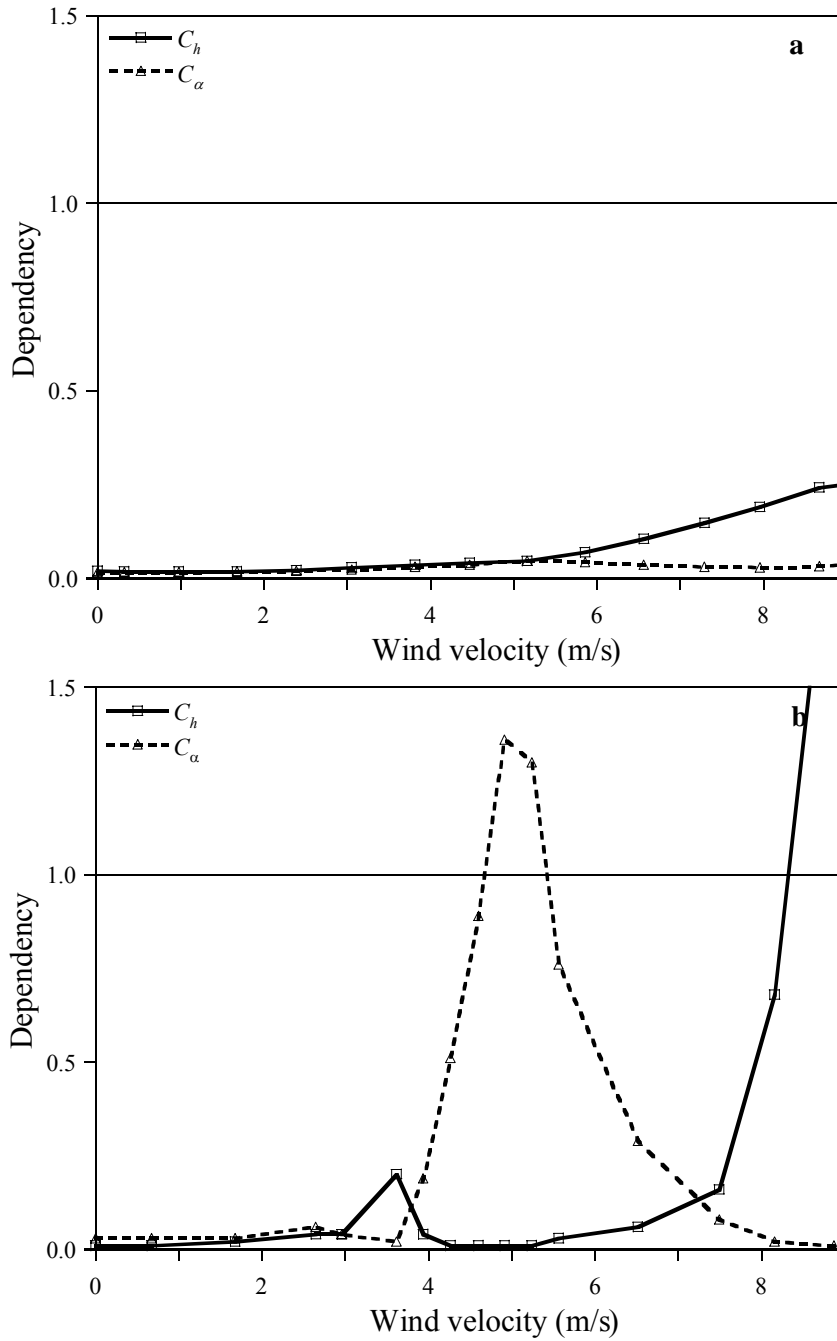
Figure 4-2. Dependency ratios of section models: (a) a thin rectangular section and
(b) a bluff H-type section

116

Here, F_h and F_α denote the FFT of measured vertical displacements and rotational angles, respectively. C_h and C_α are referred to as the vertical and the rotational dependency ratios, respectively. The ratios defined in Eq. (4-27) stay near zero if the dependency effect follows the assumption of Iwamoto and Fujino (1995), $h_2 << h_1$ and $\alpha_1 << \alpha_2$. But the motion of the section model dose not meet these conditions, the ratios significantly deviate from zero.

The two dependency ratios are drawn in Fig. 4-2 for a thin rectangular section model and a bluff H-type section model. These section models are utilized in the verification examples of this study. Both the ratios for the thin rectangular section are relatively small for all wind velocity, and thus the assumption of dominant dependency seems to be reasonable in case the motions of the thin rectangular section model. In case of the bluff H-type section model, however, the rotational dependency ratio becomes large for intermediate wind velocities, while the vertical dependency ratio increases rapidly at high wind velocities. This fact implies that the assumption is no longer appropriate for a bluff section. In case that the mechanical properties of the structural system are not diagonal, the motions of the section model have dependency to both modes even for the windless condition, and the dependency ratios seriously deviate from zero in low wind velocities. The assumption of dominant dependency is, therefore, not valid in a general sense.

This thesis proposes a new interpretation on the flutter derivatives identified from free-oscillation tests that the aeroelastic forces are expressed through eight flutter derivatives using the total responses of a section model rather than the mod-

al responses of a section:

$$
\begin{aligned}
\mathbf{F}_{ae}(t) \approx &\begin{bmatrix} \overline{H}_1(\omega_1,\omega_2) & \overline{H}_2(\omega_1,\omega_2) \\ \overline{A}_1(\omega_1,\omega_2) & \overline{A}_2(\omega_1,\omega_2) \end{bmatrix} \begin{pmatrix} \dot{h}(t) \\ \dot{\alpha}(t) \end{pmatrix} \\
&+ \begin{bmatrix} \overline{H}_4(\omega_1,\omega_2) & \overline{H}_3(\omega_1,\omega_2) \\ \overline{A}_4(\omega_1,\omega_2) & \overline{A}_3(\omega_1,\omega_2) \end{bmatrix} \begin{pmatrix} h(t) \\ \alpha(t) \end{pmatrix}
\end{aligned}
\tag{4-28}
$$

The variables with overbar in Eq. (4-28) represent flutter derivatives for the total responses of a section model. Eqs. (4-26) and (4-28) seem to be identical, but they are based on quite different concepts. Eq. (4-26) is an approximation of Eq. (4-24) with respect to the responses of a section model, while Eq. (4-28) is an approximation of the flutter derivatives defined in Eq. (4-24). As far as the derivatives themselves are concerned, of course, Eqs. (4-26) and (4-28) should yield identical results for the same measurements. Physically, however, the flutter derivatives in Eq. (4-26) are considered as functions of the individual frequency or the modal responses, and those in Eq. (4-28) should be interpreted as functions of both frequencies, i.e., the total responses. Consequently, a crucial question arises on the similitude law to be applied for the analysis of a real bridge deck corresponding to the section model. The assumption for Eq. (4-26) is not valid for all cases, but it is easy to apply a frequency-based similitude law as it is a modal response-based approximation. It is believed that further investigations should be followed on the physical significance of the flutter derivatives identified from free-oscillation tests.

4.1.2 Identification of flutter derivatives from the free vibration test based on the EEE

In case the complete time history of displacement, velocity and acceleration are available, the flutter derivatives are identified by employing the EEE proposed in section 4.1 as follows:

$$
\begin{aligned}
\operatorname*{Min}_{\mathbf{X}} \Pi(\mathbf{X}) &= \frac{1}{2} \sum_{i=1}^{nt} \left\| \mathbf{F}_{kn}(t_i) - \mathbf{F}_{un}(\mathbf{X}, t_i) \right\|_2^2 \\
&= \frac{1}{2} \sum_{i=1}^{nt} \left\| \mathbf{F}_{st}(t_i) - \mathbf{F}_{ae}(\mathbf{X}, t_i) \right\|_2^2
\end{aligned}
\tag{4-29}
$$

here, $\mathbf{X}$ is the vector of the flutter derivatives to be identified.

$$
\mathbf{X} = (\overline{H}_1 \quad \overline{H}_2 \quad \overline{H}_3 \quad \overline{H}_4 \quad \overline{A}_1 \quad \overline{A}_2 \quad \overline{A}_3 \quad \overline{A}_4)^T
\tag{4-30}
$$

$\mathbf{F}_{st}(t_i)$ and $\mathbf{F}_{ae}(\mathbf{X}, t_i)$ are the structural resistance force and the aeroelastic force at time t_i, respectively.

$$
\mathbf{F}_{st}(t_i) = \mathbf{M}\ddot{\mathbf{U}}(t_i) + \mathbf{C}\dot{\mathbf{U}}(t_i) + \mathbf{K}\mathbf{U}(t_i)
\tag{4-31}
$$

The aeroelastic force given in (4-28) is rewritten in terms of the vector of the flutter derivatives.

$$\mathbf{F}_{ae}(\mathbf{X},t_i) = \mathbf{s}(t_i)\mathbf{X}$$

$$= \begin{bmatrix} \dot{h}(t_i) & \dot{\alpha}(t_i) & \alpha(t_i) & h(t_i) & 0 & 0 & 0 & 0 \\ 0 & 0 & 0 & 0 & \dot{h}(t_i) & \dot{\alpha}(t_i) & \alpha(t_i) & h(t_i) \end{bmatrix}\mathbf{X} \qquad (4\text{-}32)$$

Following the solution procedure of the EEE method in Eq. (4-16) ~ Eq. (4-18), a unique solution is always determined by Eq. (4-18) as long as a sufficient amount of measured dynamic responses of a section model are provided.

It is customary in wind tunnel tests to carry out multiple measurements for a wind velocity to reduce the effect of noise in measurements on the identified flutter derivatives. In most of the previously proposed schemes the flutter derivatives are identified for each measurement independently, and then are averaged to obtain representative values. The EEE is capable of identifying the flutter derivatives with a single minimization process using all measurements obtained in each measurement together as defined in Eq. (4-18). Li et al. (2003) proposed a similar approach for the calculation of complex eigenvalues in the ULS method, but the corresponding eigenvectors are evaluated for an individual measurement and the representative eigenvectors are obtained by averaging them.

Complete dynamic responses, *i.e.*, displacement, velocity and acceleration, should be measured simultaneously to identify the flutter derivatives based on the EEE. Although displacement and acceleration may be measured together in wind tunnel tests, it is troublesome to install several different types of transducers on the same locations of a section model. Furthermore, direct measurement of velocity is almost impossible due to the very limited availability of transducers. To cir-

cumvent the difficulty in the complete measurement of the dynamic responses, this study utilizes reconstructed displacement and velocity from measured acceleration by the FFIR filter, which is presented in the chapter 3.

As pointed out by Bartoli et al. (2009), extraction schemes that use variables reconstructed by digital filters suffer from the loss of measured data, which may lead to inaccurate or unstable identification of the flutter derivatives especially for high wind velocities.   This drawback can be overcome in the proposed scheme by the simultaneous use of data measured from each measurement as formulated in Eq. (4-18) because the accuracy and stability of the identification are quickly improved as the amount of data used in the estimation increases.

The FFIR filter in the section 3.1.3 is employed to reconstruct displacement and velocity simultaneously from the measured acceleration.   As discussed in the section 3.1.3, the FFIR filter is capable of reconstructing displacement and velocity components for the frequency range between the target frequency and 10% of the sampling frequency, $f_T \le f \le 0.1 f_s$, within a 3% error for $\alpha_T = 0.97$.

Therefore, the sampling frequency of measurement should be larger than the highest frequency of interest at least by 10 times, which is easily achieved with modern accelerometers and A/D converters.

Since the FFIR filter is a finite and discrete filter, the Gibbs phenomenon, which is the rippling characteristics of a truncated Fourier series, is inevitably observed in the accuracy function of the FEM-FIR filter.
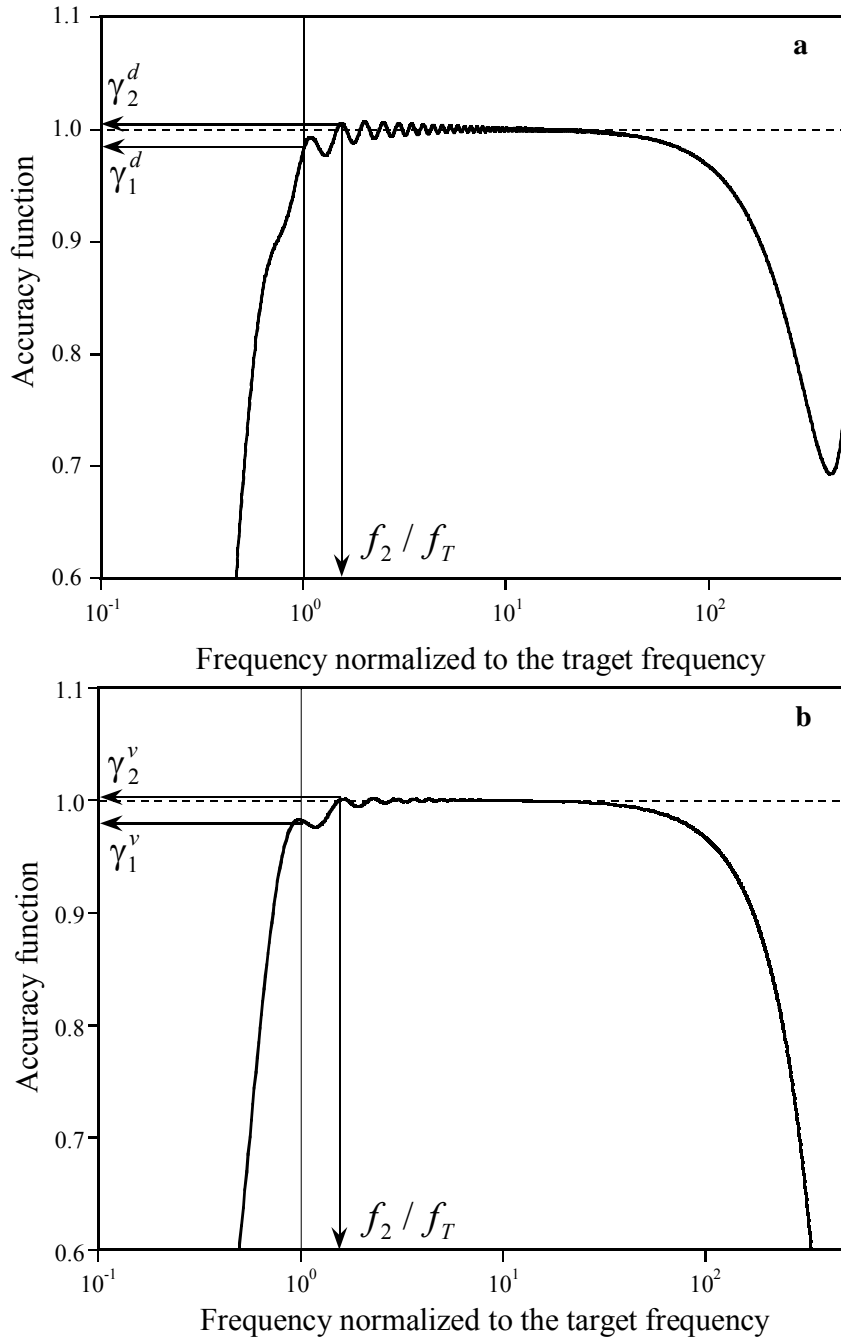
Figure 4-3. Typical accuracy functions of the FEM-FIR filter and the definitions of correction factors: (a) Displacement and (b) Velocity

By virtue of the accuracy functions of the FFIR filter, errors in reconstructed displacement and velocity are easily estimated. The typical accuracy functions of displacement and velocity are drawn in Fig. 4-3. Assuming that the reconstructed errors in the vertical and rotational motion are mainly caused by the errors in the first and second mode, respectively, the reconstructed responses are modified to compensate the errors in the FEM-FIR filter for more accurate extraction of the flutter derivatives as follows:

$$\left(\frac{\dot{h}_r(t_i)}{\gamma_1^v} \quad \frac{\dot{\alpha}_r(t_i)}{\gamma_2^v} \quad \frac{\alpha_r(t_i)}{\gamma_2^d} \quad \frac{h_r(t_i)}{\gamma_1^d} \right) \tag{4-33}$$

where subscript r indicates the reconstructed responses, while correction factors, γ_i^d and γ_i^v, are the values of the accuracy functions for the displacement and velocity at the i-th mode, respectively, as shown in Fig. 4-3.

4.3 Forced vibration test for the flutter derivatives

Dissimilar to the free vibration test, the forced vibration test includes the external forcing term in the equation of motion as flowing equation.

$$\mathbf{M}\ddot{\mathbf{U}}(t) + \mathbf{C}\dot{\mathbf{U}}(t) + \mathbf{K}\mathbf{U}(t) = \mathbf{F}_{ae}(t) + \mathbf{F}_{ex}(t) \tag{4-34}$$

where $\mathbf{F}_{ex}$ is external force. Note that the external force is the reaction force in the displacement controlled test, which should be measured for the identification.

Substitution of the matrix form of aero-elastic force in Eq. (4-23) to Eq. (4-34) yields following form of equation of motion with excitation force.

$$\mathbf{M}\ddot{\mathbf{U}}(t) + \mathbf{C}_{eff}\dot{\mathbf{U}}(t) + \mathbf{K}_{eff}\mathbf{U}(t) = \mathbf{F}_{ex}(t) \tag{4-35}$$

where $\mathbf{C}_{eff}$ and $\mathbf{K}_{eff}$ are effective damping and stiffness matrixes of aero-elastic system as follows.

$$\mathbf{C}_{eff} = \mathbf{C} - \mathbf{C}_{ae}, \quad \mathbf{K}_{eff} = \mathbf{K} - \mathbf{K}_{ae} \tag{4-36}$$

Since the 2-DOF section model is excited to damp out the transient response and the only steady-state response in a single frequency is adopted for the identification procedure in the forced-vibration test, the flutter derivatives in Eq. (4-36) imply the linear force weighting corresponding to the single excitation frequency and is appropriate for the conventional law of similitude which is discussed in the previous section.

4.3.1 Forced vibration test controlled by prescribed displacement

The displacement controlled forced vibration test is implemented by imposing the predefined sinusoidal displacement to the section model without the elastic suspension of springs.

$$\mathbf{U}(t) = \begin{pmatrix} h_0 \\ \alpha_0 \end{pmatrix} \sin(\omega_{ex} t) \qquad (4\text{-}37)$$

where ω_{ex} is the angular frequency of the excitation motion.

The absence of spring makes the mechanical damping and stiffness matrix in Eq. (4-19) zero, and the effective damping and stiffness matrix only contain aeroelastic terms as following equation.

$$\mathbf{C}_{eff} = -\mathbf{C}_{ae}, \qquad \mathbf{K}_{eff} = -\mathbf{K}_{ae} \qquad (4\text{-}38)$$

After the transient component damped out, the reaction in Eq. (4-34) also yields to sinusoidal motion.

$$\mathbf{F}_{ex}(t) = \begin{pmatrix} \overline{L}_s \\ \overline{M}_s \end{pmatrix} \sin(\omega_{ex} t) + \begin{pmatrix} \overline{L}_c \\ \overline{M}_c \end{pmatrix} \cos(\omega_{ex} t) \qquad (4\text{-}39)$$

where $\overline{L}_s$, $\overline{L}_c$, $\overline{M}_s$ and $\overline{M}_c$ are the measured amplitudes of sinusoidal reaction. Because the aero-elastic system has both amplitude and phase response in the transfer function, the reaction in Eq. (4-39) should contain not only sine term

but also cosine term.

Substitution of Eq. (4-37) and Eq. (4-39) to Eq. (4-35) yields following algebraic equations.

$$\begin{pmatrix} \overline{L}_s \\ \overline{M}_s \end{pmatrix} = \left[-\omega_{ex}^2 \mathbf{M} + \mathbf{K}_{eff} \right] \begin{pmatrix} h_0 \\ \alpha_0 \end{pmatrix}, \quad \begin{pmatrix} \overline{L}_c \\ \overline{M}_c \end{pmatrix} = \omega_{ex} \mathbf{C}_{eff} \begin{pmatrix} h_0 \\ \alpha_0 \end{pmatrix} \qquad (4\text{-}40)$$

Since only four algebraic relations given in Eq. (4-40) but there is eight unknown flutter derivatives, the solution of the equation can not be determined from a single experimental test.   To acquire sufficient information for eight unknowns, at least two separated experiments with the independent excitation conditions should be tested.

$$\begin{pmatrix} \overline{L}_{s,1} \\ \overline{M}_{s,1} \end{pmatrix} = \left[-\omega_{ex}^2 \mathbf{M} + \mathbf{K}_{eff} \right] \begin{pmatrix} h_{0,1} \\ \alpha_{0,1} \end{pmatrix}, \quad \begin{pmatrix} \overline{L}_{c,1} \\ \overline{M}_{c,1} \end{pmatrix} = \omega_{ex} \mathbf{C}_{eff} \begin{pmatrix} h_{0,1} \\ \alpha_{0,1} \end{pmatrix}$$

$$\begin{pmatrix} \overline{L}_{s,2} \\ \overline{M}_{s,2} \end{pmatrix} = \left[-\omega_{ex}^2 \mathbf{M} + \mathbf{K}_{eff} \right] \begin{pmatrix} h_{0,2} \\ \alpha_{0,2} \end{pmatrix}, \quad \begin{pmatrix} \overline{L}_{c,2} \\ \overline{M}_{c,2} \end{pmatrix} = \omega_{ex} \mathbf{C}_{eff} \begin{pmatrix} h_{0,2} \\ \alpha_{0,2} \end{pmatrix} \qquad (4\text{-}41)$$

where the additional subscript '1' and '2' denote the number of test.   If the amplitudes of reaction in Eq. (4-41) are exactly given for the two tests, the flutter derivatives can be identified by solving the simultaneous equation in Eq. (4-41).

Since the displacement is predefined as Eq. (4-37) in the displacement controlled forced vibration test, the velocity and the acceleration also can be calculated by the definition and regarded as the measured responses; hence the displacement

control test supply full-measurement condition in both state and space. The concept of SI in equation (4-41) exactly matches with the concept of the EEE for the multiple trials in Eq. (4-18) except that the least squared scheme is employed in the EEE procedure.

The measured amplitude for the reaction, $\overline{L}_s$, $\overline{L}_c$, $\overline{M}_s$ and $\overline{M}_c$, are not free from various sources of noise, the direct solution of Eq. (4-41) yields erroneous results as the fundamental property of the inverse problem. Moreover best-fit curves in sinusoidal form should be calculated for each excitation. The optimization method using the EEE can be directly employed to yield accurate and reliable results without any additional calculations.

$$\underset{\mathbf{X}}{\text{Min}}\,\Pi(\mathbf{X}) = \underset{\mathbf{X}}{\text{Min}} \sum_{k=1}^{2} \Pi^{k}(\mathbf{X}) = \frac{1}{2} \sum_{k=1}^{2} \sum_{i=1}^{nt} \left\| \mathbf{F}_{st}^{k}(t_i) - \mathbf{F}_{ae}^{k}(\mathbf{X},t_i) \right\|_{2}^{2} \qquad (4\text{-}42)$$

Here, the structural resistance force includes the measured reaction force as following equation:

$$\mathbf{F}_{st}(t_i) = \mathbf{M}\ddot{\mathbf{U}}(t_i) + \mathbf{C}\dot{\mathbf{U}}(t_i) + \mathbf{K}\mathbf{U}(t_i) - \mathbf{F}_{ex}(t_i) \qquad (4\text{-}43)$$

By the virtue of the selection of the conventional displacement set as following equation, Eq. (4-41) is represented by separated eight equations, in which contains just one unknown respectively.

$$\mathbf{U}_1(t) = \begin{pmatrix} h_{0,1} \\ 0 \end{pmatrix} \sin(\omega_{ex} t), \quad \mathbf{U}_2(t) = \begin{pmatrix} 0 \\ \alpha_{0,2} \end{pmatrix} \sin(\omega_{ex} t) \qquad (4\text{-}44)$$

Substituting Eq. (4-44) to Eq. (4-41), the flutter derivatives are acquired as follows:

$$\begin{pmatrix} H_1(\omega_{ex}) \\ A_1(\omega_{ex}) \\ H_4(\omega_{ex}) \\ A_4(\omega_{ex}) \end{pmatrix} = - \begin{pmatrix} \bar{L}_{c,1} / \omega_{ex} h_{0,1} \\ \bar{M}_{c,1} / \omega_{ex} h_{0,1} \\ \bar{L}_{s,1} / h_{0,1} + \omega_{ex}^2 m_h \\ \bar{M}_{s,1} / h_{0,1} \end{pmatrix} \qquad (4\text{-}45\text{-}a)$$

$$\begin{pmatrix} H_2(\omega_{ex}) \\ A_2(\omega_{ex}) \\ H_3(\omega_{ex}) \\ A_3(\omega_{ex}) \end{pmatrix} = - \begin{pmatrix} \bar{L}_{s,2} / \omega_{ex} \alpha_{0,2} \\ \bar{M}_{s,2} / \omega_{ex} \alpha_{0,2} \\ \bar{L}_{s,2} / \alpha_{0,2} \\ \bar{M}_{s,2} / \alpha_{0,2} + \omega_{ex}^2 m_\alpha \end{pmatrix} \qquad (4\text{-}45\text{-}b)$$

The displacement set in Eq. (4-44) is conventionally used to extract the flutter derivatives for the convenience of experimental implementation and the simplicity of identification procedure.   Since it is insufficient set to investigate the dependency of the flutter derivatives to the vibrational mode shape, the EEE method with the arbitrary displacement set in Eq (4-41) can be more generally employed for the identification.

Though the displacement control method in this section can successively identify the flutter derivatives from the experimental responses, but it divides the original problem in Eq. (4-21) into separated structural system and aero-dynamic

system by imposing the prescribed boundary condition, then author believe that this experimental procedure can not fully implement nonlinearity caused by the interaction of the original aeroelastic system.

4.3.2 Forced vibration test controlled by prescribed excitation force

The overall procedure of the force control test is very similar to the displacement control except a change of displacement from input to output, but the force-control test does not restrict the motion itself, the nonlinearity caused by the interaction can be fully considered in this method.   The force controlled forced vibration test is implemented by imposing the prescribed sinusoidal excitation force to the section model supported by the elastic springs.

$$\mathbf{F}_{ex}(t) = \begin{pmatrix} L_{ex}(t) \\ M_{ex}(t) \end{pmatrix} = \begin{pmatrix} L_0 \\ M_0 \end{pmatrix} \sin \omega_{ex} t \qquad (4\text{-}46)$$

The excitation force in Eq. (4-46) can be implemented by the four rotating mass subjected to the guide frame as Fig 4-4.
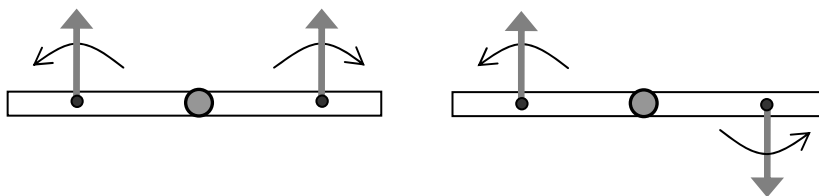
Figure 4-4. Conceptual figure for the force controlled vibration test

The analytic solution for the forced vibration test in the steady-state response is presented by Jung et al. (2011). The steady-state response to the force control test, which means the particular solution to the excitation forces of Eq. (4-35), is obtained by getting the particular solution of equation of motion in Eq. (4-35).

$$\mathbf{U}(t) = \begin{pmatrix} h_s \\ \alpha_s \end{pmatrix} \sin(\omega_{ex} t) + \begin{pmatrix} h_c \\ \alpha_c \end{pmatrix} \cos(\omega_{ex} t) \tag{4-47}$$

Substitution of Eq. (4-46) and Eq. (4-47) to Eq. (4-35) yields following equations.

$$\begin{aligned} \begin{pmatrix} h_c \\ \alpha_c \end{pmatrix} &= -\left[\left(-\omega_{ex}^2 \mathbf{M} + \mathbf{K}_{eff} \right) \left(\omega_{ex}^{-1} \mathbf{C}_{eff}^{-1} \right) \left(-\omega_{ex}^2 \mathbf{M} + \mathbf{K}_{eff} \right) + \left(\omega_{ex} \mathbf{C}_{eff} \right) \right]^{-1} \begin{pmatrix} L_0 \\ M_0 \end{pmatrix} \\ \begin{pmatrix} h_s \\ \alpha_s \end{pmatrix} &= \left[\left(-\omega_{ex}^2 \mathbf{M} + \mathbf{K}_{eff} \right) + \omega_{ex} \mathbf{C}_{eff} \left(-\omega_{ex}^2 \mathbf{M} + \mathbf{K}_{eff} \right)^{-1} \omega_{ex} \mathbf{C}_{eff} \right]^{-1} \begin{pmatrix} L_0 \\ M_0 \end{pmatrix} \end{aligned} \tag{4-48}$$

As like to the displacement control test, the flutter derivatives can not be determined from a single experimental test in Eq. (4-48) for the limited information. To acquire sufficient information for eight unknowns, at least two separated experiments with the independent excitation conditions should be tested and be treated in a single optimization process. Unlike to the displacement control test, however, the full-measurement in state is impossible unless the help of the reconstruction scheme and should be solved by the SI methods based on the OEE. Since the analytic solution for the force control test in Eq. (4-48) is nonlinear function with

respect to the unknown flutter derivative but contains several matrix inversions, the sensitivity analysis for the OEE yields severely complex problem.

By the virtue of the FFIR filter, from two or more tests with different independent excitation forces, the flutter derivatives can be identified by employing the proposed EEE method in Eq. (4-42) and Eq. (4-43) with simplicity of the quadratic problems.

4.4 Numerical and Experimental Verification for the EEE method

As commented in the previous section, the forced-vibration tests are not implemented in the Seoul National University yet. Hence, the experimental verification is confined to the free-vibration test.

For the verification of the proposed method for the free-vibration test, the flutter derivatives are identified using measurements taken from a series of free-oscillation tests for the two types of representative sections of bridge decks; a thin rectangular plate with the width-to-depth (B/D) ratio of 20 and a bluff H-type section. Fig. 4 shows the dimensions of the sections. A series of push-back and sudden release tests were repeated with the change of wind velocity. Four accelerometers as well as four noncontact displacement transducers were installed to measure 2-DOF motions of the section models. The reconstruction of the displacement and velocity is carried out by employing the FFIR filter and all the reconstructed responses are modified with the correction factors in Eq. (4-33). The instant when the actual reconstruction begins is set to $t = 0$ throughout the examples.

The flutter derivatives are identified by the proposed method using the measured accelerations and by the MITD method using the measured displacements for comparison. The identified results from both of the methods presented here are the representative values for multiple measurements. The flutter derivatives identified for each measurement are averaged for the MITD method, while multiple measurements are considered together in optimization for the proposed method.

133

a

1.5 cm

30.0 cm

b

Barrier: 0.5 cm $\times$ 1.8 cm, 0.8 cm from edge

3.0 cm

46.0 cm
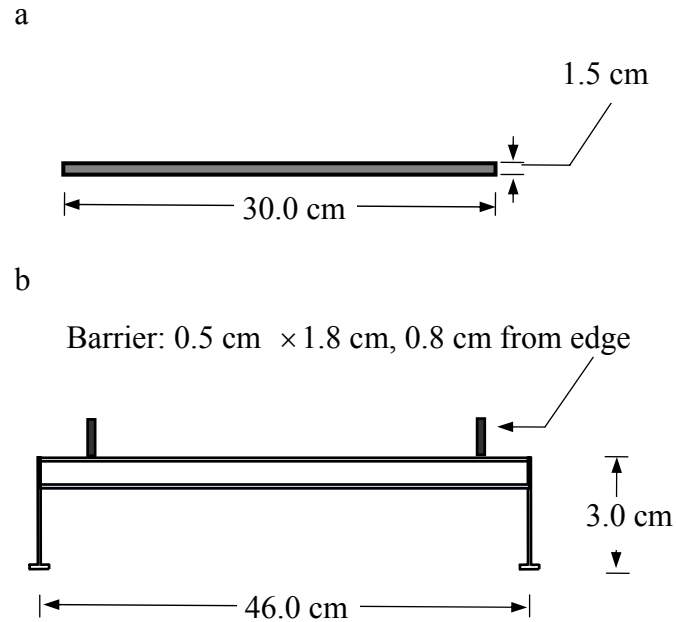
Figure 4-5. Dimension of cross-section considered: (a) a thin rectangular section (b) a bluff H-type section

The initial conditions required in the MITD method are taken from the reconstructed displacement and velocity time histories. As recommended by Sarkar et al. (1994), the nearest integer smaller than the ratio of $1/(4\Delta t f_d)$ is used for the first shift coefficient, N_1, and the second shift coefficient N_2 is set to the same value as N_1. Here, Δt and f_d denote the time increment and highest modal frequency, respectively.

To present the identified flutter derivatives as functions of the reduced wind velocity in a conventional fashion, the following normalization is applied to the flutter derivatives defined in Eq. (4-26).

134

$$
\begin{bmatrix} H_1^*(\widetilde{V}_1) & H_2^*(\widetilde{V}_2) \\ A_1^*(\widetilde{V}_1) & A_2^*(\widetilde{V}_2) \end{bmatrix} = \frac{2}{\rho B^2} \begin{bmatrix} \dfrac{1}{\omega_1}\overline{H}_1(\omega_1,\omega_2) & \dfrac{1}{B\omega_2}\overline{H}_2(\omega_1,\omega_2) \\ \dfrac{1}{B\omega_1}\overline{A}_1(\omega_1,\omega_2) & \dfrac{1}{B^2\omega_2}\overline{A}_2(\omega_1,\omega_2) \end{bmatrix}
$$

$$
\begin{bmatrix} H_4^*(\widetilde{V}_1) & H_3^*(\widetilde{V}_2) \\ A_4^*(\widetilde{V}_1) & A_3^*(\widetilde{V}_2) \end{bmatrix} = \frac{2}{\rho B^2} \begin{bmatrix} \dfrac{1}{\omega_1^2}\overline{H}_4(\omega_1,\omega_2) & \dfrac{1}{B\omega_2^2}\overline{H}_3(\omega_1,\omega_2) \\ \dfrac{1}{B\omega_1^2}\overline{A}_4(\omega_1,\omega_2) & \dfrac{1}{B^2\omega_2^2}\overline{A}_3(\omega_1,\omega_2) \end{bmatrix}
$$

(4-49)

$$
\widetilde{V}_m = \frac{V_w}{B(\omega_m/2\pi)}, \quad m = 1,\,2 \tag{4-50}
$$

where H_i^* and A_i^* $(i=1\sim4)$ are the normalized flutter derivatives, V_w is the actual wind velocity, $\widetilde{V}_m$ is the reduced wind velocity, ρ is the air density and B is the width of section model.

4.4.1 Free-vibration test of a thin rectangular section of B/D=20 – case of a stream-lined section

The wind-tunnel tests for this example are preformed in the wind tunnel of Mokpo National University, Mokpo, Korea. Fig. 4-6 shows the experimental set-ups for this example. The transverse movement is restrained with piano wires to simulate 2-DOF motions. A 2-DOF free oscillation is introduced to the model by suddenly releasing two pneumatic pistons that push the section to induce initial displacements of 2cm in the vertical direction and 0.05 radians in the rotational

direction.   The free-oscillation test was performed for 20 wind velocities at an almost equal interval from 0 m/sec to 12.8 m/sec and repeated 10 times consecutively for each wind velocity.   Standard time duration for the identification is set to 10 sec.   In case one of the 2-DOF responses is damped out before 10 sec, measurements taken up to the instant when one of the responses disappears is utilized.   The shortest time duration of 1.31 sec is adopted at the maximum wind velocity of 12.8m/s.

The two dominant frequencies identified at each wind velocity through the FFT of the measured accelerations are shown in Fig. 4-7.   The lower frequencies, which correspond to the 1st modal frequency, are adopted as the target frequencies of the FEM-FIR filter for the reconstruction of displacements and velocities.
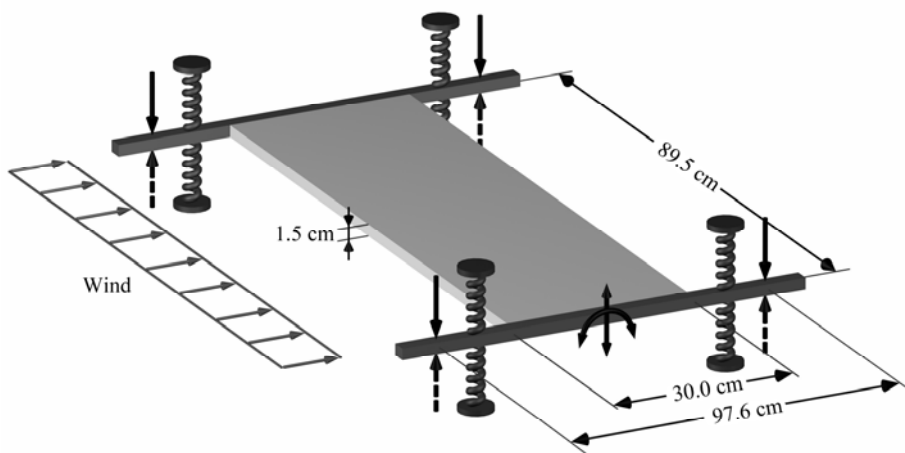
Mass per unit length: 4.69 (kg/m)
Mass moment of inertia per unit length: 0.14 (kg-m^2/m)
Air density: 1.25 (kg/ m^3)
Figure 4-6. Experimental setup for the thin rectangular section

136
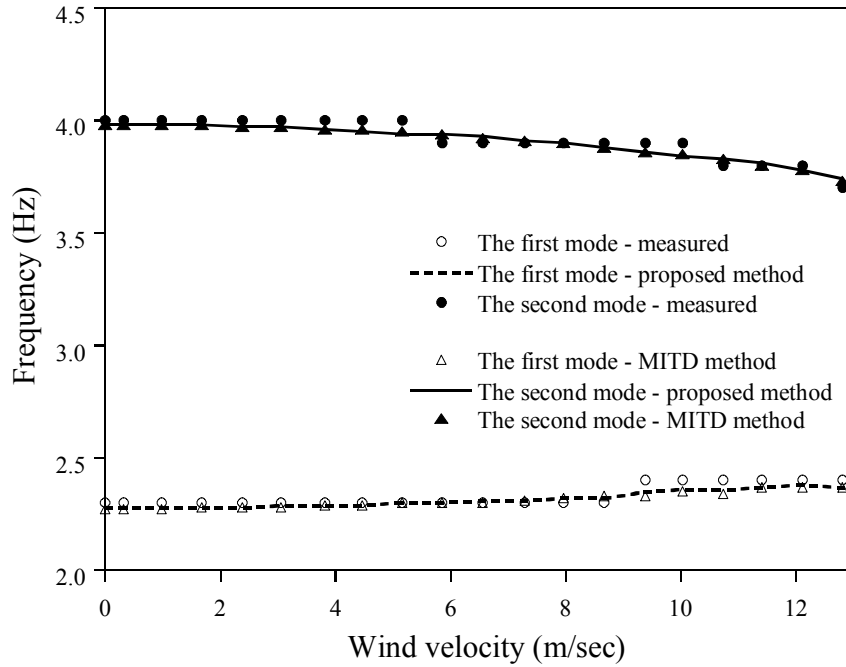
Figure 4-7. Two dominant frequencies of the thin rectangular section
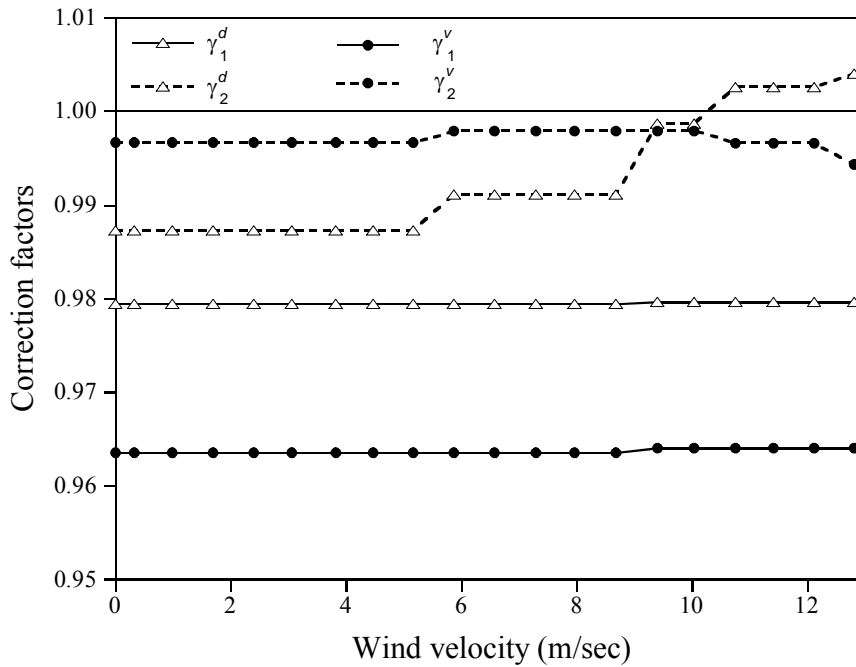
Figure 4-8. Correction factors applied for the thin rectangular section
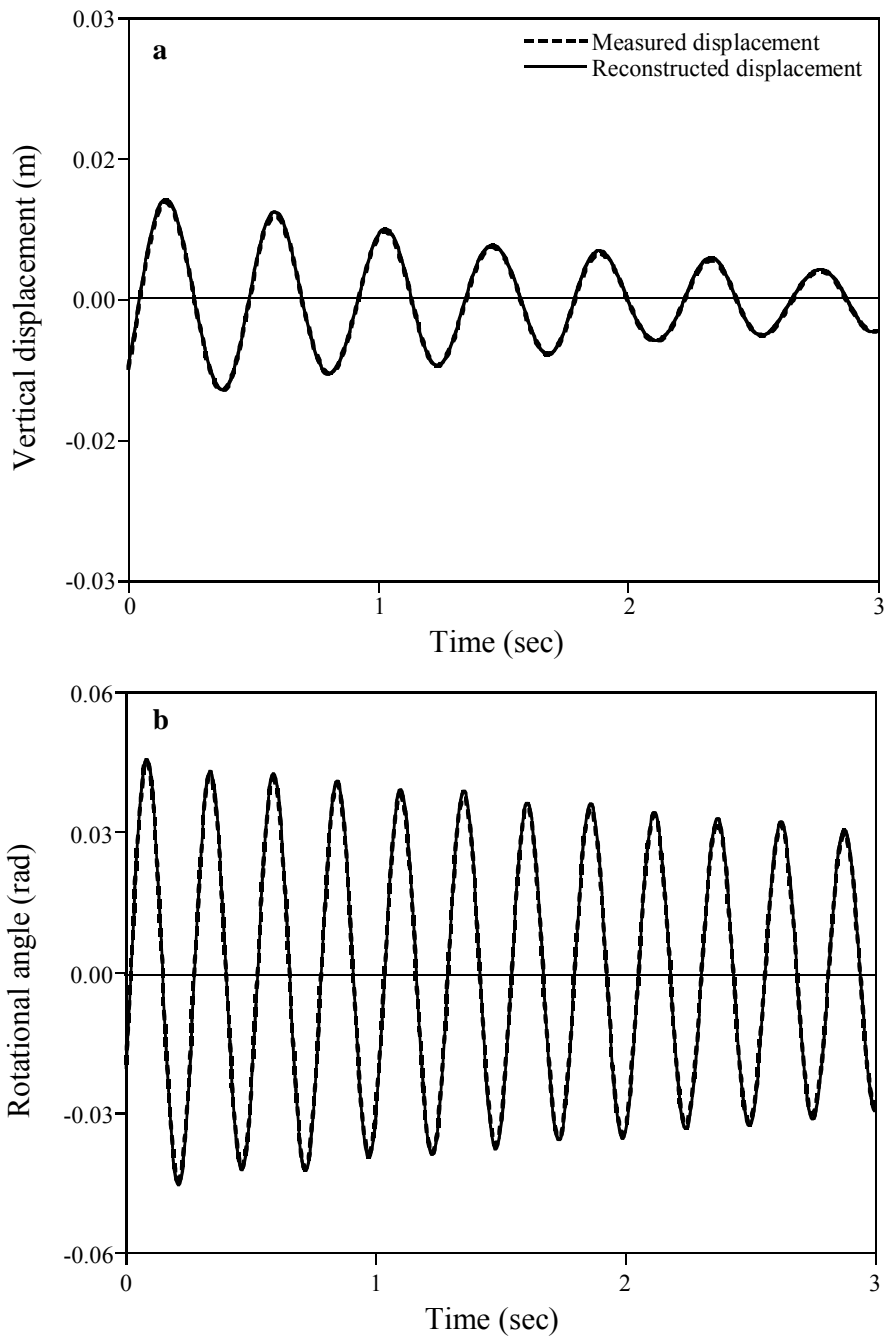
Figure 4-9. Measured and reconstructed displacements at the wind velocity of 5.86m/s for the thin rectangular section: (a) vertical displacement and (b) rotational angle

The correction factors of reconstructed responses determined for each wind velocity are given in Fig. 4-8. The reconstructed displacements of the section at the wind velocity of 5.86m/s are compared with the measured displacements in Fig. 4-9. The two displacements appear almost identical in the figure, and the reconstructed responses for the other wind velocities maintain the same levels of accuracy as shown in Fig. 8. The mechanical frequencies and the damping ratios of the model are identified as f_1=2.72Hz, f_2=3.98Hz, ξ_1=0.274% and ξ_2=0.124% using the reconstructed displacements for the windless condition.
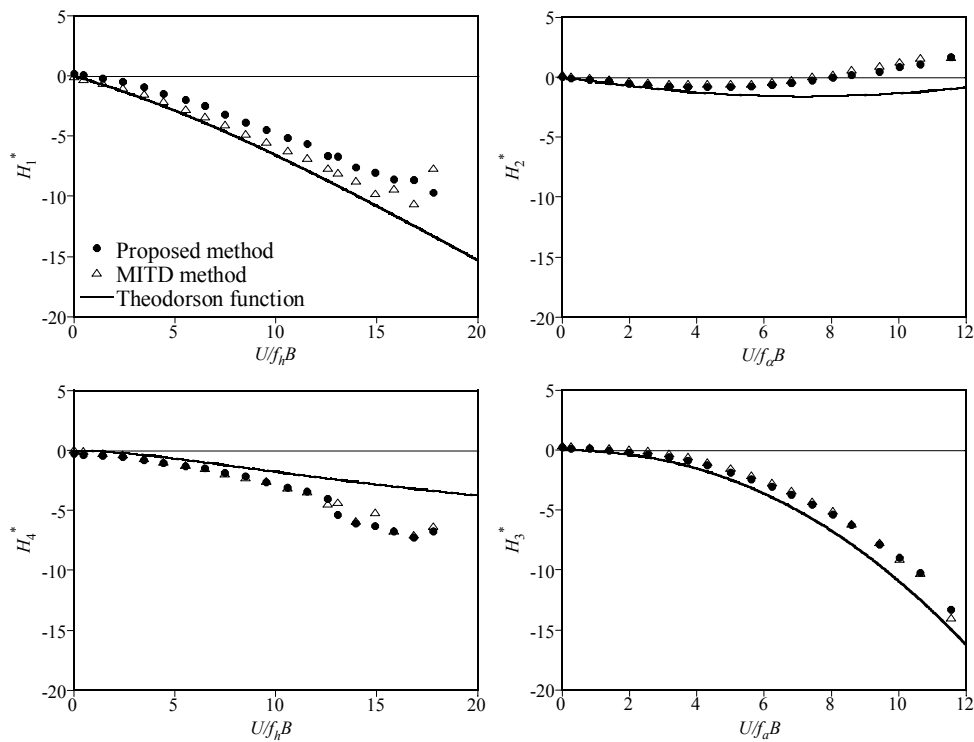
Figure 4-10. Identified flutter derivatives for the thin rectangular section - H^* components: (a) H_1^*, (b) H_2^*, (c) H_4^* and (d) H_3^*

139
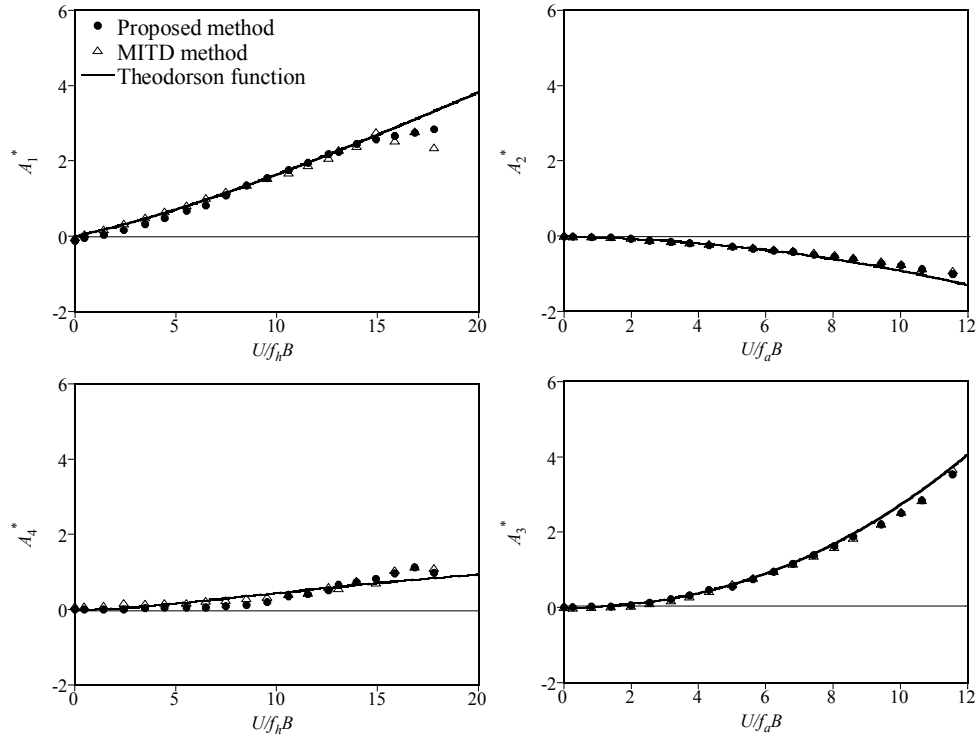
Figure 4-11. Identified flutter derivatives for the thin rectangular section - A^* components: (a) A_1^*, (b) A_2^*, (c) A_4^* and (d) A_3^*

Figs. 4-10 and 4-11 show the flutter derivatives for the lift force and moment, respectively, identified by the proposed and MITD method as well as predicted by the Theodorsen function for an ideally thin plate. The H_4^* and A_3^* components by the Theodorsen function in the figures do not include added mass terms (Scanlan and Tomko, 1971), because their contributions to the identified results are eliminated in the identification process. The proposed method yields well-matched results compared to the MITD method for all eight of the flutter deriva-

tives in an overall sense even though slight differences in the H_1^* component are found between the two methods.   As the identification of the flutter derivatives is a type of ill-posed inverse problem, the results may depend on numerical schemes to some extent (Scanlan and Tomko, 1971), and the differences seem to be within an acceptable range.   The A_i^* components by both the proposed method and the MITD method are almost identical to those predicted by the Theodorsen function.

As compared to the A_i^* components, the H_i^* components identified by both the proposed and MITD method, somewhat deviate from the theoretical values predicted by the Theodorsen function.   This kind of phenomenon also has been reported by Scanlan and Tomko (1971).
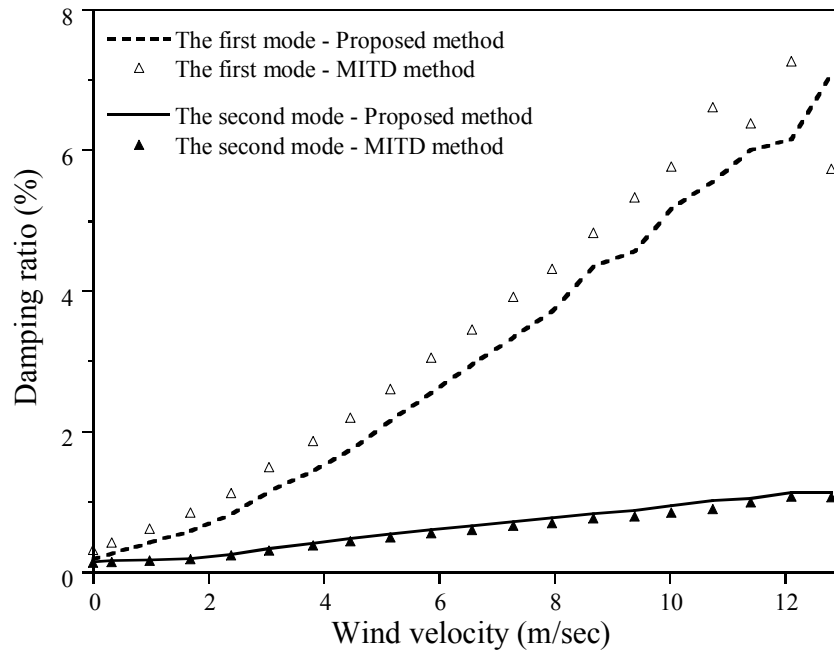
Figure 4-12. Identified damping ratios for the thin rectangular section

The frequencies and the damping ratios of the section are calculated through the complex eigenvalue analysis of Eq. (4-1) with the identified flutter derivatives, and are presented in Fig. 4-7 and Fig. 4-12, respectively. The calculated frequencies show good agreements with those identified by the FFT of the measured accelerations. The MITD method yields slightly larger damping ratios for the 1st mode and a smaller damping ratio for the 2nd mode than the proposed method.

As the last step of the verification, the displacement time history is calculated by solving Eq. (4-1) in the time domain with the Newmark's method. The average acceleration assumption and the time increment of 0.001 sec are utilized for the numerical integration. The initial conditions are taken from the reconstructed displacement and velocity. Fig. 4-13 compares the measured displacements with the calculated ones for a wind velocity of 5.86 m/sec. Virtually no phase error is found in either the vertical displacement or rotational angle. The amplitude of the calculated rotational angle is almost identical to the measurement. However, the flutter derivatives identified by the proposed method result in slightly larger amplitude in the vertical displacement than in the measurement. It seems that the proposed method somewhat underestimates the damping for the vertical motion.
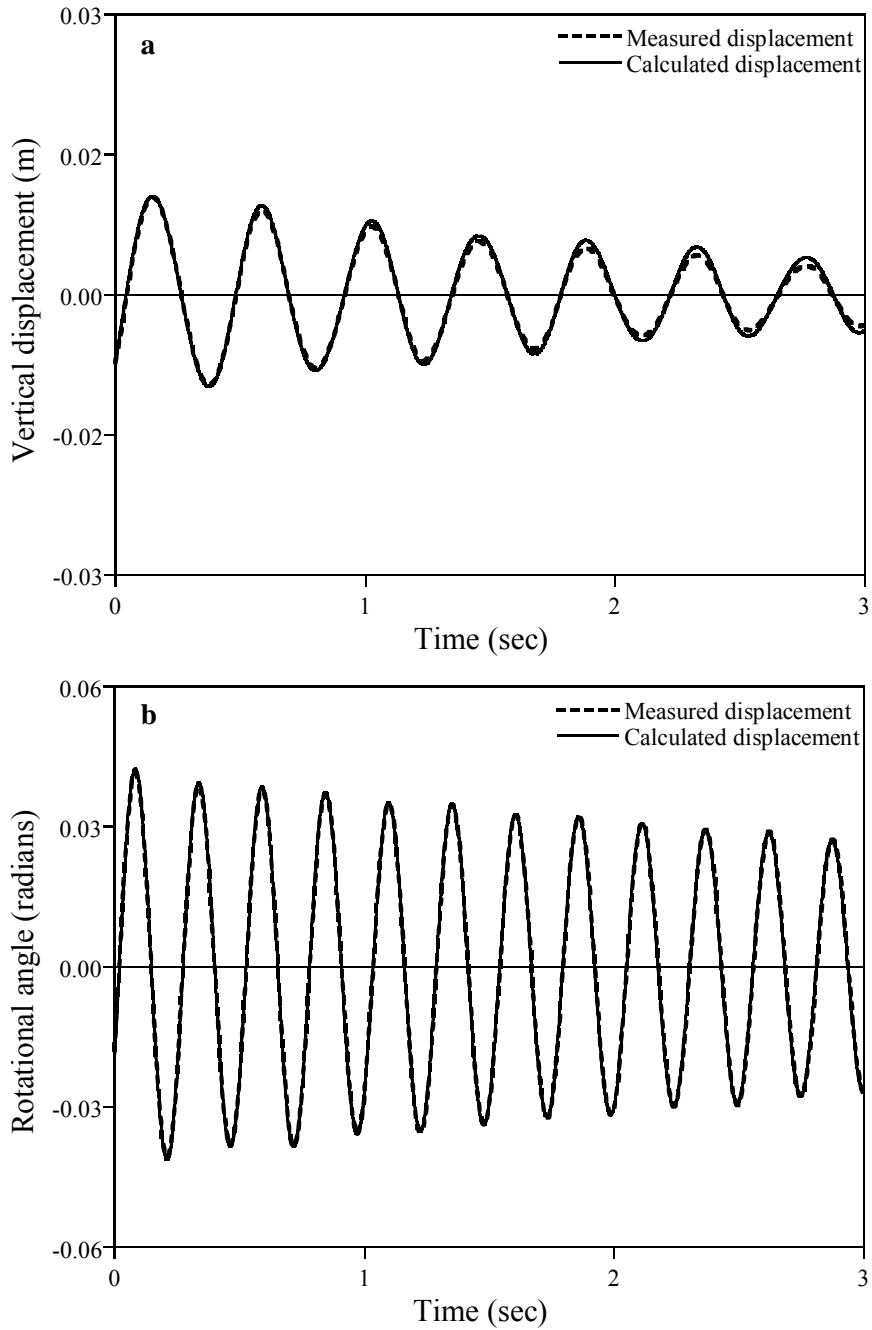
Figure 4-13. Calculated displacements with extracted flutter derivatives for the thin rectangular section at the wind velocity of 5.86m/s: (a) vertical displacement and (b) rotational angle

143

4.4.2 Free-vibration test of an H-type section – case of a bluff section

A bluff H-type section of B/D=9.6 shown in Fig. 4-5(b) is tested in this example. The dimensions of the section and the locations of sensors are illustrated in Fig. 4-14. These types of sections are widely used in medium-span cable-stayed bridges. The wind tunnel tests were performed at the Boundary Layer Wind Tunnel Laboratory at the University of Western Ontario in Ontario, Canada (Kim and King, 2007). This example is adopted from the work by Hong et al. (2010), in which the details on the experimental setups and reconstruction parameters are presented. Sudden release tests were carried out for 16 different wind velocities, and 20 measurements were taken for each wind velocity.

Mass per unit length: 3.64 (kg/m)
Mass moment of inertia per unit length: 0.102 (kg-m^2/m)
Air density: 1.25 (kg/ m^3)
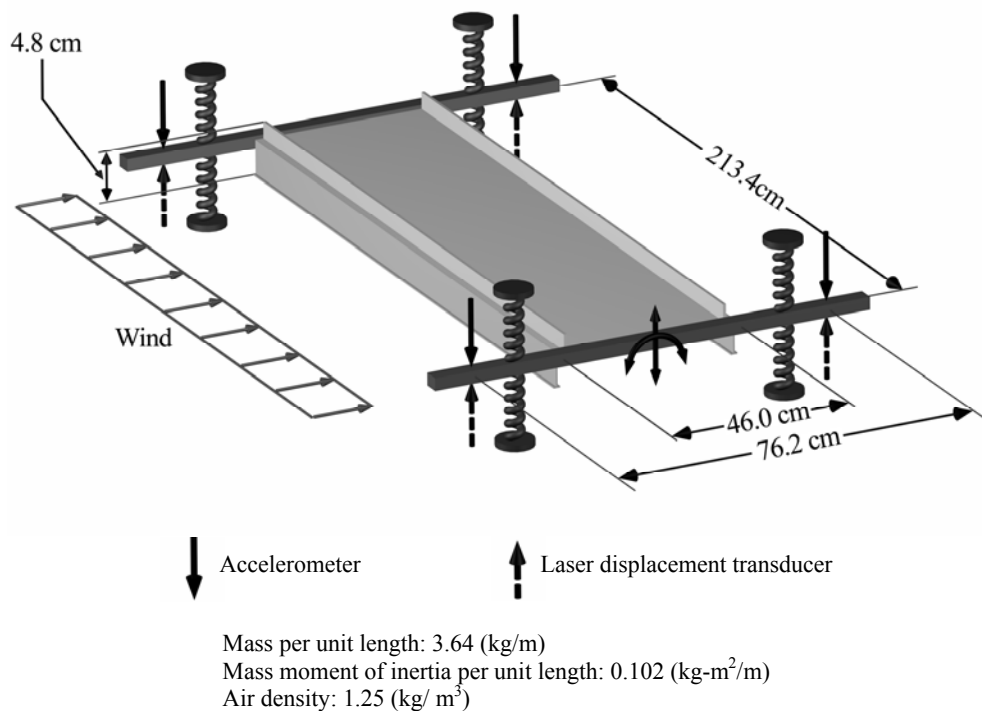
Figure 4-14. Experimental setup for the bluff H-type section

The correction factors used for the reconstruction are shown in Fig. 4-15. The displacements for all wind velocity are successfully reconstructed, and the same levels of accuracy as shown in Fig. 4-9 are obtained but are not presented here. The frequencies and damping ratios for the windless condition are identified as f_1=3.05Hz, f_2=5.13Hz, ξ_1=0.671% and ξ_2=0.316% with the reconstructed displacement and velocity.

Figs. 4-16 and 4-17 show the identified H_i^* components and A_i^* components, respectively. The flutter derivatives of the bluff section exhibit much more complicated variations with wind velocities than the thin rectangular section. This is because flow fields around bluff sections are severely perturbed, and thus strong turbulence is developed.
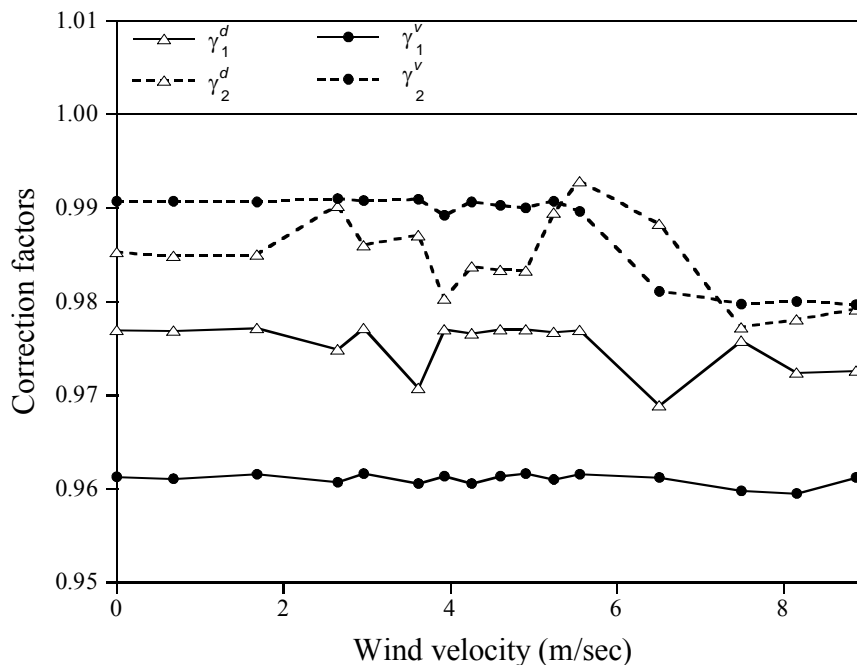
Figure 4-15. Correction factors applied for the bluff H-type section

The cubic spline fits of the identified results by the proposed method are also drawn in the figures. Most of the flutter derivatives by the proposed method show good agreements with those by the MITD method. Although some differences are observed for H_1^* for higher wind velocities as in the thin rectangular section, the overall consistency between the proposed method and the MITD method is confirmed for the bluff section.

Figs. 4-16 and 4-17 show the identified H_i^* components and A_i^* components, respectively.
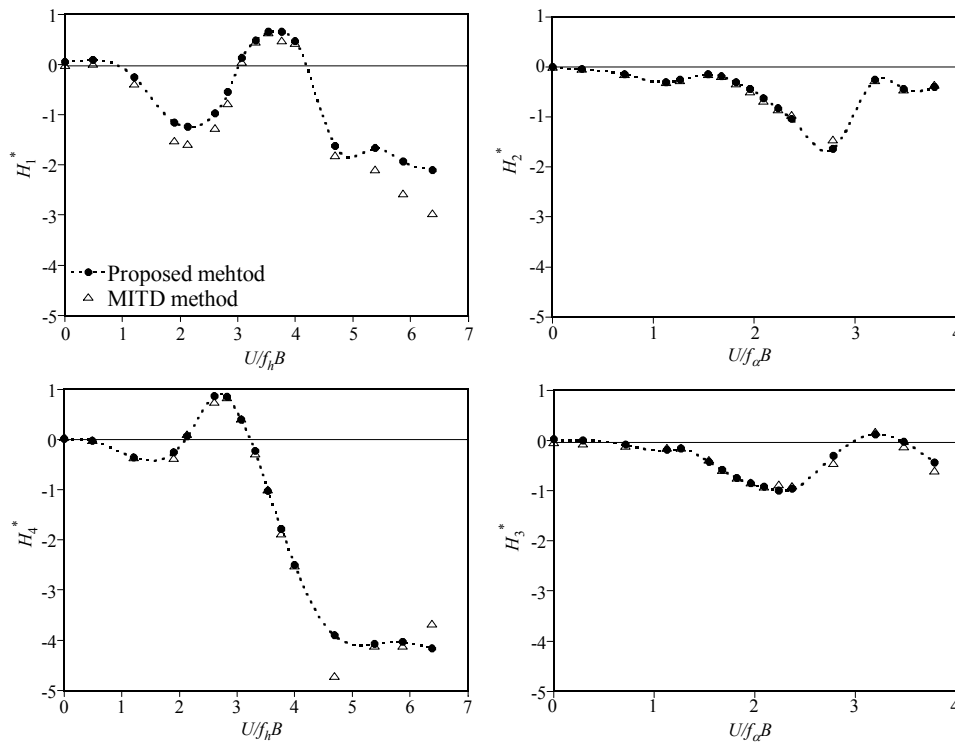
Figure 4-16. Identified flutter derivatives for the bluff H-type section - H^* components: (a) H_1^*, (b) H_2^*, (c) H_4^* and (d) H_3^*

146
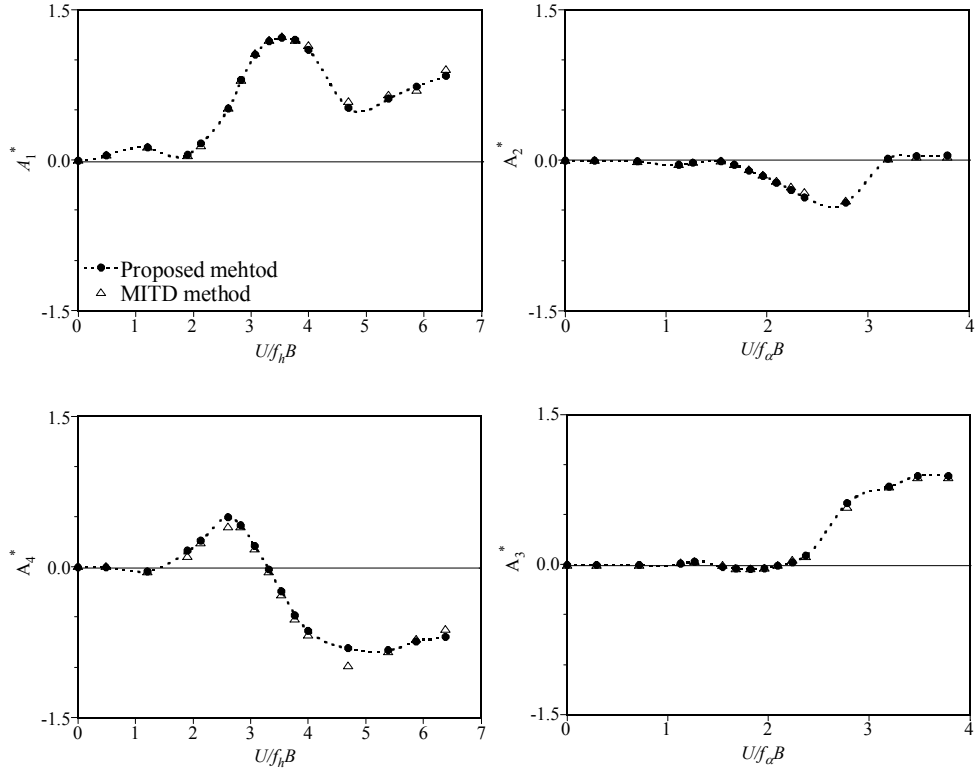
Figure 4-17. Identified flutter derivatives for the bluff H-type section - A^* components: (a) A_1^*, (b) A_2^*, (c) A_4^* and (d) A_3^*

The flutter derivatives of the bluff section exhibit much more complicated variations with wind velocities than the thin rectangular section. This is because flow fields around bluff sections are severely perturbed, and thus strong turbulence is developed. The cubic spline fits of the identified results by the proposed method are also drawn in the figures. Most of the flutter derivatives by the proposed method show good agreements with those by the MITD method. Although some differences are observed for H_1^* for higher wind velocities as in the thin rectangular section, the overall consistency between the proposed method and the MITD

147

method is confirmed for the bluff section.

Figs. 4-18 and 4-19 show the modal frequencies and the damping ratios calculated with identified flutter derivatives, respectively. The calculated modal frequencies agree well with those identified by the FFT of the measured accelerations. The damping ratios for the 1st and 2nd mode are identified as being slightly lower and higher, respectively, by the proposed method than by the MITD method. Near zero damping ratios are predicted for the 1st and 2nd mode at wind velocities of around 5 m/sec and 3.6 m/sec, respectively.   Fig. 4-20 compares the calculated displacements by Eq. (4-1) to the measured displacements at a wind velocity of 4.27m/s.   The same numerical integration scheme used in example 1 is employed. Both the phase and amplitude of the rotational angle are predicted accurately with the identified results, while the amplitude of the vertical displacement is calculated somewhat larger than the measurement as in the previous example.
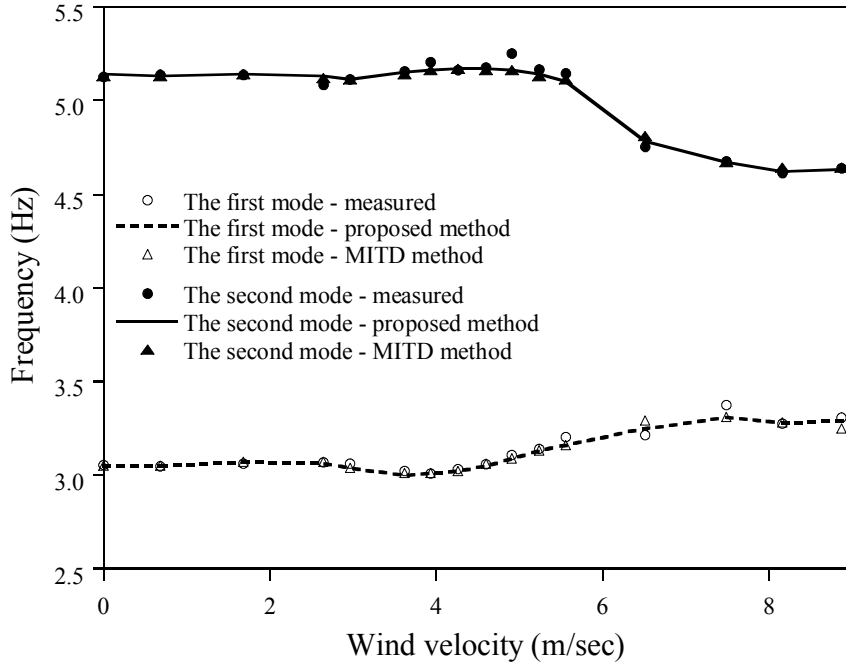
Figure 4-18. Two dominant frequencies of the bluff H-type section
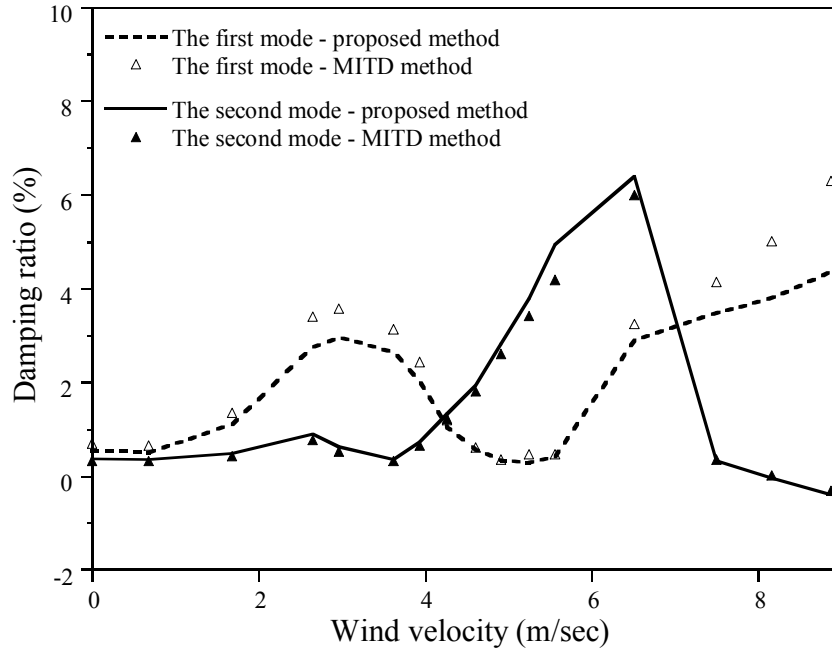
Figure 4-19. Identified damping ratios for the bluff H-type section

149
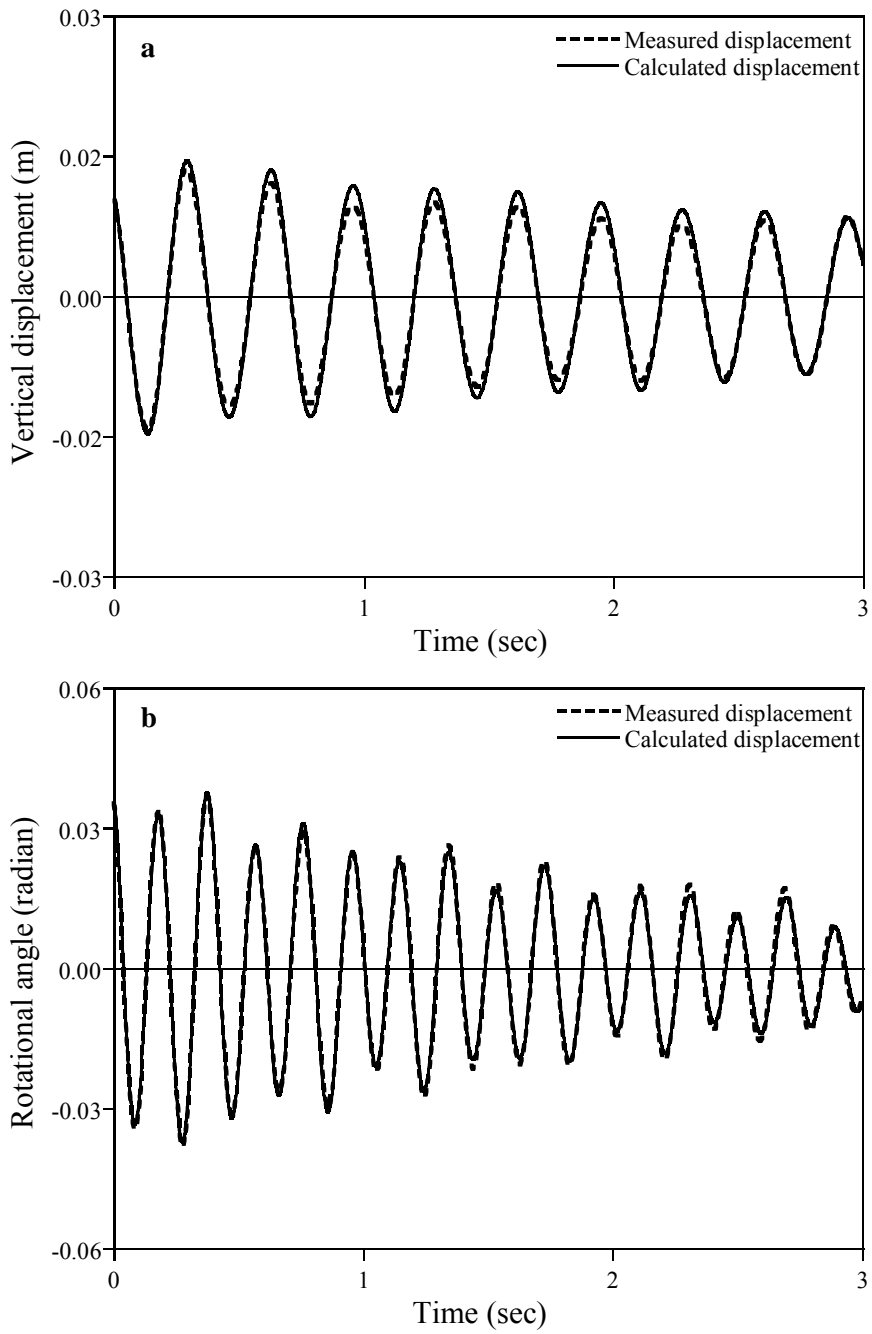
Figure 4-20. Calculated displacements with extracted flutter derivatives for the bluff H-type section at the wind velocity of 4.27m/s: (a) vertical displacement and (b) rotational angle

150

4.4.3 Numerical simulation of forced-vibration test controlled by a prescribed force

The proposed EEE method is applied to an extraction of the flutter derivatives for the numerically simulated force-control test of the thin rectangular section in the section 4.4.1. To simulate the analytic motion response, the optimized flutter derivatives of the section presented by Jung et al. (2011), which is modified to satisfy causality condition through proper optimization, are adopted for the exact flutter derivatives of the numerical analysis.

Two forced vibration tests of the section model are conducted by applying following excitation forces for 10 seconds, respectively.

$$\mathbf{F}_{ex,1}(t) = \begin{pmatrix} 1 \\ 0 \end{pmatrix} \sin \omega_{ex}t, \quad \mathbf{F}_{ex,2}(t) = \begin{pmatrix} 0 \\ 1 \end{pmatrix} \sin \omega_{ex}t \qquad (4\text{-}51)$$

The analytic solution for the force-control test in Eq. (4-31) and (4-32) is derived from the Scanlan's equation, the linearity and vibrational mode shape independency are satisfied. Hence any sets of two excitation forces with different ratios of amplitudes in the vertical and rotational direction can be properly employed for the force-control test. The analytic acceleration is obtained from the second order differentiation of Eq. (4-31).

$$\begin{aligned}
\ddot{\mathbf{U}}_1(t) &= -\omega_{ex}^2 \left[\begin{pmatrix} h_{s,1} \\ \alpha_{s,1} \end{pmatrix} \sin(\omega_{ex}t) + \begin{pmatrix} h_{c,1} \\ \alpha_{c,1} \end{pmatrix} \cos(\omega_{ex}t) \right] \\
\ddot{\mathbf{U}}_2(t) &= -\omega_{ex}^2 \left[\begin{pmatrix} h_{s,2} \\ \alpha_{s,2} \end{pmatrix} \sin(\omega_{ex}t) + \begin{pmatrix} h_{c,2} \\ \alpha_{c,2} \end{pmatrix} \cos(\omega_{ex}t) \right]
\end{aligned} \qquad (4\text{-}52)$$

The acceleration is calculated for the several reduced frequencies from 2 to 20 with constant increment and measured at the sampling of 100 Hz. Though the analytic displacement and velocity can be possibly calculated, to simulate the actual situation, the displacement and velocity are reconstructed by the FFIR filter in the section 3. To alleviate the rippling error of the FFIR filter the reconstructed responses are modified with the same procedure in Eq. (4-33) which is used for the modification of the response in the free-vibration test. Since the analytic acceleration of the forced-vibration test is solely single frequency components without noise, near exact displacement and velocity are reconstructed by this modification procedure.
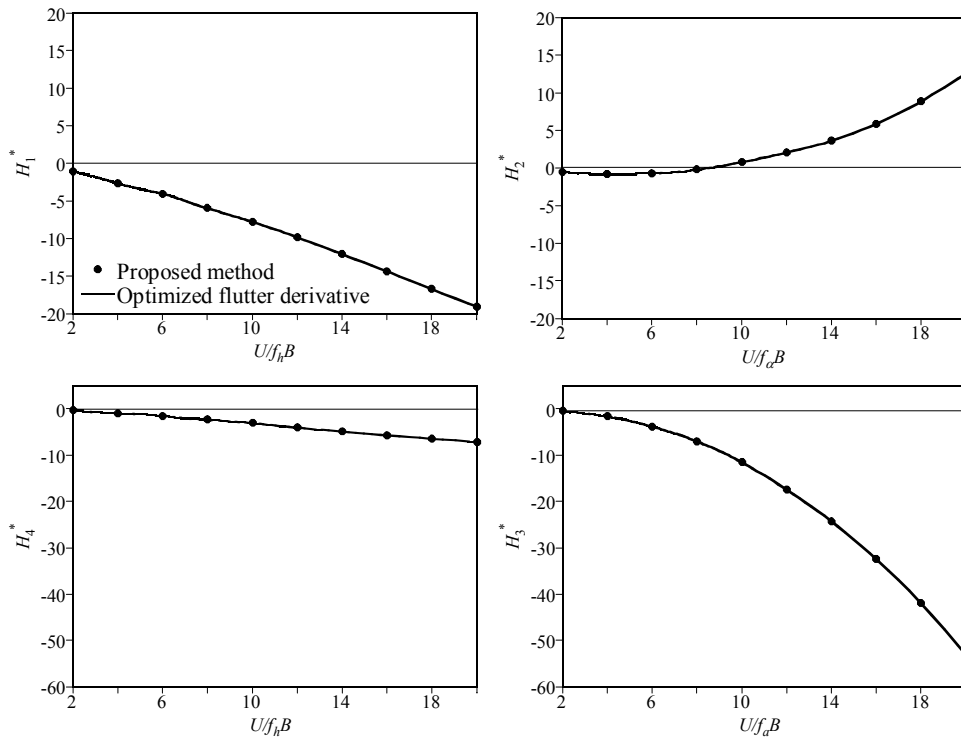
Figure 4-21. Identified flutter derivatives for the numerically simulated force control test - H^* components: (a) H_1^*, (b) H_2^*, (c) H_4^* and (d) H_3^*
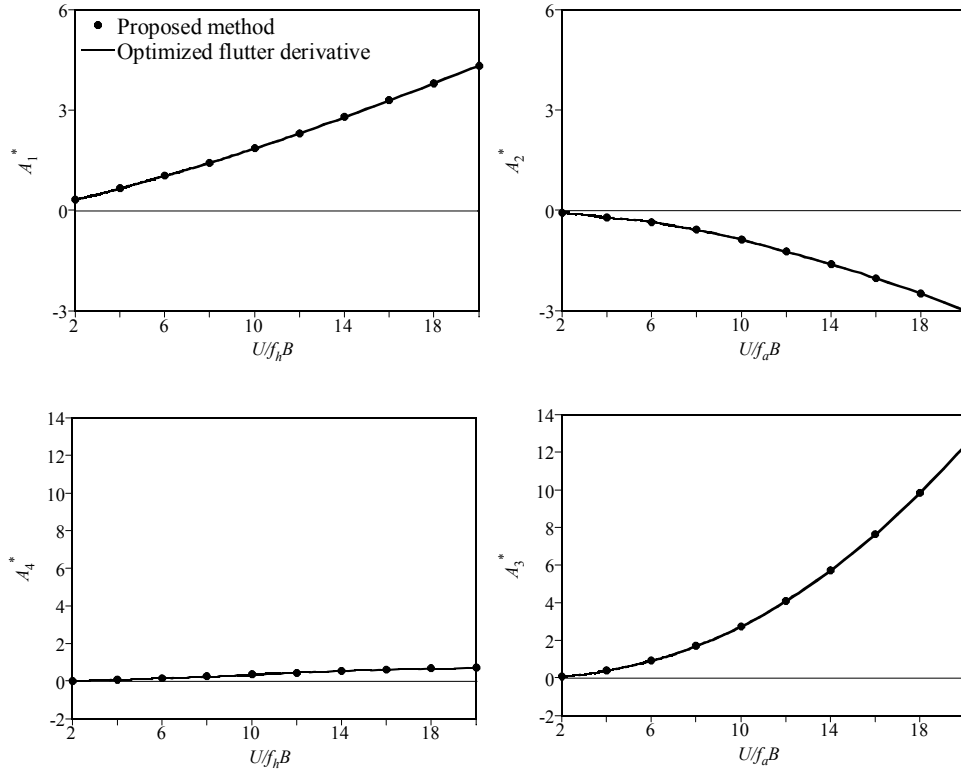
Figure 4-22. Identified flutter derivatives for the numerically simulated force control test - A^* components: (a) A_1^*, (b) A_2^*, (c) A_4^* and (d) A_3^*

Figs. 4-21 and 4-22 show the identified H_i^* components and A_i^* components with the exact value of flutter derivatives, respectively. The identified flutter derivatives perfectly agree with the exact values in this numerical study.

5. Conclusion and further study

Conclusions

This study proposes three types of FIR filters, the CFIR FDM-FIR filter and FFIR filter, to reconstruct displacement from measured accelerations. The BEF transfer function is derived by taking the variation of the minimization problem that defines an inverse problem for the reconstruction of displacement. The regularization factor in the inverse problem is determined with the desired accuracy at the target frequency. The CFIR filter directly approximates the BEF transfer function in the frequency domain by the truncated Fourier series, while FDM-FIR filter and the FFIR filter are obtained by discretizing the minimization problem itself with FDM and the variational statement of the minimization problem with the standard FEM, respectively. The second order central difference method is utilized to discretize the second order differentiator and the Hermitian shape function is utilized to interpolate displacement in each finite element. By the virtue of the FFIR filter, velocity as well as displacement can be reconstructed simultaneously from the same measurement.

The proposed filters are capable of suppressing the low frequency noises below the target frequency, and reconstructing displacement accurately above the target frequency. The longer filter size results in smaller rippling amplitude in three filters. The CFIR filter exhibits a uniform frequency response from the target frequency to the Nyquist Frequency in case the filter size is set to either the standard

or long filter size. The filter sizes other than the two filter sizes cause diverging rippling amplitudes in the transfer function of the CFIR filter, which may be considered to be the one shortcoming of the CFIR filter. On the other hand, the size of the FDM-FIR filter and FFIR filter size can be adjusted freely as needed in applications and the rippling amplitude of them damps out quickly for all filter sizes. Although the accuracy of the FDM-FIR filter and FFIR filter deteriorates in higher frequency ranges, the overall performance is not affected seriously because the high frequency contents in measured accelerations contribute little to the reconstructed displacement. From the aforementioned facts, it may be concluded that the CFIR filter is a good choice for the reconstruction in systems with a wide frequency spectrum while the FDM-FIR filter and FFIR filter are suitable for low-frequency dominant systems. To reconstruct velocity as well as displacement, however, the FFIR filter should be employed.

Four examples are presented to verify the proposed FIR filters. In the numerical simulation study and field experiment, the proposed FIR filters yield very accurate displacement, and exhibit robust behaviors against measurement noises.

In the last example, the flutter derivatives for the section model of a bridge deck system with plate girders are identified by the reconstructed displacement, and are compared with those by measured displacement. Both the identified derivatives show good agreement with each other. Therefore, the proposed FFIR filters can be applied to the identification of the flutter derivatives of long-span cable-supported bridges in service, in which the measurements of displacement are

considered to be one of the major obstacles.   It is believed that the proposed FFIR filters provide accurate and reliable alternatives to direct measurement of dynamic displacements, which is costly, difficult and almost impossible, especially for large-manifest scale structures.

Further study

Scope of the proposed reconstruction scheme

In the near-field of an earthquake the effects of the rotational components of ground motion may not be negligible compared to the effects of translational motions.   Several analyses of the equations of motion of horizontal and vertical pendulum show that horizontal sensors are sensitive not only to translational motion but also to tilts.   In this reasons, different groups of researchers in earthquake field have tried to measure the displacement responses in the longitudinal, transverse and vertical directions with consideration of the tilts components [Graizer 2005 and Graizer 2006].

The scope of the reconstruction scheme in this study, however, is to reconstruct the tangential displacement and velocity which correspond to the measured tangential acceleration rather than the horizontal and vertical responses.   Under the small deformation assumption in serviceability state, these tangential responses can be regarded as the vertical or horizontal responses.

Since the accelerometers commonly have an accurate high-frequency resolution but it is insensitive to near-zero frequency responses like pseudo-static compo-

nents. This study has mainly investigated the displacement and velocity reconstruction for the pure dynamic responses which are defined with harmonic functions through the Duhamel integral.

Expansion of the scope of the proposed reconstruction scheme

In civil structure accelerometers are most often used, however displacement sensors, such as non-contact optical techniques as well as GPS-based methods are becoming more common. The accelerometers commonly have an accurate high-frequency resolution but it is insensitive to near-zero frequency responses like pseudo-static components. On the other hand, displacement-based sensors can measure the pseudo-static components and the permanent displacement while the high-frequency resolution limited, and often relatively low sampling rates are used. It is suggested, if possible, to exploit the redundancy in the sensors and combine the acceleration and displacement measurements in a manner which yields highly accurate motion data. Though this study mainly investigates the displacement reconstruction for the pure dynamic responses by setting the static equilibrium position to be zero, the proposed method has possibilities to be expended for the responses from different types of sensor by imposing non-zero static equilibrium position to the regularity condition. Continuous researches on these fields should be intensively performed to apply the displacement reconstruction to more general monitoring of the civil structures.

Investigation of the similitude law for the flutter derivatives identified from the free-vibration test and implementation of the force-control test in the wind tunnel for the estimation of flutter derivatives

There is apparent uncertainty in frequency dependency for the flutter derivatives identified from the 2-DOF free-vibration test and the frequency similarity in Eq. (4-49) is hardly applied for the flutter derivatives of the bluff body section. As far as the frequency dependency of the flutter derivatives is concerned, the displacement-control test can be best solution. However, the displacement-control test is not free from the limitation that the mutual influence of structural dynamics and fluid flow in regions of moving boundaries are not fully considered. In this reason, the force-control test should be implemented and further research on the relationship and relative differences among three tests should be intensively verified from the result of experiments.

One of the alternative methods to extract the flutter derivatives rather than the wind tunnel test is the computerized fluid dynamic (CFD) analysis. After the implementation of the force-control test, continuous researches about the relation between the wind tunnel tests and the CFD method and limitation of each experimental method should be performed.

Reference

Bardella (2003)

    Bardella L., Carini A. and Genna F., "Time integration errors and some new functionals for the dynamics of a free mass", *Computers & Structures*, vol. 81, pp. 2361-2372 (2003).

Bartoli (2009)

    Bartoli G., Contri S., Mannini C. and Righi M., "Toward an improvement in the identification of bridge deck flutter derivatives", *Journal of Engineering Mechanics*, vol. 135 (8), pp. 771–785 (2009)

Boore (1997)

    Boore D.M., Stephens C.D. and Joyner W.B., "Comments on baseline correction of digital strong-motion data: Example from the 1999 Hector Mine, California, Earthquake", *Bulletin of the Seismological Society of America*, vol. 87, pp. 932-944 (1997).

Chen (2004)

    Chen X. and Kareem A., "Efficacy of the implied approximation in the identification of flutter derivatives", *Journal of Structural Engineering*, vol. 130(12), pp. 2070–2074 (2004).

Cheng (2005)

    Cheng A. and Cheng D.T., "Heritage and early history of the boundary value element method", *Engineering Analysis with Boundary Element,* vol. 29, pp. 268-302 (2005).

Chiu (1997)

    Chiu H.C., "Stable baseline correction of digital strong-motion data", *Bulletin of the Seismological Society of America*, vol. 87, pp. 932-944 (1997).

Chowdhury (2003)

    Chowdhury A. G. and Sarkar P. P., "A new technique for identification of eighteen flut-

ter derivatives using a three-degree-of freedom section model", *Engineering Structures*, vol. 25 (14), pp. 1763–1772 (2003).

Chopra (2000)

Chopra A.K., Dynamics of Structures, Theory and Applications to Earthquake Engineering, 2nd ed., Prentice Hall, Englewood Cliffs, NJ, (2000).

Diana (2004)

Diana G., Resta F., Zasso A., Belloli M. and Rocchi D., "Forced motion and free motion aeroelastic tests on a new concept dynamometric section model of the Messina suspension bridge", *Journal of Wind Engineering and Industrial Aerodynamics*, vol. 92, pp. 441–462 (2004).

Falco (1992)

Falco M., Curami A. and Zasso A., "Nonlinear effects in sectional model aeroelastic parameters identification", *Journal of Wind Engineering and Industrial Aerodynamics*, vol. 41-44, pp. 1321–1332 (1992).

Gavin (1998)

Gavin H.P., Morales R. and Reilly K., "Drift-free integrators", *Review of Scientific Instruments*, vol. 69 (5), pp. 2171-2175 (1998).

Golub (1996)

Golub G.H.and Van Loan C.F., *Matrix Computations*, 3rd ed., Johns Hopkins, Baltimore, (1996).

Graizer (2005)

Graizer V. M., "Effect of tilt on strong motion data processing", *Soil Dynamics and Earthquake Engineering*, vol. 25, pp. 197–204 (2005).

Graizer (2006)

Graizer V. M., "Tilts in strong ground motion", *Bulletin of the Seismological Society of*

America, vol. 96(6), pp. 2090–2102 (2006).

Gu (2000)

Gu M., Zhang R. and Xiang H., "Identification of flutter derivatives of bridge decks", *Journal of Wind Engineering and Industrial Aerodynamics*, vol. 84, pp. 151–162 (2000).

Gupta (2001)

Gupta V.K., Nielsen S.R.K., and Kirkegaard P.H., "A preliminary prediction of seismic damage-based degradation in RC structures", *Earthquake Engineering and Structural Dynamics*, vol. 30, pp. 981-993 (2001).

Hansen (1988)

Hansen P.C., Rank-Deficient and Discrete Ill-Posed Problems: Numerical Aspects of Linear Inversion, SIAM, Philadelphia, (1988).

Hamming (1989)

Hamming R.W., *Digital Filters,* 3rd ed., Prentice-Hall, Englewood Cliffs, NJ, (1989).

Hetenyi (1946)

Hetenyi M.I., Beams on elastic foundation: theory with applications in the fields of civil and mechanical engineering, Univ. of Michigan, (1946).

Hjelmstad (1995)

Hjelmstad K.D., Banan M.R. and Banan M.R., "Time-domain parameter estimation algorithm for structures. I: computational aspects", *Journal of Engineering Mechanics*, vol. 121 (3), pp. 424–434 (1995).

Hong (2010)

Hong Y.H., Kim H.K. and Lee H.S., "Reconstruction of dynamic displacement and velocity from measured accelerations using the variational statement of an inverse prob-

lem", *Journal of Sound and Vibration*, vol. 329, pp. 4980–5003 (2010).

Housner (1997)

Housner G.W., Bergman L.A., Caughey T.K., Chassiakos A.G., Claus R.O., Masri S.F., Skelton R.E., Soong T.T., Spencer B.F. and Yao J.T.P., "Structural control: past, present, and future", *Journal of engineering mechanics*, vol. 123, pp. 897-971 (1997).

Hughes (1987)

Hughes T.J.R., The Finite Element Method: Linear Static and Dynamic Finite Element Analysis, Prentice-Hall, Englewood Cliffs, NJ, (1987).

Ibrahim (1977)

Ibrahim S. R. and Mikulcik E. C., "A method for the direct identification of vibration parameters from the free response", *Shock and Vibration Bulletin*, vol. 47(4), pp.183–198 (1977).

Iwamoto (1995)

Iwamoto M. and Fujino Y., "Identification of flutter derivatives of bridge deck from vibration data", *Journal of Wind Engineering and Industrial Aerodynamics*, vol. 54/55, pp. 55–63 (1995).

Iwan (1985)

Iwan W.D., Moser M.A. and Peng C.Y., "Some observations on strong-motion earthquake measurement using a digital accelerograph", *Bulletin of the Seismological Society of America*, vol. 75 (5), pp. 1225-1246 (1985).

Jung (2011)

Jung K., Kim H. K. and Lee H. S., "Evaluation of impulse response functions for convolution integrals of aerodynamic forces by optimization with a penalty function", *Journal of Engineering Mechanics*, *ASCE,* under review, (2011).

Kang (2005)

Kang J.S., Park S.K., Shin S.B. and Lee H.S., "Structural system identification in time domain using measured acceleration", *Journal of Sound and Vibration*, vol. 228, pp. 215-234 (2005).

Kim (2007)

Kim J.D. and King J.P.C., *The Development of Wind Tunnel Test Technique for an Aeroelastic Buffeting Analysis of Long-span Bridges*, BLWTL-SS19-2007-DRAFT Report submitted to Korea Wind Engineering Research Center, The Boundary Layer Wind Tunnel Laboratory of The University of Western Ontario, (2007).

Kumar (1996)

Kumar B., Choudhury D.R. and Kumar A., "On the Design of Linear Phase, FIR Integrators for Midband Frequencies", *IEEE Transactions on Signal* Processing, vol. 44 (10), pp. 2391-2395 (1996)

Lapidus (1982)

Lapidus L. and Pinder G. F., Numerical Solution of Partial Differential Equations in Science and Engineering, John Wiley & Sons, New York, (1982).

Lee (1999)

Lee H.S., Kim Y.H., Park C.J. and Park H.W., "A new spatial regularization scheme for the identification of the geometric shape of an inclusion in a finite body", *International Journal for Numerical Methods in Engineering*, vol. 46 (7), pp. 973-992 (1999).

Lee (2010)

Lee H.S., Y.H. Hong and H.W. Park, "Design of an FIR Filter for the Displacement Reconstruction Using Measured Acceleration in Low-frequency Dominant Structures", *International Journal for Numerical Methods in Engineering*, vol. 82, pp. 403-434 (2010)

Li (2003)

Li Y., Liao H. and Qiang S., "Weighting ensemble least-square method for flutter de-

rivatives of bridge decks", *Journal of Wind Engineering and Industrial Aerodynamics* vol. 91, pp. 713–721 (2003).

Ljung (1999)

Ljung L., *System Identification: Theory for the User*, 2nd ed., Prentice-Hall, Upper Saddle River, NJ, (1999).

Matsumoto (1993)

Matsumoto M., Shiraishi N., Shigetaka K. and Niihara Y., "Aerodynamic derivatives of coupled/hybrid flutter of fundamental structural sections", *Journal of Wind Engineering and Industrial Aerodynamics*, vol. 49, pp. 575–584 (1993).

Montgomery (2005)

Montgomery D.C., "*Introduction to Statistical Quality Control*, 5th ed.", John Wiley & Sons, Hoboken, NJ, (2005).

Morgenthal (2000)

Morgenthal G., *Fulid-Structure Interaction in Bluff-Body Aerodynamics and Long-Span Bridge Design: Phenomena and methods*, Technical report No. CUED/D-Struct/TR. 187, University of Cambridge department of engineering, (2000).

Oppenheim (1999)

Oppenheim A.V., Schafer R.W. and Buck J.R., *Discrete-Time Signal Processing*, 2nd *ed*., Prentice-Hall, Upper Saddle River, NJ, (1999).

Park (1984)

Park Y.J., Ang A.H-S., and Wen Y.K, , *Seismic damage analysis and damage-limiting design of R/C buildings*, Civil Engineering Studies, Technical Report No. SRS 516, University of Illinois, Urbana Champaign (1984)

Park (2001)

Park H.W., Shin S.B. and Lee H.S., "Determination of an optimal regularization factor

in system identification with Tikhonov function for linear elastic continua", *International Journal for Numerical Methods in Engineering*, vol. 51 (10), pp. 1211-1230 (2001).

Park (2007)

Park H.W., Park M.W., Ahn B.K., and Lee H.S., "1-norm based regularization scheme for system identification of structures with discontinuous system parameters", *International Journal for Numerical Methods in Engineering*, vol. 69 (3), pp. 504-523 (2007).

Park (2008)

Park S.K., Park H.W., Shin S.B. and Lee H.S., "Detection of abrupt structural damage induced by an earthquake using time-window technique", *Computers & Structures,* vol. 86, pp. 1253-1265 (2008)

Rabiner (1975)

Rabiner L.R. and Gold B., *Theory and Application of Digital Signal Processing*, Prentice-Hall, Englewood Cliffs, NJ, (1975).

Sarkar (1992)

Sarkar P. P., Jones N. P. and Scanlan R. H., "System identification for estimation of flutter derivatives", *Journal of Wind Engineering and Industrial Aerodynamics*, vol. 41/44, pp. 1243–1254 (1992).

Sarkar (1994)

Sarkar P. P., Jones N. P. and Scanlan R. H., "Identification of aeroelastic parameters of flexible bridges", *Journal of Engineering Mechanics*, *ASCE,* vol. 120(8), pp. 1718–1741 (1994).

Scanlan (1971)

Scanlan R. H. and Tomko J. J., "Airfoil and bridge deck flutter derivatives", *Journal of Engineering Mechanics Division*, *ASCE,* vol. 97 (6), pp. 1717–1733 (1971).

Simiu (1996)

Simiu E. and Scanlan R. H., Wind Effects on Structures: fundamentals and applications to design, 3rd ed., John Wiley and Sons, (1996).

Smyth (2007)

Smyth A. and Wu M., "Multi-rate Kalman filtering for the data fusion of displacement and acceleration response measurements in dynamic system monitoring", *Mechanical Systems and Signal Processing*, vol. 21, pp. 706-723 (2007).

Sohn (2004)

Sohn H., Farrar C.R., Hemez F.M., Shunk D.D., Stinemates S.W., Nadler B.R. and Czarnecki J.J., *A review of structural health monitoring literature: 1996-2001*, Los Alamos National Laboratory report LA-13976-MS (2004).

Stephens (1985)

Stephens J.E. and Yao J.T.P., "Data processing of earthquake acceleration records", Report no. CE-STR-85-5, Purdue University, West Lafayette, Indiana, (1985).

국문초록

변위, 속도, 가속도와 같은 구조물의 동적응답특성은 구조물의 건전성감시(Structural Health Monitoring)와 제어(Control)에 있어서 필수적인 계측치들이다. 이러한 동적응답 중 변위이력은 비선형 거동을 하는 구조물의 건전성감시와 제어에 있어서 중요한 정보를 담고 있기 때문에 이러한 변위 이력을 확보하는 것은 매우 중요하다. 하지만 일반적으로 교량이나 고층빌딩과 같은 대형구조물에서 이러한 변위 이력을 측정하기 위한 변위계의 고정된 지점을 확보하는 것이 불가능하며 이러한 이유로 인하여 대형 토목구조물에서 변위를 직접적으로 측정하는 것은 한계가 있다. 이에 반해, 가속도는 관성을 기반으로 하여 측정되기 때문에 고정된 지점을 확보할 필요가 없으며 넓은 주파수 범위에서 다양한 종류의 가속도계가 상업적으로 판매되기 때문에 대형구조물로부터 측정이 용이하다. 이러한 측정의 용이성과 높은 해상도로 인해 가속도가 여러 공학적 문제에서 가장 손쉽게 측정되는 동적응답이라고 할 수 있다.

수학적으로 가속도는 변위의 2계 미분에 해당하고, 따라서 이러한 정의를 바탕으로 측정 가속도로부터 변위를 계산하기 위해서 많은 노력이 시도되었다. 이중 뉴마크방법으로 대표되는 시간누적속성(time-marching)에 기반을 둔 적분 알고리즘은 측정가속도로부터 변위를 계산하기 위한 가장 손쉽고도 명확한 방법이라고 할 수 있다. 하지만 이러한 시간 누적성에 기반을 둔 적분알고리즘들은 여러 가지 원인에서 기인한 문제점들을 갖고 있다. 먼저 이러한 시간누적성에 기초한 적분을 수행하기 위해서 필요한 초기값인 변위와 속도의 초기값은 일반적인 문제에서 측정이 불가능하거나 혹은 부정확하다는 문제점이 있다. 이러한 초기치 오차로 인한 문제뿐만 아니라, 가속도 측정과정에서는 일반적으로 여러 가지 요인에 의해서 무작위(random) 측정오차가 가속도 측정치에 포함되고 이러한

169

측정오차는 물리적으로 의미 없는 결과를 만들게 된다. 특히 이러한 측정 잡음 중 저주파 성분은 2차 적분과정에서 증폭되어 계산된 변위를 심각하게 왜곡시킨다. 또한 이러한 저주파 성분의 변위 오차 증폭은 특히 대형토목구조물과 같이 저주파 변위가 지배적인 구조물에서 복원된 변위의 신뢰도를 매우 저하시킨다.

이러한 이유로 이 논문은 측정 가속도로부터 변위 및 속도를 정확하게 재구성하는 기법을 제안한다. 이러한 시간영역에서의 재구성기법에서는 측정가속도로부터 변위 및 속도를 계산하는 문제를 기존의 시간누적속성에 기초한 초기치문제(initial value problem)로서 보는 것이 아니라 유한한 크기의 측정된 가속도에 대해서 경계조건문제(boundary value problem)로 정의하여 변위 및 속도를 재구성하게 된다. 시간창(time window)이라고 하는 유한한 크기의 시간에 대해서 가속도이력이 이미 측정되어 주어져 있다면, 변위의 2계 미분은 가속도이기 때문에 변위는 하나의 시간 창 내부에서 측정된 가속도와 재구성될 변위의 2계 시간 미분사이의 차를 최소화하는 최적화 문제를 풀어 구할 수 있다. 그리고 이 2계 시간미분은 중앙차분(central finite difference) 또는 유한요소법(finite element method)를 이용하여 근사할 수 있다. 이러한 이산화를 통해 변위재구성을 최종적으로 FIR-filter(finite impulse response filter) 형태로 제안하고 필터 관점에서의 건전성을 평가한다.

Scanlan 에 의해 공탄성(aeroelastic) 방정식에 근거한 플러터계수가 제안된 이래로 풍동실험을 통한 교량단면의 플러터계수 추정에 대해서 많은 연구들이 수행되었다. 일반적으로 풍동실험에서 변위이력만을 측정하고 또한 직접적인 속도의 측정은 매우 난해하기 때문에, 풍동실험은 공간(space)상에서는 모든 자유도가 측정 가능하지만 상태(state)상에는 완전측정(full measurement)이 불가능하다. 따라서 계수추정문제는 부분측정(partial measure-ment)으로 인해 동방정식에서 바로 구할 수 없다.

이러한 문제를 해결하기 위해서 많은 기법들이 수학적 모델로부터 구해진 시스템변위응답과 측정변위 사이의 상대오차를 최소화하는 OEE(output error estimation)에 기반하여 제안되었다. 하지만 완전측정이 가능한 경우, 이러한 OEE기반의 최소화 문제를 풀지 않고

직접 동방정식상에서 힘의 오차를 최소하는 문제를 통해 플러터계수를 추정할 수 있다. 따라서 이 논문에서는 재구성기법을 통한 완전측정치를 이용하여 직접적으로 동방정식의 오차를 최소화하여 플러터계수를 추정하는 EEE(equation error estimation) 방법을 제안한다. 또한 측정 가속도도부터 변위와 속도이력을 계산하여 완전측정이 가능하게 하는 FFIR필터를 플러터계수 추정에 이용하는 과정을 제안한다.